ULTRACOLD FERMIONS IN A HONEYCOMB OPTICAL LATTICE

LEE KEAN LOON

B.Sc. (Hons.), NUS

A THESIS SUBMITTED FOR

THE DEGREE OF DOCTOR OF PHILOSOPHY

NUS Graduate School for Integrative Sciences and Engineering

National University of Singapore

2010

Acknowledgments

This work would not exist without the help and support from many people. I sincerely thank my supervisors, Berthold-G. Englert, Benoît Grémaud and Christian Miniatura, for their guidance and the various opportunities that they have given me. Equally important are the assistance from my collaborators, who are Han Rui, Karim Bouadim, Frédéric Hébert, George G. Batrouni and Richard T. Scalettar. Special thanks to Scalettar for providing me the numerical codes, Karim for his help in adapting the codes, Dominique Delande for the discussion on the relationship between distortions and mean energy as well as David Wilkowski for his explanations on the experimental details. I would like to acknowledge here the financial support from both NUS Graduate School for Integrative Sciences and Engineering (NGS) and French Merlion PhD program (CNOUS 20074539). I am grateful to the administrative staff involved, who are Cheng Bee, Rahayu, Irene and Vivien from NGS as well as Audrey from the French embassy in Singapore. Not to forget are the three research centres, namely Centre for Quantum Technologies (CQT) in Singapore, Laboratoire Kastler Brossel (LKB) in Paris, France and Institut non Linéaire de Nice (INLN) in Nice, France, that have supported me with comfortable working environment and huge amount of computational resources. Finally, I would like to thank my parents and sisters for their kind understanding on the little time that I spent with them in my course of study, my fiancée Xiao Ling for her company throughout the years, as well as friends who have given me

support and encouragement.

This thesis mainly covers (not exclusively) results published in Phys. Rev. A **80**, 043411 (2009) and Phys. Rev. B **80**, 245118 (2009). Both papers were subsequently selected for Virtual Journal of Atomic Quantum Fluids.

Contents

Abstract

A honeycomb lattice half-filled with fermions has its excitations described by massless Dirac fermions, e.g. graphene. We investigate the experimental feasibility of loading ultracold fermionic atoms in a two-dimensional optical lattice with honeycomb structure and we go beyond graphene by addressing interactions between fermions in such a lattice. We analyze in great detail the optical lattice generated by the coherent superposition of three coplanar running laser waves with respective angles $2\pi/3$. The corresponding band structure displays Dirac cones located at the corners of the Brillouin zone and the excitations obey Weyl-Dirac equations. In an ideal honeycomb lattice, the presence of Dirac cones is a consequence of the point group symmetry and it is independent of the optical potential depth. We obtain the important parameter that characterizes the tight-binding model, the nearest-neighbor hopping parameter t, as a function of the optical lattice parameters. Our semiclassical instanton method is in excellent agreement with an exact numerical diagonalization of the full Hamilton operator in the tight-binding regime. We conclude that the temperature range needed to access the Dirac fermions regime is within experimental reach. We also analyze imperfections in the laser configuration as they lead to optical lattice distortions which affect the Dirac fermions. We show that the Dirac cones do survive up to some critical intensity or angle mismatches which are easily controlled in actual experiments. The presence of the Dirac cones can be understood in terms of geometrical configuration of hopping

parameters. In the tight-binding regime, we predict, and numerically confirm, that these critical mismatches are inversely proportional to the square root of the optical potential strength. To study the interactions between fermions, we focus on attractive fermionic Hubbard model on a honeycomb lattice. The study is carried out using determinant quantum Monte Carlo algorithm and we extract the frequency-dependent spectral function using maximum entropy method. By increasing the interaction strength U (relative to the hopping parameter t) at half-filling and zero temperature, the system undergoes a quantum phase transition at $U_c/t \approx 5$ from a disordered phase to a phase displaying simultaneously superfluid behavior and density order. Meng *et al.* reported recently a lower critical strength and they showed that the system first enters a pseudo-spin liquid phase before becoming superfluid. We attributed the discrepancy in the numbers to the "relatively high" temperature at which our simulations were performed. We were not able to identify the pseudo-spin liquid phase because computing the relevant time-displaced pair Green's function is computationally too expensive for us. Doping away from half-filling, and increasing the interaction strength at finite but low temperature T, the system appears to be a superfluid exhibiting a crossover between a BCS and a molecular regime. These different regimes are analyzed by studying the spectral function. The formation of pairs and the emergence of phase coherence throughout the sample are studied as U is increased and T is lowered.

List of Tables

List of Figures

List of Symbols[1]

a	Lattice constant	9
$\boldsymbol{a}_1, \boldsymbol{a}_2$	Primitive vectors	8
A, B	Sublattice of a honeycomb lattice	9
$\{a, b\}$	$\equiv ab + ba$, anti-commutator.	*
$[a, b]$	$\equiv ab - ba$, commutator.	*
$A(\omega)$	Spectral function	95
$\boldsymbol{b}_1, \boldsymbol{b}_2$	Reciprocal primitive vectors	11
$\mathcal{B}$	Bravais lattice	8
$\tilde{\mathcal{B}}$	Reciprocal lattice	11
β	Inverse temperature	89
$\boldsymbol{c}_i$	Vector that connect an A site to its neigboring B site	9
δ	Light detuning from atomic resonance	33
$D_{\boldsymbol{ij}}$	Density-density correlation functions	93
$\Delta^\dagger_{\boldsymbol{i}}(\Delta_{\boldsymbol{i}})$	Pair creation (annihilation) operator at site $\boldsymbol{i}$	94
$\boldsymbol{e}_x, \boldsymbol{e}_y$	Unit vectors in the x, y-directions	*
E_R	Recoil energy of atom	44
$\epsilon_{\pm,\boldsymbol{k}}$	Dispersion relation of tight-binding model	24
$f_{\boldsymbol{i}\sigma}(f^\dagger_{\boldsymbol{i}\sigma})$	Annihilation(Creation) operator of spin-σ fermion at site $\boldsymbol{i}$	25
$G(\tau)$	On-site Green's function	95

[1]The page where a given symbol are defined/introduced is listed at the rightmost column. When the definition is general, page number is given as *.

$G^{\mathrm{p}}_{\boldsymbol{ij}}$	Pair Green's function	94
$\mathcal{G}$	Point group operation	15
$\hbar_e$	Effective Planck's constant	45
H	Hamilton operator	*
$\mathcal{H}$	Position representation of the Hamilton operator	*
H_K	Kinetic energy in the Hubbard model	87
H_V	Interaction energy in the Hubbard model	88
$\boldsymbol{J_i}$	Pseudo-spin vector at site $\boldsymbol{i}$	116
$\boldsymbol{k}$	Bloch wave vector in reciprocal space	10
K, K'	Dirac points of a honeycomb lattice	12
L	Linear dimension of finite lattice	*
N	$= 2L^2$, total number of lattice sites	*
N_c	$= L^2$, total number of primitive unit cells	*
Ω	First Brillouin zone in reciprocal space	10
P_{s}	Pair structure factor	94
$\psi_{\boldsymbol{k}}(\boldsymbol{r})$	$\equiv \langle \boldsymbol{r} \vert \psi_{\boldsymbol{k}} \rangle$, Bloch wave function	12
$\psi(\boldsymbol{r})$	$\equiv \langle \boldsymbol{r} \vert \psi \rangle$, position wave function of state $\vert \psi \rangle$	*
$\boldsymbol{r}$	Position vector of a fermionic particle	*
$\boldsymbol{R}$	Bravais lattice vector	8
ρ	Average total fermionic density	88
ρ_{p}	Density of on-site pairs	127
S_{dw}	Density wave structure factor	94
$\boldsymbol{S_i}$	Spin vector at site $\boldsymbol{i}$	115
Σ	Diamond-shaped primitive unit cell in real space	8
$T_{\boldsymbol{R}}$	Translation operator of a Bravais lattice	10
t_i	Tunneling parameter in the i-th direction.	24
t	Tunneling amplitude in an ideal honeycomb lattice	*

List of Abbreviations

1st BZ	First Brillouin zone
2D	Two-dimensional
AF	Antiferromagnetic
BCS	Bardeen-Cooper-Schrieffer
BEC	Bose-Einstein condensation
BKT	Berezinskii-Kosterlitz-Thouless
DQMC	Determinantal quantum Monte Carlo
DW	Density wave
FAHM	Fermionic attractive Hubbard model
FET	Field effect transistor
FRHM	Fermionic repulsive Hubbard model
HS	Hubbard-Stratonovich
HOT	Holographic optical tweezer
LCAO	Linear combinations of atomic orbitals
LHO	Local harmonic oscillator
MaxEnt	Maximum entropy method
PDF	Probability distribution function
PSL	Pseudo-spin liquid
QMC	Quantum Monte Carlo
QPT	Quantum phase transition

RPA	Random phase approximation
SC	Superconductor
SF	Superfluid

Chapter 1

Introduction

In 2004, researchers in Manchester successfully isolated single-atomic planes of carbon atoms through the mechanical exfoliation of graphite using Scotch tape [1]. Since then, graphene has attracted much attention due to theoretical interests in fundamental physics as well as its potential applications in electronics, such as the recently announced graphene-based field effect transistors (FETs) that operate at a much higher speed (100 GHz) compared to conventional silicon-based FETs [2].

In these free-standing graphene sheets, the hybridized sp^2-orbitals lead to a planar honeycomb structure of the carbon atoms with σ-bonds between nearest neighbors, separated by 1.42 Å. The unaffected p_z-orbitals, which are perpendicular to the planar structure, bind covalently to form a π-band. Since each carbon atom has one valence electron from the p_z-orbital, the π-band is half-filled. The energy band spectrum shows "conical points" where the valence and conduction bands are connected, and the Fermi energy at half-filling is located precisely at these points as only half of the available states are filled. Around these points, the energy varies proportionally to the modulus of the wave-vector and the excitations (holes or particles) of the system are described by two-dimensional massless Weyl-Dirac fermions, propagating at about one 300th of the speed of light [3, 4]. Graphene

sheets thus allow for table-top experiments on two-dimensional (2D) relativistic field theories, with a replacement of the velocity of light by the so-called *Fermi velocity* in graphene. Triggered by the Manchester discovery, an intense activity has flourished in the field, and continues to flourish, as witnessed by Refs. [5–10], for example. The reported and predicted phenomena include the Klein paradox (the perfect transmission of relativistic particles through high and wide potential barriers) [8], the anomalous quantum Hall effect induced by Berry phases [4, 11], and its corresponding modified Landau levels [12].

The attempt to understand graphene physics is not without difficulty. For example, intrinsic ripples have been observed in suspended graphene [13, 14]. As a consequence, there are fluctuations in the nearest-neighbor hopping amplitudes that depend on the deformation tensor [9]. This inhomogeneity may be taken into account using an effective Dirac-like Hamiltonian but with the addition of vector potentials. Other complications include electron-phonon interactions [15] and the presence of a charge inhomogeneity in graphene [16].

On the other hand, the experimental successes in achieving Bose-Einstein condensation (BEC) [17–19] and Fermi degeneracy [20–22] in ultracold atomic gases enable us to focus on the particle statistics and the inter-particle interactions. Following the discovery of the stability of Li_2 molecules despite their high vibrational excitation [23], much effort has been dedicated to achieve condensation of fermionic pairs. Various experiments were performed to study fermionic superfluidity, such as the direct demonstration through the observation of vortices [24]. Other exciting discoveries include the population imbalance in fermionic mixtures [25–29] and the (indirect) observation of fermionic superfluidity in optical lattice [30]. These recent advances in experiments with cold atoms [31] thus offer us the possibility to simulate condensed-matter phenomena by loading ultracold atoms into optical lattices without the complications of graphene. The great advantage is that

the relevant parameters (shape and strength of the light potential, atom-atom interaction strength via Feshbach resonances [32], etc.) are accessible and can be accurately controlled while spurious effects that destroy the quantum coherence are absent, such as the analog of the electron-phonon interaction. Cold atom experiments thus provide us an exact physical realization of theoretical models like the Hubbard model.

In Ref. [33], Zhu *et al.* proposed to observe Dirac fermions with cold atoms in a honeycomb optical lattice. In the first part of this work, we analyze in details this scheme that is capable of reproducing in atomic physics the unique situation found in graphene. It consists of creating a two-dimensional honeycomb optical lattice and loading it with ultracold fermions like the neutral ^{6}Li atoms. We calculate the important nearest-neighbor hopping parameter in terms of optical lattice parameters and conclude that the temperature range needed to access the Dirac fermion regime is within experimental reach. We further consider imperfections in the laser configurations that lead to distortions in the optical lattice. Our analysis shows that Dirac fermions survive up to some critical beam intensity imbalance or aligment angle mismatch in the experimental setup, which are easily controlled in actual experiments. We also explain the relation between the critical values and the optical potential strength. The existence of Dirac fermions in a perfect honeycomb can be accounted for by the point group symmetry, but in a distorted lattice, it is explained by the geometrical relation of hopping parameters in the tight-binding regime.

In the second part, we address the question of attractive interactions between the atoms. Specifically, we study the phenomenon of BCS-BEC crossover in the honeycomb lattice as there are some unsolved questions that cannot be studied using graphene. Such an interacting system can be described by a Hubbard model and this model (or effective models that are derived from it, such as the t-J model)

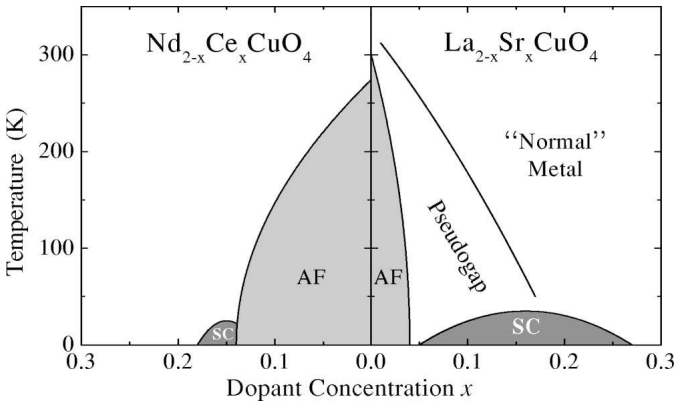

Figure 1.1: Schematic phase diagram of hole-doped (right side) and electron-doped (left side) high-T_c superconductors. The various regions shown are superconductor (SC), antiferromagnetic (AF), pseudogap and normal metals. Reprinted figure with permission from Ref. [34] as follows: Andrea Damascelli *et al.*, Reviews of Modern Physics **75** 473 (2003) (`http://rmp.aps.org/abstract/RMP/v75/i2/p473_1`). Copyright (2003) by the American Physical Society.

is believed to be the underlying model for high-T_c superconductors [35, 36]. In a typical high-T_c superconductor, there are layers of CuO_2 planes that are separated by some 'spacer' elements, e.g. Ca, Sr and Y. This CuO_2 plane is approximated by a simple square lattice of lattice parameter being roughly 3.84 Å, with the Cu atoms sit at the lattice points and the O atoms at the midpoints between nearest Cu atoms. When the Hubbard model on a square lattice is half-filled, the nesting of the Fermi surface generally leads to ordered phases (such as the antiferromagnetic phase in Fig. 1.1) even for arbitrarily small interaction strengths [37]. Using t-J model and introducing slave boson to enforce the constraint against double occupancy, the superconducting phase (SC) is shown to emerge by doping the antiferromagnetic Mott insulator [35]. On the contrary, in a honeycomb lattice, the peculiar nature of the Fermi surface (i.e. reduced to a finite number of Dirac points) leads to special physics at and around half-filling. In this honeycomb lattice and with repulsive interactions, Paiva *et al.* have found a quantum phase transition (QPT) at half-filling between a metallic and an ordered phase when the interaction strength is increased [38]. However, when the attractive system

is slightly doped away from half-filling, the nature of the system is yet to be determined. Since graphene has a single interaction strength that cannot be tuned with present technology[1], this QPT at half-filling is not accessible in experiments with graphene but is in the reach of cold atom experiments.

The study of interactions is carried out through determinant quantum Monte Carlo simulations of the attractive fermioninc Hubbard model. We determine the QPT to occur at around $5.0 < U_c/t < 5.1$, where U_c is the critical interaction strength. Doping away from half-filling, and increasing the interaction strength at finite but low temperature T, the system appears to be a superfluid exhibiting a crossover between a Bardeen-Cooper-Schrieffer (BCS) and a molecular regime at a doping as low as 5%. These different regimes are analyzed by studying the spectral function. The formation of pairs and the emergence of phase coherence throughout the sample are studied as U is increased and T is lowered.

After our work on interacting fermions on a honeycomb lattice was published [42], it was brought to our attention that before becoming an antiferromagnetic Mott insulator (density-ordered superconductor) with repulsive (attractive) interactions, the interacting system on a half-filled honeycomb lattice first enters a spin liquid (pseudo-spin liquid) phase, followed by the ordered phase as the interaction strength increases [43–46]. Unfortunately, to probe such a three-step transition, we are required to measure (imaginary)-time-displaced pair correlations, which are too time-consuming using our algorithm and not feasible within our time frame. In Chapter 6, we will explain in more details the findings of Ref. [43] in order to make the picture more complete, even though it is not our work.

[1]The on-site interaction strength in graphene is estimated to be $U \approx 3.6t$ based on experiments performed on polyacetylene [10, 39], but Refs [40, 41] predicted graphene to be a marginal Fermi liquid with strong unscreened Coulomb interactions between the electrons based on renormalization group theory. Since we are not aware of any experimental evidence showing graphene to be an AF Mott insulator, which is a phase characteristic of half-filled bipartite Hubbard model with strong repulsion, we adopt the view point that graphene is weakly interacting.

Chapter 2

General properties of a honeycomb lattice

2.1 Lattice and symmetries

A solid crystal, such as a graphene sheet, consists of a periodic arrangement of atoms. The positively-charged nuclei (with screening from the other electrons) form attractive centers for the valence electrons. This periodic potential felt by the electrons, and similarly the optical potential experienced by the trapped atoms in an optical lattice, is most conveniently described in terms of a *crystal structure*. For simplicity, we consider a crystal structure as composed of a periodic array of sites in space, generated by the repeated translations of a primitive unit cell called *basis*. More specifically, it can be viewed as a Bravais lattice with the Bravais lattice points replaced by identical primitive unit cells. A primitive unit cell can contain more than one lattice site, and the lattice sites within a unit cell can have different local environment, such as sites A and B in the primitive unit cell Σ in Fig. 2.1, in contrast to the Bravais lattice points that have identical local environment. A suitable choice of lattice sites is the positions of atoms in a solid

crystal and the optical potential minima in an optical potential. With this choice, the positions of carbon atoms in a graphene sheet and the positions of the potential wells in an optical lattice (discussed in Chapter 3) form a lattice with honeycomb structure, which is the core lattice studied in this work. For convenience sake and to conform to common terminology used in literature, we will now refer to a lattice with honeycomb structure as a honeycomb lattice. For more pedagogic details on crystallography, readers are advised to read Ref. [47].

A periodic potential $V(\boldsymbol{r})$ with honeycomb structure, where $\boldsymbol{r}$ is the position vector of a single electron in a graphene sheet or a trapped atom in an optical lattice, may be represented pictorially by a honeycomb lattice (Fig. 2.1). Its underlying Bravais lattice is a triangular lattice,

$$\mathcal{B} = \big\{ m_1\boldsymbol{a}_1 + m_2\boldsymbol{a}_2 \;\big|\; m_1, m_2 = 0, \pm 1, \pm 2, \dots \big\}, \tag{2.1}$$

defined in such a way that the value of the periodic potential remains unchanged by any displacement $\boldsymbol{R} \in \mathcal{B}$, $V(\boldsymbol{r} + \boldsymbol{R}) = V(\boldsymbol{r})$. The two linearly independent primitive vectors are parameterized by

$$\left.\begin{matrix} \boldsymbol{a}_1 \\ \boldsymbol{a}_2 \end{matrix}\right\} = \Lambda \frac{\sqrt{3}\boldsymbol{e}_x \mp \boldsymbol{e}_y}{2}, \tag{2.2}$$

where $\Lambda = \big|\boldsymbol{a}_1\big| = \big|\boldsymbol{a}_2\big|$ is the common length of the Bravais primitive vectors. The choice of primitive unit cell is not unique and we have opted for the diamond-shaped primitive cell Σ delineated by the two primitive lattice vectors for convenience sake (Fig. 2.1). An alternative choice that incorporates the symmetry properties of the Bravais lattice is the *Wigner-Seitz cell*; see Fig. 2.3. It is defined with respect to a Bravais lattice point as the region of space that is closer to that point than any other Bravais lattice point; see p. 73–75 of Ref [47].

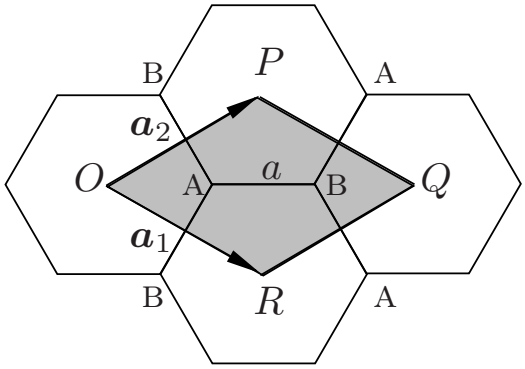

Figure 2.1: The underlying Bravais lattice $\mathcal{B}$ of a two-dimensional honeycomb lattice is the two-dimensional triangular Bravais lattice with a two-point basis A and B. The grey-shaded area is the primitive cell Σ. The honeycomb lattice parameter a is defined as the distance between nearest-neighbor sites.

The basis contains two sites, labeled as A and B sites, hence a honeycomb lattice is commonly known as a bipartite lattice or a triangular lattice with a two-point basis. Each lattice site has three nearest neighbors that belong to the other sublattice. The three vectors that connect an A site to its three nearest neighbors, which also translate sublattice A to sublattice B, are parameterized by

$$\begin{aligned}
\boldsymbol{c}_1 &= \frac{1}{3}(\boldsymbol{a}_1 + \boldsymbol{a}_2) = a\boldsymbol{e}_x \,, \\
\boldsymbol{c}_2 &= \frac{1}{3}(\boldsymbol{a}_2 - 2\boldsymbol{a}_1) = a\frac{-\boldsymbol{e}_x + \sqrt{3}\boldsymbol{e}_y}{2} \,, \\
\boldsymbol{c}_3 &= \frac{1}{3}(\boldsymbol{a}_1 - 2\boldsymbol{a}_2) = a\frac{-\boldsymbol{e}_x - \sqrt{3}\boldsymbol{e}_y}{2} \,,
\end{aligned} \tag{2.3}$$

where $a = \left|\boldsymbol{c}_j\right| = \Lambda/\sqrt{3}$ is the lattice parameter[1]. Furthermore, a is the distance from an A site to a neighboring B site, or the distance from the center of the hexagon of lattice sites to any one of its corners.

It is important to study the symmetry properties of the lattice structure because physical problems can be greatly simplified through symmetry-based arguments.

[1] According to conventions in crystallography, a lattice parameter (or lattice constant) refers to the constant distance between unit cells, i.e. Λ. Here, we instead define it as the nearest-neighbor distance a for convenience in later calculations.

The lattice remains invariant under certain coordinate transformations induced by the associated symmetry transformation operators. Correspondingly, the periodic potential, and hence the single-particle Hamilton operator H, is invariant under such transformations (the transformations are norm-preserving such that the kinetic energy operator is invariant as well). The implication of the invariance of H is that we can label the eigenstates of the Hamilton operator by the eigenvalues of the symmetry operators; see Appendix A.1. If there are several commuting symmetry operators, all of which commute with H, the eigenstates of H can be chosen as the simultaneous eigenstates of these symmetry operators [48].

The symmetry operators that commute with H generally involve translations, rotations, reflections, and inversions [49]. The complete set of symmetry operators that transform the lattice into itself is called the *space group*. Within the space group of a honeycomb lattice, we pay special attention to two subgroups called the *translation group* and the *point group*.

2.2 Translation group of a honeycomb lattice

In the previous section, we have already mentioned the translation group of a honeycomb lattice, i.e. the Hamilton operator is invariant under any translation $\boldsymbol{R}$ that belongs to the underlying Bravais lattice; see Eq. (2.1). The set of translation operators are

$$T_{\boldsymbol{R}} = \mathrm{e}^{-\frac{\mathrm{i}}{\hbar}\boldsymbol{P}\cdot\boldsymbol{R}} \quad \text{with} \quad \boldsymbol{R} \in \mathcal{B}, \tag{2.4}$$

where $\boldsymbol{P}$ is the two-dimensional momentum operator. The corresponding eigenvalues are given by $\mathrm{e}^{-\mathrm{i}\boldsymbol{k}\cdot\boldsymbol{R}}$ (see Appendix A.2), where $\boldsymbol{k}$ is a wave vector that lies in the Wigner-Seitz cell of the reciprocal lattice, which is more commonly known as the *first Brillouin zone* (1st BZ); see Fig. 2.2.

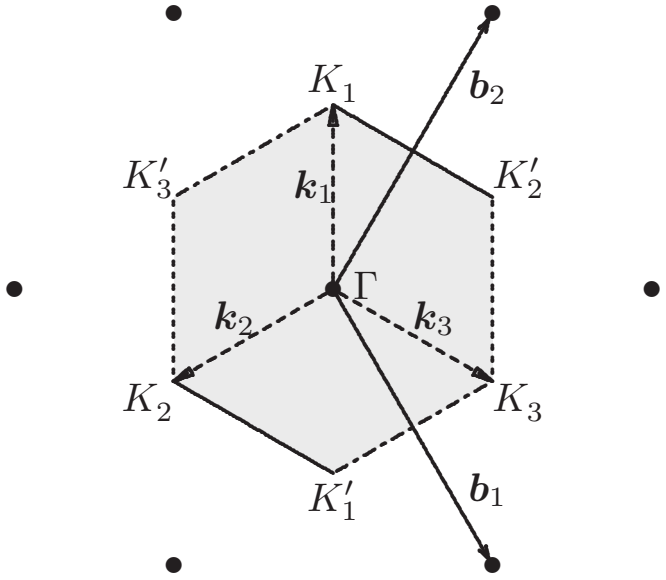

Figure 2.2: The triangular reciprocal lattice $\tilde{\mathcal{B}}$ associated with the triangular Bravais lattice of Fig. 2.1 and Fig. 3.3. It is spanned by the reciprocal primitive vectors $\boldsymbol{b}_1$ and $\boldsymbol{b}_2$ of Eq. (2.7), and is also a triangular lattice (as indicated by the full dots). The shaded region identifies the first Brillouin zone Ω which is here a regular hexagon. Its center is conventionally named Γ in the solid-state literature. Opposite edges are in fact identical as they only differ by a translation in the reciprocal lattice. This feature is emphasized by drawing the identical edges with the same (solid, dashed or dash-dotted) line. For the same reason, the three corners K_a $(a = 1, 2, 3)$ are to be identified with each other, and likewise the three corners K_a' are really only one point in Ω. Thus only two of the six corners, collectively labeled as K and K' and known as the Dirac points, are different. Also shown are the wave vectors of the three coplanar plane waves (dashed arrows; see Eq. (2.8)).

The reciprocal lattice $\tilde{\mathcal{B}}$ is a regular pattern in $\boldsymbol{k}$ space defined by linear combinations of the reciprocal primitive vectors $\boldsymbol{b}_1$ and $\boldsymbol{b}_2$ with integer coefficients,

$$\tilde{\mathcal{B}} = \big\{ n_1\boldsymbol{b}_1 + n_2\boldsymbol{b}_2 \;\big|\; n_1, n_2 = 0, \pm 1, \pm 2, \dots \big\}. \tag{2.5}$$

The $\boldsymbol{b}_i$s are constructed based on the orthogonal relation

$$\boldsymbol{a}_i \cdot \boldsymbol{b}_j = 2\pi\delta_{ij} \;\text{ for }\; i, j = 1, 2, \tag{2.6}$$

which in turn implies that the Bravais lattice $\mathcal{B}$ and the reciprocal lattice $\tilde{\mathcal{B}}$ con-

stitute dual spaces. From Eq. (2.2), we have

$$\left.\begin{matrix}\boldsymbol{b}_1\\ \boldsymbol{b}_2\end{matrix}\right\} = \kappa\frac{\boldsymbol{e}_x \mp \sqrt{3}\boldsymbol{e}_y}{2} \tag{2.7}$$

with $\kappa = \left|\boldsymbol{b}_i\right| = 4\pi/(\sqrt{3}\Lambda) = 4\pi/(3a)$.

A domain in reciprocal space of utmost importance is the first Brillouin zone Ω. It is a *regular* hexagon but with the subtle feature that opposite edges are to be identified with each other since they can be related by a displacement vector in $\tilde{\mathcal{B}}$ [2]. By the same token the three corners K_a (respectively K'_a) have to be identified with one another and we collectively denote them by K (respectively K'). These two different corners K and K' are known as the Dirac points in the graphene literature for a reason that will become clear in the next two sections. As we shall see in Chapter 3, upon denoting $\boldsymbol{K} \equiv \boldsymbol{K}_1$ and $\boldsymbol{K'} \equiv \boldsymbol{K}'_1$, their positions in Ω happen to be the wave vectors $\boldsymbol{k}_i$ of the lasers that generate the optical honeycomb potential,

$$\boldsymbol{K} = -\boldsymbol{K'} = \frac{1}{3}(\boldsymbol{b}_2 - \boldsymbol{b}_1) = \boldsymbol{k}_1 \tag{2.8}$$

and $\boldsymbol{K}_2 = \boldsymbol{k}_2 = \boldsymbol{K} - \boldsymbol{b}_2$, $\boldsymbol{K}_3 = \boldsymbol{k}_3 = \boldsymbol{K} + \boldsymbol{b}_1$, as well as $\boldsymbol{K_a} = -\boldsymbol{K}'_a$.

At this point, it is worth mentioning *Bloch's theorem* that associates each eigenstate $|\psi_{\boldsymbol{k}}\rangle$ of H with a wave vector $\boldsymbol{k} \in \Omega$ such that

$$\psi_{\boldsymbol{k}}(\boldsymbol{r} - \boldsymbol{R}) = \mathrm{e}^{-\mathrm{i}\boldsymbol{k}\,\cdot\,\boldsymbol{R}}\psi_{\boldsymbol{k}}(\boldsymbol{r}), \tag{2.9}$$

where $\langle\boldsymbol{r}|H|\psi_{\boldsymbol{k}}\rangle = \mathcal{H}\psi_{\boldsymbol{k}}(\boldsymbol{r}) = \epsilon_{\boldsymbol{k}}\psi_{\boldsymbol{k}}(\boldsymbol{r})$ and $\epsilon_{\boldsymbol{k}}$ is the eigenenergy of H. It is easy to see that Eq. (2.9) is simply a consequence of the previous discussion that an

[2] In Appendix A.2, either $k = -\frac{\pi}{a}$ or $k = \frac{\pi}{a}$ is kept in the range of k inclusively for the same reasoning.

energy eigenstate is simultaneously an eigenstate of the translation operators, i.e.

$$\left.\begin{aligned} T_{\boldsymbol{R}}|\psi_{\boldsymbol{k}}\rangle &= \mathrm{e}^{-\mathrm{i}\boldsymbol{k}\cdot\boldsymbol{R}}|\psi_{\boldsymbol{k}}\rangle \\ \langle\boldsymbol{r}|T_{\boldsymbol{R}}|\psi_{\boldsymbol{k}}\rangle &= \langle\boldsymbol{r}-\boldsymbol{R}|\psi_{\boldsymbol{k}}\rangle = \psi_{\boldsymbol{k}}(\boldsymbol{r}-\boldsymbol{R}) \end{aligned}\right\} \Rightarrow \psi_{\boldsymbol{k}}(\boldsymbol{r}-\boldsymbol{R}) = \mathrm{e}^{-\mathrm{i}\boldsymbol{k}\cdot\boldsymbol{R}}\psi_{\boldsymbol{k}}(\boldsymbol{r}). \quad (2.10)$$

From Eq. (2.9), we obtain a function $u_{\boldsymbol{k}}(\boldsymbol{r})$ that has the periodicity of the Bravais lattice,

$$\begin{aligned} u_{\boldsymbol{k}}(\boldsymbol{r}) &\equiv \mathrm{e}^{-\mathrm{i}\boldsymbol{k}\cdot\boldsymbol{r}}\psi_{\boldsymbol{k}}(\boldsymbol{r}) \\ &= \mathrm{e}^{-\mathrm{i}\boldsymbol{k}\cdot(\boldsymbol{r}-\boldsymbol{R})}\psi_{\boldsymbol{k}}(\boldsymbol{r}-\boldsymbol{R}) \quad \text{from Eq. (2.9)} \\ &= u_{\boldsymbol{k}}(\boldsymbol{r}-\boldsymbol{R}). \end{aligned} \quad (2.11)$$

Hence, we arrive at an alternate formulation of Bloch's theorem, which is also frequently called *Floquet's theorem* (since it was first proven by Floquet in the periodic one-dimensional system),

$$\psi_{\boldsymbol{k}}(\boldsymbol{r}) = \mathrm{e}^{\mathrm{i}\boldsymbol{k}\cdot\boldsymbol{r}}u_{\boldsymbol{k}}(\boldsymbol{r}). \quad (2.12)$$

This form of a single-particle wave function is more useful in the analysis of point group symmetry of the Bravais lattice, which is carried out in the next section.

Since $\boldsymbol{k}$ is a good quantum number, the eigenenergy $\epsilon_{\boldsymbol{k}}$ of $|\psi_{\boldsymbol{k}}\rangle$ is often plotted as a function of $\boldsymbol{k}$, either along certain high symmetry lines in the $\boldsymbol{k}$-space or on a 2D plane. When we restrict the plotted $\boldsymbol{k}$ to lie within the 1st BZ (also known as *reduced zone scheme*), we can clearly see that there are allowed and forbidden energy ranges. These allowed energy ranges are often called *energy bands*. The earliest calculation of the band structure of graphite (multi-layers of graphene) was provided by Wallace [50].

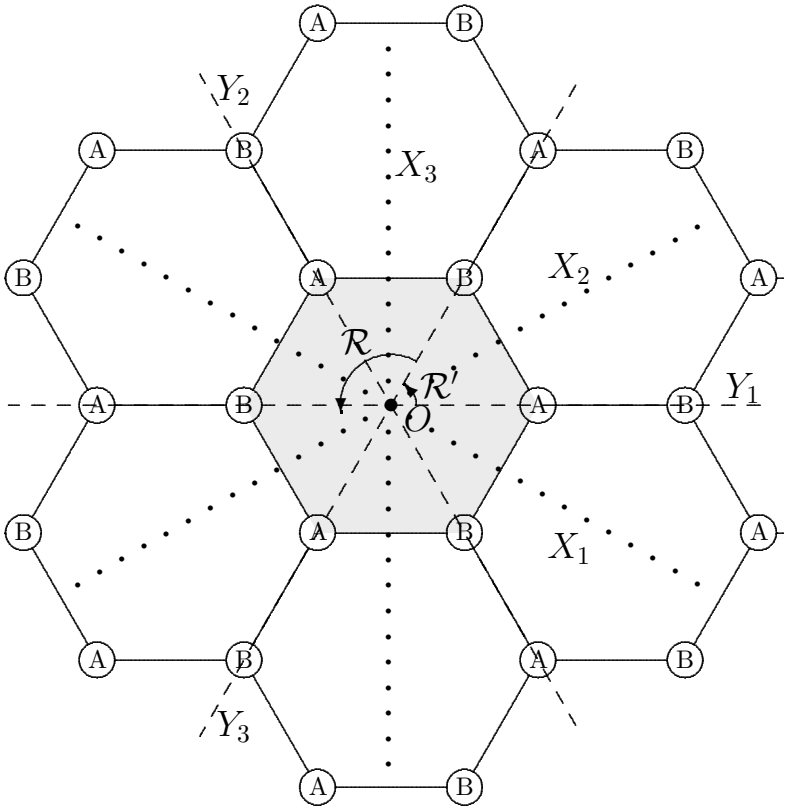

Figure 2.3: Rotations and reflections that belongs to the point group of a honeycomb lattice. The shaded hexagon centered at origin O is the Wigner-Seitz cell, reflecting the symmetries of the lattice. The dotted and dashed lines represent the mirror planes of reflections X_i and Y_i respectively.

2.3 Point group of a honeycomb lattice

The point group of a honeycomb lattice can be obtained by setting all translations in its space group to be zero. Refering to Fig. 2.3, we define the origin O as the center of the hexagonal Wigner-Seitz cell with six honeycomb lattice sites sit at the corners of this hexagon. The point group is then built up by the following operations (besides identity operation E) [48, 49]:

- $\mathcal{R}$ and its inverse $\mathcal{R}^{-1}$, anti-clockwise *rotations* of $\frac{2\pi}{3}$ and $\frac{4\pi}{3}$ respectively about the origin O,

- Y_1, Y_2, Y_3, *reflections* in lines connecting opposite corners of the hexagon cen-

tered at the origin O,

- $\mathcal{R}'$ and its inverse $\mathcal{R}'^{-1}$, anti-clockwise *rotations* of $\frac{\pi}{3}$ and $-\frac{\pi}{3}$ respectively about the origin O,

- X_1, X_2, X_3, *reflections* in lines connecting midpoints of opposite edges of the hexagon centered at the origin O,

- and *inversion* $\mathcal{I}$ that takes $\boldsymbol{r}$ into $-\boldsymbol{r}$.

The last three sets of operations interchange the roles of A and B sites. Hence, the operations are included (not included) in the point group if the two sublattices are treated as equivalent (inequivalent) and the order of the point group is 12 (6). According to Schoenflies system of notation, the point group is called C_{6v} (C_{3v}); see p. 54–56 of Ref. [48]. Some of the point group operations are shown in Fig. 2.3.

Consider the action of a point group operation $\mathcal{G}$, with the corresponding transformation operator $P_{\mathcal{G}}$, on a Bloch wave function $\psi_{\boldsymbol{k}}(\boldsymbol{r})$,

$$P_{\mathcal{G}}\psi_{\boldsymbol{k}}(\boldsymbol{r}) = \psi_{\boldsymbol{k}}(\mathcal{G}^{-1}\boldsymbol{r}) = \mathrm{e}^{\mathrm{i}\boldsymbol{k}\cdot(\mathcal{G}^{-1}\boldsymbol{r})}u_{\boldsymbol{k}}(\mathcal{G}^{-1}\boldsymbol{r}) = \mathrm{e}^{\mathrm{i}(\mathcal{G}\boldsymbol{k})\cdot\boldsymbol{r}}u_{\boldsymbol{k}}(\mathcal{G}^{-1}\boldsymbol{r}). \tag{2.13}$$

Since $\mathcal{G}^{-1}\boldsymbol{R} \in \mathcal{B}$ if $\boldsymbol{R} \in \mathcal{B}$, we can obtain another function[3] $u'_{\mathcal{G}\boldsymbol{k}}(\boldsymbol{r}) \equiv u_{\boldsymbol{k}}(\mathcal{G}^{-1}\boldsymbol{r})$ that has the periodicity of the Bravais lattice,

$$\begin{aligned} u'_{\mathcal{G}\boldsymbol{k}}(\boldsymbol{r}-\boldsymbol{R}) &= u_{\boldsymbol{k}}(\mathcal{G}^{-1}\boldsymbol{r} - \mathcal{G}^{-1}\boldsymbol{R}) \\ &= u_{\boldsymbol{k}}(\mathcal{G}^{-1}\boldsymbol{r}) \quad \text{from Eq. (2.11)} \\ &= u'_{\mathcal{G}\boldsymbol{k}}(\boldsymbol{r}). \end{aligned} \tag{2.14}$$

[3]When there is no degeneracy, u' differs from u only by a phase factor. However, when there is degeneracy, u' can be a linear combination of the degenerate functions u; see Ref. [48].

Representation	Class		
	E	$\mathcal{R}$, $\mathcal{R}^{-1}$	X_1, X_2, X_3
$\Gamma^{(1)}$	1	1	1
$\Gamma^{(2)}$	1	1	-1
$\Gamma^{(3)}$	2	-1	0

Table 2.1: Character table of small representations of the group of $\boldsymbol{K}(\boldsymbol{K}')$. Representations $\Gamma^{(1)}$ and $\Gamma^{(2)}$ are one-dimensional representations while $\Gamma^{(3)}$ is a two-dimensional representation. Of special interest is $\Gamma^{(3)}$ for degenerate eigenstates.

The resulting equation,

$$P_{\mathcal{G}}\psi_{\boldsymbol{k}}(\boldsymbol{r}) = \mathrm{e}^{\mathrm{i}(\mathcal{G}\boldsymbol{k})\cdot\boldsymbol{r}}u'_{\mathcal{G}\boldsymbol{k}}(\boldsymbol{r}) \equiv \psi'_{\mathcal{G}\boldsymbol{k}}(\boldsymbol{r}), \tag{2.15}$$

implies that the point group operation acts on an energy eigenfunction $\psi_{\boldsymbol{k}}(\boldsymbol{r})$ with wave vector $\boldsymbol{k}$ to produce another eigenfunction $\psi'_{\mathcal{G}\boldsymbol{k}}(\boldsymbol{r})$, also in Bloch form, but with its wave vector transformed to $\mathcal{G}\boldsymbol{k}$. The search for eigenenergies can thus be simplified by finding all the symmetry-related $\boldsymbol{k}$ vectors with the associated eigenfunctions of the same energy. An example would be to consider the situation where the two sublattices are inequivalent, such as when site A and site B have different potential depths[4]; see Sec. 4.1. The point group is reduced to identity operation E, rotations $\mathcal{R}$ and $\mathcal{R}^{-1}$ as well as reflections Y_1, Y_2 and Y_3. Yet, the Bloch wave functions at $\boldsymbol{K}$ and $\boldsymbol{K}'$ are still degenerate because they are connected by the reflections Y_i.

The action of all point group operators on a given $\boldsymbol{k}$ generate a set of wave vectors known as the *star* of $\boldsymbol{k}$, e.g. all the corners of 1st BZ in Fig. 2.2 belong to the star of $\boldsymbol{K}$. We pay special attention to group operations that leave a given $\boldsymbol{k}$ invariant up to a reciprocal lattice vector, i.e. $\mathcal{G}\boldsymbol{k} \to \boldsymbol{k} + \boldsymbol{b}, \boldsymbol{b} \in \tilde{\mathcal{B}}$, and these operators form a subgroup of the point group called the *group of the wave vector*

[4]We have assumed that the only changes made are the potential depths. There is no change to the local environment around the lattice sites.

Matrix representation of $\Gamma^{(3)}$
$E = \begin{pmatrix} 1 & 0 \\ 0 & 1 \end{pmatrix}$, $\mathcal{R} = \begin{pmatrix} \omega^{-1} & 0 \\ 0 & \omega \end{pmatrix}$, $\mathcal{R}^{-1} = \begin{pmatrix} \omega & 0 \\ 0 & \omega^{-1} \end{pmatrix}$,
$X_1 = \begin{pmatrix} 0 & -\omega^{-1} \\ -\omega & 0 \end{pmatrix}$, $X_2 = \begin{pmatrix} 0 & -\omega \\ -\omega^{-1} & 0 \end{pmatrix}$, $X_3 = \begin{pmatrix} 0 & -1 \\ -1 & 0 \end{pmatrix}$.

Table 2.2: Explicit matrix representation of $\Gamma^{(3)}$. The matrix representations of $\Gamma^{(1)}$ and $\Gamma^{(2)}$ are identical to their characters. The matrix representation of $\Gamma^{(3)}$ can be obtained by first considering the action of the operator on $\boldsymbol{r} = x\boldsymbol{e}_x + y\boldsymbol{e}_y$, followed by the action on the basis functions $\{\frac{1}{\sqrt{2}}(x - \mathrm{i}y), \frac{1}{\sqrt{2}}(x + \mathrm{i}y)\}$.

$\boldsymbol{k}$. We can obtain an irreducible representation of the group of $\boldsymbol{k}$ called the *small representation* by studying the transformation of a function of $\boldsymbol{r}$ under the group operation[5]. The various small representations in a honeycomb lattice have been reported by Lomer [49]. Following the discussion on labeling energy eigenfunctions by eigenvalues of commuting symmetry operators, we can label the various Bloch wave functions $\psi_{\boldsymbol{k}}(\boldsymbol{r})$ by the small representations of $\boldsymbol{k}$. Using Eq. (2.15), we know how do the various $u_{\boldsymbol{k}}(\boldsymbol{r})$ transform among themselves and hence their small representation labels.

Special interests are attached to the point K and K' in the 1st BZ due to the elementary excitations around these points that obey relativistic equation of motion; see Sec. 2.4. Both groups of vector $\boldsymbol{K}$ and $\boldsymbol{K}'$ consist of identity operation E, rotations $\mathcal{R}$ and $\mathcal{R}^{-1}$ as well as reflections X_i [49, 51]. The characters of the small representations and their explicit matrix representations are given in Refs. [49, 51]; see Table 2.1 and 2.2. In real graphene, the p_z-orbital of a carbon atom, which is perpendicular to the graphene sheet, binds covalently with neighboring carbon atoms to form a π-band [10]. Similarly, in a honeycomb optical lattice, the deep optical potential well is crudely approximated by a harmonic potential. The corresponding harmonic oscillator ground state, which is a Gaussian

[5]See p. 18–20 of Ref. [48] on the concept of an *irreducible representation*.

function, contributes to the formation of a tight-binding band that has vanishing density of states at the Dirac points K and K' [52]. Both the π-band in real graphene and the tight-binding band in honeycomb optical lattice contain two degenerate Bloch wave functions of wave vector $\boldsymbol{K}$ (also at $\boldsymbol{K}'$) that belong to the two-dimensional representation $\Gamma^{(3)}$. Consequently, the energy band is gapless; see the next section.

2.3.1 Point group symmetry and honeycomb potential

At this point, it may be suitable to briefly discuss the possible form of a regular honeycomb potential restricted by its point group symmetry [53]. Due to its periodicity, a regular potential with honeycomb structure can be Fourier expanded,

$$\begin{aligned} V(\boldsymbol{r}) &= \sum_{\boldsymbol{k},\boldsymbol{k}'\in\tilde{\mathcal{B}}} \mathrm{e}^{\mathrm{i}\boldsymbol{k}\cdot\boldsymbol{r}}\, V_{\boldsymbol{k},\boldsymbol{k}'}\, \mathrm{e}^{-\mathrm{i}\boldsymbol{k}'\cdot\boldsymbol{r}} \\ &= \sum_{(\boldsymbol{k}-\boldsymbol{k}')\in\tilde{\mathcal{B}}} \mathrm{e}^{\mathrm{i}(\boldsymbol{k}-\boldsymbol{k}')\cdot\boldsymbol{r}}\, V_{\boldsymbol{k}-\boldsymbol{k}'} \\ &= \sum_{n,m=-\infty}^{\infty} \mathrm{e}^{\mathrm{i}(n\boldsymbol{b}_1+m\boldsymbol{b}_2)\cdot\boldsymbol{r}}\, V_{n,m}, \end{aligned} \tag{2.16}$$

where $\boldsymbol{b}_1$ and $\boldsymbol{b}_2$ are the reciprocal primitive vectors defined previously. The matrix element $V_{\boldsymbol{k},\boldsymbol{k}'}$ represents the coupling between a Bloch state $\psi_{\boldsymbol{k}'}(\boldsymbol{r})$ and another state $\psi_{\boldsymbol{k}}(\boldsymbol{r})$ by the potential and the sum $V_{\boldsymbol{k}-\boldsymbol{k}'} = \sum_{\boldsymbol{k}''\in\tilde{\mathcal{B}}} V_{[\boldsymbol{k}''+(\boldsymbol{k}-\boldsymbol{k}')]/2,[\boldsymbol{k}''-(\boldsymbol{k}-\boldsymbol{k}')]/2}$ means that, in terms of the coupling due to potential alone, only the difference in the momentum is physically relevant. The indices (n, m) thus represent the projection of this difference in momentum along $\boldsymbol{b}_1$ and $\boldsymbol{b}_2$. The invariance of the

Type of operation	Matrix representation
Rotations	$\mathcal{R} = \begin{pmatrix} 0 & -1 \\ 1 & -1 \end{pmatrix}, \quad \mathcal{R}^{-1} = \begin{pmatrix} -1 & 1 \\ -1 & 0 \end{pmatrix}$
Reflections	$Y_1 = \begin{pmatrix} 0 & 1 \\ 1 & 0 \end{pmatrix}, \quad Y_2 = \begin{pmatrix} 1 & -1 \\ 0 & -1 \end{pmatrix}, \quad Y_3 = \begin{pmatrix} -1 & 0 \\ -1 & 1 \end{pmatrix}$
Rotations	$\mathcal{R}' = \begin{pmatrix} 1 & -1 \\ 1 & 0 \end{pmatrix}, \quad \mathcal{R}'^{-1} = \begin{pmatrix} 0 & 1 \\ -1 & 1 \end{pmatrix}$
Reflections	$X_1 = \begin{pmatrix} 1 & 0 \\ 1 & -1 \end{pmatrix}, \quad X_2 = \begin{pmatrix} -1 & 1 \\ 0 & 1 \end{pmatrix}, \quad X_3 = \begin{pmatrix} 0 & -1 \\ -1 & 0 \end{pmatrix}$
Inversion	$\mathcal{I} = \begin{pmatrix} -1 & 0 \\ 0 & -1 \end{pmatrix}$

Table 2.3: Explicit matrix representation of $\mathcal{G}$ in the basis of indices (n, m), where (n, m) is defined by Eq. (2.16). The indices can be grouped into sets such that indices within the same set are transformed among themselves under the point group operations.

potential under a point group operation implies that

$$\begin{aligned} V'(\boldsymbol{r}) &= P_{\mathcal{G}} V(\boldsymbol{r}) = V(\mathcal{G}^{-1}\boldsymbol{r}) \\ &= \sum_{n,m=-\infty}^{\infty} \mathrm{e}^{\mathrm{i}(n\boldsymbol{b}_1 + m\boldsymbol{b}_2)\,\cdot\,(\mathcal{G}^{-1}\boldsymbol{r})}\, V_{n,m} \\ &= \sum_{n,m=-\infty}^{\infty} \mathrm{e}^{\mathrm{i}(n\mathcal{G}\boldsymbol{b}_1 + m\mathcal{G}\boldsymbol{b}_2)\,\cdot\,\boldsymbol{r}}\, V_{n,m} \\ &= \sum_{n',m'=-\infty}^{\infty} \mathrm{e}^{\mathrm{i}(n'\boldsymbol{b}_1 + m'\boldsymbol{b}_2)\,\cdot\,\boldsymbol{r}}\, V_{n',m'}. \end{aligned} \tag{2.17}$$

Hence, we can equate two Fourier coefficients $V_{n,m}$ and $V_{n',m'}$ via the relation $n'\boldsymbol{b}_1 + m'\boldsymbol{b}_2 = n\mathcal{G}\boldsymbol{b}_1 + m\mathcal{G}\boldsymbol{b}_2$. The relation can be rewritten into matrix representation using (n, m) as basis,

$$\begin{pmatrix} n' \\ m' \end{pmatrix} = (\text{representation of } \mathcal{G}) \begin{pmatrix} n \\ m \end{pmatrix}, \tag{2.18}$$

and the representation of $\mathcal{G}$ is given in Table 2.3.

For any non-zero $V_{n,m}$, the $V_{n',m'}$s generated through the group operations are necessarily non-zero too. There is an additional constraint that $V(\boldsymbol{r})$ must be real, hence $V^*_{n,m} = V_{-n,-m}$. Together, these conditions enable us to group the $V_{n,m}$s into sets of closely related Fourier coefficients.

Other than the trivial constant solution $V(\boldsymbol{r}) = V_{0,0}$, the simplest case is obtained when all coefficients vanish except for the set associated with $V_{1,0} = V_0$, that is $(n, m) = \{\pm(1, 0), \pm(0, 1), \pm(1, 1)\}$ and by convention, $V_{0,0} = 3V_0$. This yields the honeycomb potential of the discussed optical lattice; see Eq. (3.7).

2.4 Tight-binding model and Dirac fermions

2.4.1 Wannier functions

Consider a collection of potential wells (with a given depth) located at the lattice points of a periodic lattice. When the lattice parameter is infinitely large, we can essentially view the wells as isolated and an atom trapped in a particular well would be in the vibrational levels localized at the lattice sites. If we are to shrink the lattice parameter, at some point, we have to modify the identification of the atomic states in the lattice with the vibrational levels of isolated wells. This modification is necessary when the spatial extent of a vibrational level is comparable to the lattice parameter, which is the typical distance between two neighboring potential wells, since an atom in that vibrational level can now be affected by the presence of neighboring wells [47]. This motivates us to use a *tight-binding model* to describe a system where there is non-negligible overlap between localized vibrational states of neighboring potential wells, but not so much as to completely destroy the isolated

well picture.

The tight-binding model is closely related to the idea of *Wannier functions* [54]. In turn, the relation of Wannier functions to the Bloch functions of Eq. (2.12) can be established by considering a Bloch function as a function of $\boldsymbol{k}$ instead of $\boldsymbol{r}$. Since $\psi_{\boldsymbol{k}}(\boldsymbol{r})$ is periodic in the reciprocal space, i.e. $\psi_{\boldsymbol{k}+\boldsymbol{q}}(\boldsymbol{r}) = \psi_{\boldsymbol{k}}(\boldsymbol{r})\ \forall \boldsymbol{q} \in \tilde{B}$, we can Fourier expand it as

$$\psi_{n\boldsymbol{k}}(\boldsymbol{r}) = \frac{1}{\sqrt{N_c}} \sum_{\boldsymbol{R}\in\mathcal{B}} \mathrm{e}^{\mathrm{i}\boldsymbol{k}\cdot\boldsymbol{R}} \phi_{n,\boldsymbol{r},\boldsymbol{R}}, \tag{2.19}$$

where N_c is the total number of unit cells and n is a band index. We may invert Eq. (2.19) to arrive at

$$\begin{aligned}
\phi_{n,\boldsymbol{r},\boldsymbol{R}} &= \frac{1}{\sqrt{N_c}} \sum_{\boldsymbol{k}\in\Omega} \mathrm{e}^{-\mathrm{i}\boldsymbol{k}\cdot\boldsymbol{R}} \psi_{n\boldsymbol{k}}(\boldsymbol{r}) \\
&= \frac{1}{\sqrt{N_c}} \sum_{\boldsymbol{k}\in\Omega} \mathrm{e}^{\mathrm{i}\boldsymbol{k}\cdot(\boldsymbol{r}-\boldsymbol{R})} u_{n\boldsymbol{k}}(\boldsymbol{r}) \quad \text{from Eq. (2.12)} \\
&= \frac{1}{\sqrt{N_c}} \sum_{\boldsymbol{k}\in\Omega} \mathrm{e}^{\mathrm{i}\boldsymbol{k}\cdot(\boldsymbol{r}-\boldsymbol{R})} u_{n\boldsymbol{k}}(\boldsymbol{r}-\boldsymbol{R}). \quad \text{from Eq. (2.11)}
\end{aligned} \tag{2.20}$$

Clearly, $\phi_{n,\boldsymbol{r},\boldsymbol{R}}$ is a function of $\boldsymbol{r}-\boldsymbol{R}$ and in fact, it is a Wannier function of energy band index n centered at lattice point $\boldsymbol{R}$, i.e. $w_n(\boldsymbol{r}-\boldsymbol{R}) \equiv \langle \boldsymbol{r}|w_{n\boldsymbol{R}}\rangle = \phi_{n,\boldsymbol{r},\boldsymbol{R}}$. There is a subtlety in the definition of a Wannier function, that is we can rewrite it as

$$w_n(\boldsymbol{r}-\boldsymbol{R}) = \frac{1}{\sqrt{N_c}} \sum_{\boldsymbol{k}\in\Omega} \mathrm{e}^{-\mathrm{i}\boldsymbol{k}\cdot\boldsymbol{R}+\mathrm{i}\varphi(\boldsymbol{k})} \psi_{n\boldsymbol{k}}(\boldsymbol{r}), \tag{2.21}$$

where $\varphi(\boldsymbol{k})$ is now an arbitrary real function, because the Bloch function is determined only within an overall phase factor. By manipulating the phase factor, it is possible to find a corresponding set of Wannier functions that decrease exponentially at infinity for each energy band in a 1D infinite lattice with a center of symmetry [55, 56].

So far, we have assumed a Bravais lattice to illustrate the relation between Wannier functions and Bloch functions, such that the energy band has a simple structure with a single energy value attached to each $\boldsymbol{k}$ point. In general, when the energy band has a complex structure such that there are several branches which intersect at some $\boldsymbol{k}$-points (the tight-binding band of a honeycomb lattice is a complex band with two branches intersecting at the Dirac points), it is still possible to attach a Wannier function that falls off exponentially at infinity to each lattice site [57–59]. However, the Wannier function $w_{n,\mathrm{A}}(\boldsymbol{r}-\boldsymbol{R}_{\mathrm{A}})$ of one sublattice site $\boldsymbol{R}_{\mathrm{A}}$ may not be identical with $w_{n,\mathrm{B}}(\boldsymbol{r}-\boldsymbol{R}_{\mathrm{B}})$ defined on a site $\boldsymbol{R}_{\mathrm{B}}$ that belongs to another sublattice, in the sense that $w_{n,\mathrm{A}}(\boldsymbol{r})$ does not necessarily equal to $w_{n,\mathrm{B}}(\boldsymbol{r})$, but are related through space group operation which transforms $\boldsymbol{R}_{\mathrm{A}}$ to $\boldsymbol{R}_{\mathrm{B}}$, e.g. $w_{n,\mathrm{A}}(\boldsymbol{r}) = w_{n,\mathrm{B}}(-\boldsymbol{r})$ due to the inversion symmetry of the potential. In fact, the Wannier functions attached to a lattice site $\boldsymbol{R}_{\mathrm{A}}$ should form a basis of an irreducible representation of a group $G_{\boldsymbol{R}_{\mathrm{A}}}$, which contains all space group operations that leave $\boldsymbol{R}_{\mathrm{A}}$ invariant [57], i.e. the Wannier functions should display symmetry properties associated with the local potential structure.

The Bloch wave function of a honeycomb lattice has now to be written as a linear combination of quasi-Bloch wave functions[6],

$$\psi_{n\boldsymbol{k}}(\boldsymbol{r}) = \alpha_{n\boldsymbol{k}}\psi^{(\mathrm{A})}_{n\boldsymbol{k}}(\boldsymbol{r}) + \beta_{n\boldsymbol{k}}\psi^{(\mathrm{B})}_{n\boldsymbol{k}}(\boldsymbol{r}) \;\text{ with }\; |\alpha_{n\boldsymbol{k}}|^2 + \beta_{n\boldsymbol{k}}|^2 = 1, \tag{2.22}$$

where the quasi-Bloch wave functions are defined analogous to Eq. (2.19) [58],

$$\psi^{(a)}_{n\boldsymbol{k}}(\boldsymbol{r}) = \frac{1}{\sqrt{N_c}}\sum_{\boldsymbol{R}_a} \mathrm{e}^{\mathrm{i}\boldsymbol{k}\cdot\boldsymbol{R}_a} w_{n,a}(\boldsymbol{r}-\boldsymbol{R}_a) \;\text{ with }\; a = \mathrm{A},\mathrm{B} \tag{2.23}$$

and essentially live on the type-A sublattice and type-B sublattice, respectively.

The Wannier functions of Eq. (2.21) has an additional useful property, that is,

[6] This is reminiscent of the linear combinations of atomic orbitals (LCAO) method.

the Wannier functions centered at different lattice sites or of different bands are orthonormal to each other, i.e.

$$\langle w_{n,\boldsymbol{R}}|w_{n',\boldsymbol{R}'}\rangle = \int (d\boldsymbol{r}) w_n^*(\boldsymbol{r}-\boldsymbol{R}) w_{n'}(\boldsymbol{r}-\boldsymbol{R}') = \delta_{\boldsymbol{R}\boldsymbol{R}'}\delta_{nn'}. \tag{2.24}$$

This property is easily proven with the orthonormality of Bloch wave functions. Hence, the orthonormality and exponentially decaying property of Wannier functions invite us to consider them as the localized single-particle states centered at each lattice sites. We can thus describe the system in a hopping picture, where we envision the particle as hopping from site to site with some quantum mechanical tunneling amplitudes due to the overlap of Wannier functions. If we further consider a tight-binding picture, particles are only allowed to hop between nearest neighbors.

2.4.2 Tight-binding model

The eigenenergies $\epsilon_{n\boldsymbol{k}}$ of H are found by the equation

$$H|\psi_{n\boldsymbol{k}}\rangle = \epsilon_{n\boldsymbol{k}}|\psi_{n\boldsymbol{k}}\rangle. \tag{2.25}$$

Substituting Eqs. (2.22), (2.23) and (2.24) into Eq. (2.25) and assuming that particles can only tunnel between nearest-neighbor lattice sites, i.e. $\langle w_{\boldsymbol{R}_i}|H|w_{\boldsymbol{R}_j}\rangle$ is non-vanishing only if $\boldsymbol{R}_i$ and $\boldsymbol{R}_j$ are two nearest neighbors, we get the 2×2 homogeneous linear system

$$\begin{pmatrix} \epsilon_{\mathrm{A}} - \epsilon_{n\boldsymbol{k}} & Z_{\boldsymbol{k}} \\ Z_{\boldsymbol{k}}^* & \epsilon_{\mathrm{B}} - \epsilon_{n\boldsymbol{k}} \end{pmatrix} \begin{pmatrix} \alpha_{\boldsymbol{k}} \\ \beta_{\boldsymbol{k}} \end{pmatrix} = 0, \tag{2.26}$$

where $\epsilon_a = \langle w_{\boldsymbol{R}_a}|H|w_{\boldsymbol{R}_a}\rangle (a = \mathrm{A}, \mathrm{B})$ are the on-site energies and

$$Z_{\boldsymbol{k}} = \sum_{i=1}^{3} t_i \mathrm{e}^{\mathrm{i}\boldsymbol{k}.\boldsymbol{c}_i} \quad \text{with} \quad t_i = \langle w_{\boldsymbol{R}_\mathrm{A}}|H|w_{\boldsymbol{R}_{\mathrm{B}_i}}\rangle. \tag{2.27}$$

Here, $\boldsymbol{R}_{\mathrm{B}_i} = \boldsymbol{R}_\mathrm{A} + \boldsymbol{c}_i$ is a short-hand notation for the three B sites next to the A site. To have a non-trivial solution, the determinant of the 2×2 matrix in Eq. (2.26) has to vanish, hence we obtain the band structure of a tight-binding model on a honeycomb lattice,

$$\epsilon_{\pm,\boldsymbol{k}} = \epsilon_0 \pm \sqrt{\varepsilon^2 + |Z_{\boldsymbol{k}}|^2}, \tag{2.28}$$

where $\epsilon_0 = (\epsilon_\mathrm{A} + \epsilon_\mathrm{B})/2$ is the mean on-site energy and $\varepsilon = |(\epsilon_\mathrm{A} - \epsilon_\mathrm{B})|/2$ is half of the on-site energy difference. As it should be, the tunneling parameters t_i remain unchanged under any energy shift in H due to orthonormality of Wannier functions. Furthermore, such a shift only results in a corresponding shift in ϵ_0 but not the $\boldsymbol{k}$-dependent square-root term in Eq. (2.28). Hence, the physics of the problem is not lost if we redefine the energy scale such that $\epsilon_0 = 0$.

As expected from the fact that the honeycomb lattice consists of two distinct sublattices, we find two bands[7]: a conduction band (+) and a valence band (−). In each band, the number of Bloch states is the same as the number of unit cells N_c. If we have a perfect honeycomb lattice such that the t_is are independent of the hopping direction, i.e. $t_i = -t$ for $i = 1, 2, 3$ and $t > 0$, then $Z_{\boldsymbol{k}}$ vanishes when

$$1 + \mathrm{e}^{\mathrm{i}\boldsymbol{k}\cdot\boldsymbol{a}_1} + \mathrm{e}^{\mathrm{i}\boldsymbol{k}\cdot\boldsymbol{a}_2} = 0, \tag{2.29}$$

which is solved by the corners K and K' of Ω since $\boldsymbol{K}\cdot\boldsymbol{a}_2 = \boldsymbol{K}'\cdot\boldsymbol{a}_1 = 2\pi/3$. We thus see that the conduction and the valence bands are gapped by ε when the

[7] According to previous discussions on Wannier functions, we should call them the two branches of a complex band. However, to conform to common terminology in the literature, from now onwards, we will call them *bands*.

lattice is filled with particles. For spin-$\frac{1}{2}$ fermions, there are a total of $2N_c$ states in each band. When there is exactly one particle per site (a situation known as *half-filling*), all levels in the valence bands are filled at zero temperature and the Fermi energy E_F (the energy of the highest filled level) precisely cuts the energy surface at the K and K' points. In this case, the low-energy excitations of the system can be described by linearizing the band spectrum in the neighborhood of K and K'. Denoting by $\boldsymbol{q} = \boldsymbol{p}/\hbar$ the small displacement from either $\boldsymbol{K}$ or $\boldsymbol{K}'$, the linearization of $Z_{\boldsymbol{k}}$ gives

$$|Z_{\boldsymbol{k}}| \approx \frac{3at}{2}|\boldsymbol{q}| = \hbar v_0 |\boldsymbol{q}| = |\boldsymbol{p}| v_0, \tag{2.30}$$

where the quantity $v_0 = 3at/(2\hbar)$ is called the *Fermi velocity* in the solid state community, even though it has nothing to do with the standard Fermi velocity $\sqrt{2E_F/m}$, which depends on the actual mass of the particle.

The dispersion relation now takes on the very suggestive form

$$\epsilon_{\pm}(\boldsymbol{p}) \approx \pm\sqrt{m_*^2 v_0^4 + p^2 v_0^2} \tag{2.31}$$

that is typical of a relativistic dispersion relation with particle-hole symmetry. The effective mass m_*, defined through $\varepsilon = m_* v_0^2$, appears thus as the rest mass of the excitations and relates to the energy imbalance of the two sublattices. The Fermi velocity v_0 is the analog of the velocity of light in relativity.

To relate to field theory, the one-particle quantum dynamics is more conveniently described using second quantization. With the hopping picture in mind, we introduce a set of fermionic annihilation and creation operators $\{f_{\boldsymbol{i}\sigma}, f^{\dagger}_{\boldsymbol{i}\sigma}\}$, where $\boldsymbol{i}$ and $\boldsymbol{j}$ label the sites while σ stands for the spin index or any other pertinent quantum number of the particle. These creation (annihilation) operators create (annihilate) particles localized to the lattice sites, with their position wave func-

tions described by the correponding Wannier functions. The second quantized Hamilton operator thus reads

$$H = \sum_{\langle \boldsymbol{i},\boldsymbol{j}\rangle,\sigma} t_{ij}\left(f^\dagger_{\boldsymbol{i}\sigma} f_{\boldsymbol{j}\sigma} + f^\dagger_{\boldsymbol{j}\sigma} f_{\boldsymbol{i}\sigma}\right) + \varepsilon \sum_{\boldsymbol{i}\in\boldsymbol{R}_{\mathrm{A}},\boldsymbol{j}\in\boldsymbol{R}_{\mathrm{B}},\sigma}\left(f^\dagger_{\boldsymbol{i}\sigma} f_{\boldsymbol{i}\sigma} - f^\dagger_{\boldsymbol{j}\sigma} f_{\boldsymbol{j}\sigma}\right), \tag{2.32}$$

where $\langle \boldsymbol{i},\boldsymbol{j}\rangle$ means that only nearest neighbors are included in the sum and t_{ij} is a direction-dependent hopping parameter[8]. This model accounts for hopping to neighboring sites through the first term but does not permit a change in the internal quantum number σ during the hop. A possible energy mismatch of ε between the A and B sites are included through the second term.

The Hamilton operator in Eq. (2.32) can be recast into a form reminiscent of Eq. (2.26) by separately Fourier transforming $\{f_{\boldsymbol{i}\sigma}, f^\dagger_{\boldsymbol{i}\sigma}\}$ of each sublattice to give

$$\begin{aligned} f^\dagger_{\mathrm{A}\boldsymbol{k}\sigma} &= \frac{1}{\sqrt{N_c}}\sum_{\boldsymbol{R}_{\mathrm{A}}} \mathrm{e}^{\mathrm{i}\boldsymbol{k}\cdot\boldsymbol{R}_{\mathrm{A}}} f^\dagger_{\boldsymbol{R}_{\mathrm{A}}\sigma},\ f_{\mathrm{A}\boldsymbol{k}\sigma} = \frac{1}{\sqrt{N_c}}\sum_{\boldsymbol{R}_{\mathrm{A}}} \mathrm{e}^{-\mathrm{i}\boldsymbol{k}\cdot\boldsymbol{R}_{\mathrm{A}}} f_{\boldsymbol{R}_{\mathrm{A}}\sigma}, \\ f^\dagger_{\mathrm{B}\boldsymbol{k}\sigma} &= \frac{1}{\sqrt{N_c}}\sum_{\boldsymbol{R}_{\mathrm{B}}} \mathrm{e}^{\mathrm{i}\boldsymbol{k}\cdot\boldsymbol{R}_{\mathrm{B}}} f^\dagger_{\boldsymbol{R}_{\mathrm{B}}\sigma},\ f_{\mathrm{B}\boldsymbol{k}\sigma} = \frac{1}{\sqrt{N_c}}\sum_{\boldsymbol{R}_{\mathrm{B}}} \mathrm{e}^{-\mathrm{i}\boldsymbol{k}\cdot\boldsymbol{R}_{\mathrm{B}}} f_{\boldsymbol{R}_{\mathrm{B}}\sigma}, \end{aligned} \tag{2.33}$$

where $f^\dagger_{\mathrm{A}\boldsymbol{k}\sigma}$ and $f^\dagger_{\mathrm{B}\boldsymbol{k}\sigma}$ might be interpreted as the creation operators for quasi-Bloch functions that live on sublattice A and sublattice B respectively; see Eq. (2.23). The Hamilton operator becomes

$$H = \sum_{\boldsymbol{k}\in\Omega,\sigma} (f^\dagger_{\mathrm{A}\boldsymbol{k}\sigma}, f^\dagger_{\mathrm{B}\boldsymbol{k}\sigma})\mathcal{H}_{\boldsymbol{k}} \begin{pmatrix} f_{\mathrm{A}\boldsymbol{k}\sigma} \\ f_{\mathrm{B}\boldsymbol{k}\sigma} \end{pmatrix}, \quad \mathcal{H}_{\boldsymbol{k}} = \begin{pmatrix} \varepsilon & Z_{\boldsymbol{k}} \\ Z^*_{\boldsymbol{k}} & -\varepsilon \end{pmatrix}, \tag{2.34}$$

where the matrix representation of H is the same as Eq. (2.26) after a shift in the energy scale by ϵ_0.

[8]The hopping parameter can be chosen to be real in the absence of external fields.

2.4.3 Dirac fermions

Let us now consider a perfect honeycomb lattice such that $t_{ij} = -t, t > 0$ for all nearest-neighbor hoppings[9]. To obtain the effective Hamilton operator for Dirac fermions, we consider small $\boldsymbol{q}$ expansion around the two Dirac points K and K'. Let $\boldsymbol{q} = q_x\boldsymbol{e}_x + q_y\boldsymbol{e}_y, a\big|\boldsymbol{q}\big| \ll 1$, then

$$Z_{\boldsymbol{K}+\boldsymbol{q}} \approx -\frac{3at}{2}(\mathrm{i}q_x - q_y) \quad \text{and} \quad Z_{\boldsymbol{K}'+\boldsymbol{q}} \approx -\frac{3at}{2}(\mathrm{i}q_x + q_y) \approx -Z^*_{\boldsymbol{K}+\boldsymbol{q}}. \tag{2.35}$$

The quasi-Bloch wave representation of H is reduced to the simple form

$$\mathcal{H}_{\boldsymbol{k}} = \begin{pmatrix} \varepsilon & Z_{\boldsymbol{k}} \\ Z^*_{\boldsymbol{k}} & -\varepsilon \end{pmatrix} \approx \begin{cases} \varepsilon\sigma_z + \hbar v_0(q_x\sigma_y + q_y\sigma_x), \ \boldsymbol{k} = \boldsymbol{K} + \boldsymbol{q} \\ \varepsilon\sigma_z + \hbar v_0(q_x\sigma_y - q_y\sigma_x), \ \boldsymbol{k} = \boldsymbol{K}' + \boldsymbol{q} \end{cases} \tag{2.36}$$

where σ_x, σ_y and σ_z are the standard Pauli matrices,

$$\sigma_x = \begin{pmatrix} 0 & 1 \\ 1 & 0 \end{pmatrix}, \quad \sigma_y = \begin{pmatrix} 0 & -\mathrm{i} \\ \mathrm{i} & 0 \end{pmatrix}, \quad \sigma_z = \begin{pmatrix} 1 & 0 \\ 0 & -1 \end{pmatrix}. \tag{2.37}$$

If we now define the Dirac matrices for the (2+1)-dimensional Dirac algebra by $\gamma^\mu = (\gamma^0, \gamma^1, \gamma^2) = (\sigma_z, -\mathrm{i}\sigma_x, -\mathrm{i}\sigma_y)$ such that they satisfy the commutation relations

$$\{\gamma^\mu, \gamma^\nu\} = 2g^{\mu\nu}, \ [\gamma^\mu, \gamma^\nu] = -2\mathrm{i}\epsilon^{\mu\nu\lambda}\gamma_\lambda, \ g^{\mu\nu} = (1, -1, -1), \tag{2.38}$$

where $\epsilon^{\mu\nu\lambda}$ is a Levi-Civita symbol, we can rewrite Eq. (2.34) into (keeping only states with wave vector $\boldsymbol{k}$ close to the Dirac points)

$$H_{\mathrm{Dirac}} = v_0 \sum_{\boldsymbol{q}} \overline{\psi}_1(\boldsymbol{q})(\hbar\boldsymbol{\gamma}\cdot\boldsymbol{q} + m_* v_0)\psi_1(\boldsymbol{q}) + \overline{\psi}_2(\boldsymbol{q})(\hbar\boldsymbol{\gamma}\cdot\boldsymbol{q} - m_* v_0)\psi_2(\boldsymbol{q}), \tag{2.39}$$

[9] As we shall see in Sec. 3.4, it is indeed that $t_{ij} < 0$ for nearest neighbor.

where

$$\psi_1(\boldsymbol{q}) = \begin{pmatrix} f_{\mathrm{A}\boldsymbol{K}'+\boldsymbol{q}} \\ f_{\mathrm{B}\boldsymbol{K}'+\boldsymbol{q}} \end{pmatrix}, \quad \psi_2(\boldsymbol{q}) = \sigma_x \begin{pmatrix} f_{\mathrm{A}\boldsymbol{K}+\boldsymbol{q}} \\ f_{\mathrm{B}\boldsymbol{K}+\boldsymbol{q}} \end{pmatrix}, \quad \overline{\psi}_i = \psi_i^\dagger \gamma^0. \tag{2.40}$$

Writing in coordinate space, where $\boldsymbol{q} \to \frac{\mathrm{i}}{\hbar}\nabla$ and we define a four-component Dirac spinor encapsulating the excitations around K and K', $\psi = \begin{pmatrix} \psi_1 \\ \psi_2 \end{pmatrix}$, we arrive at Eq. (2.41), which is an effective Hamilton operator that that resembles the Weyl-Dirac equation in two dimensions,

$$H = v_0 \int \frac{(d\boldsymbol{r})}{(2\pi)^2}\, \overline{\psi}(\boldsymbol{r}) \begin{pmatrix} \mathrm{i}\boldsymbol{\gamma}\cdot\boldsymbol{\nabla} + m_* v_0 & 0 \\ 0 & \mathrm{i}\boldsymbol{\gamma}\cdot\boldsymbol{\nabla} - m_* v_0 \end{pmatrix} \psi(\boldsymbol{r})\,. \tag{2.41}$$

This is why the name *Dirac points* is given to K and K'; see Refs. [3, 10, 60] for more details.

In contrast to the spin components of an electron, which belong to the internal degree of freedom, the spin components of ψ_1 and ψ_2 refer to the sublattices, i.e. "spin-↑" corresponds to sublattice-A while "spin-↓" corresponds to sublattice-B, hence these spins are commonly called *pseudo-spins*[10] in the literature on graphene. Furthermore, since $\boldsymbol{q}$ is the small difference between the Bloch wave-vector $\boldsymbol{k}$ and $\boldsymbol{K}$ or $\boldsymbol{K}'$, a Dirac fermion in a honeycomb lattice thus physically represents a long wavelength modulation of the Bloch function on top of the $\pm 2\pi/3$ phase change (given by $\boldsymbol{K}\cdot\boldsymbol{a}_i$ and $\boldsymbol{K}'\cdot\boldsymbol{a}_i$) from a unit cell to its neighboring cell. Hence, if we are making comparisons between high-energy physics of Dirac fermions and the condensed matter phenomena observed in experiments with fermions on a honeycomb lattice, we have to make careful distinction between these various

[10]This pseudo-spin is to be distinguished from the pseudo-spin encountered in the Hubbard model on bipartite lattice. See Chapter 6.

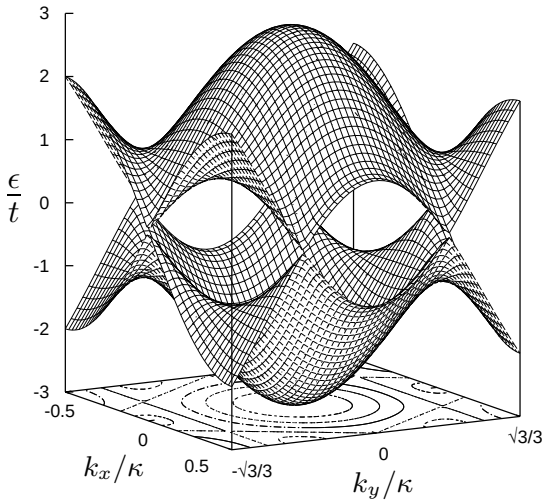

Figure 2.4: The tight-binding band structure of graphene (in units of the tunneling strength t) as a function of $\boldsymbol{k} \in \Omega$ in units of κ. The origin of energy has been chosen at the Dirac points and the axis ranges are $\left|k_x/\kappa\right| \leq 1/2$ and $\left|k_y/\kappa\right| \leq \sqrt{3}/3$. The bottom contour lines are lines of constant $\left|\epsilon\right|/t$.

physical quantities.

2.4.4 Band structure and density of states

When ε vanishes, as is the case of real graphene where all lattice sites have the same energy, then $\epsilon_{\pm,\boldsymbol{k}} = \pm\left|Z_{\boldsymbol{k}}\right|$ and the two bands are degenerate at the corners of Ω where they display circular conical intersections; see Fig. 2.4. In the literature, this situation is referred to as a semi-metal or a zero-gap semi-conductor and the corresponding low-energy excitations are known as massless Dirac fermions. The total band width is $W = 6t$ and, at half-filling, the Fermi energy $E_F = 3t$ (taking the energy origin at the lower band minimum) precisely slices the energy bands at the Dirac points. Hence the Fermi surface reduces to these two points, so that the density of states vanishes there [10]; see Fig. 2.5.

An analytical expression of the density of states is given in Refs. [10, 61, 62] (see Appendix A.3 for detailed derivation). As a function of the reduced energy $\mathcal{E} = \epsilon/t$, the non-interacting density of states per unit cell per spin component

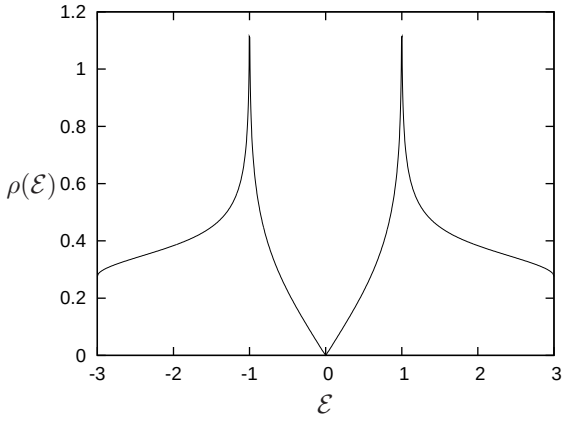

Figure 2.5: The noninteracting density of states per unit cell and per spin component $\rho(\mathcal{E})$ as a function of the reduced energy $\mathcal{E} = \epsilon/t$. The origin of energy has been chosen at the Dirac points. When $\mathcal{E} \ll 1$, then $\rho(\mathcal{E}) \approx 2|\mathcal{E}|/(\sqrt{3}\pi)$ and the density of states vanishes at $\mathcal{E} = 0$, a signature of the semi-metal behavior. Note the logarithmic Van Hove singularity at $|\mathcal{E}| = 1$.

$\rho(\mathcal{E})$ is defined by

$$\rho(\mathcal{E}) = \lim_{N_c \to \infty} \frac{1}{N_c} \sum_{\boldsymbol{k}s} \delta(\epsilon_{s,\boldsymbol{k}}/t - \mathcal{E}) \tag{2.42}$$

with $\boldsymbol{k} = \frac{i}{L}\boldsymbol{b_1} + \frac{j}{L}\boldsymbol{b_2}$ for $i, j = 0, 1, \ldots, L-1$. Its analytical expression is given by

$$\rho(\mathcal{E}) = \frac{2}{\pi^2} \frac{|\mathcal{E}|}{\sqrt{Z_0}} F\left(\frac{\pi}{2}, \sqrt{\frac{Z_1}{Z_0}}\right), \tag{2.43}$$

$$Z_0 = \begin{cases} (1+|\mathcal{E}|)^2 - \frac{1}{4}(|\mathcal{E}|^2 - 1)^2 & \text{for } |\mathcal{E}| \le 1, \\ 4|\mathcal{E}| & \text{for } 1 \le |\mathcal{E}| \le 3, \end{cases}$$

$$Z_1 = \begin{cases} 4|\mathcal{E}| & \text{for } |\mathcal{E}| \le 1, \\ (1+|\mathcal{E}|)^2 - \frac{1}{4}(|\mathcal{E}|^2 - 1)^2 & \text{for } 1 \le |\mathcal{E}| \le 3, \end{cases}$$

where

$$F(\pi/2, k) = \int_0^{\pi/2} \frac{d\theta}{\sqrt{1 - k^2 \sin^2\theta}} = \int_0^1 \frac{dx}{\sqrt{(1-x^2)(1-k^2x^2)}}$$

is a complete elliptical integral of the first kind.

2.5 Summary

The crystallographic properties of an ideal honeycomb lattice have been discussed. We can label a single-particle state by its crystal momentum due to translation invariance. We have shown that the presence of conical intersections at the Dirac points is a consequence of point group symmetry. The possible form of a generic honeycomb potential is obtained based on point group symmetry and we argued that the optical potential proposed in the next chapter is the simplest honeycomb potential in the sense of Fourier expansion. Using the concept of Wannier functions, we provided justification for a tight-binding description of fermions localized at the lattice sites. This paves the way for the use of Hubbard model in Chapter 5 and 6. Based on tight-binding model, we derive the Weyl-Dirac Hamiltonian, which describes the elementary excitations when the lattice is half-filled (each lattice site is occupied by a spin-$\frac{1}{2}$ fermion).

Chapter 3

Ideal honeycomb optical lattice

3.1 Radiative forces and optical lattices

A two-level atom (with angular frequency separation ω_{at} and excited-state angular frequency width Γ) that interacts with a monochromatic laser field with complex amplitude $\boldsymbol{\mathcal{E}}(\boldsymbol{r},t) = \boldsymbol{E}(\boldsymbol{r})\,\mathrm{e}^{-\mathrm{i}\omega_L t}$ gets polarized and experiences radiative forces due to photon absorption and emission cycles [64, 66]. When the light frequency is tuned far away from the atomic resonance, i.e. when the light detuning $\delta = \omega_L - \omega_{at}$ is much larger than Γ, the field-induced saturation effects are negligible and the atom essentially keeps staying in its ground state. In this situation, the atom-field interaction is dominated by stimulated emission processes where the atomic dipole absorbs a photon from one Fourier component of the field and radiates it back into the same or another one of these Fourier modes. In each such stimulated cycle, there is a momentum transfer to the atom and, as a net result, the atom experiences an average force in the course of time. This dipole force exerted by the field onto the atom in its ground state is conservative. It derives from the polarization energy shift of the atomic levels (AC Stark or light shifts; see Fig. 3.1) [65, 67] and the

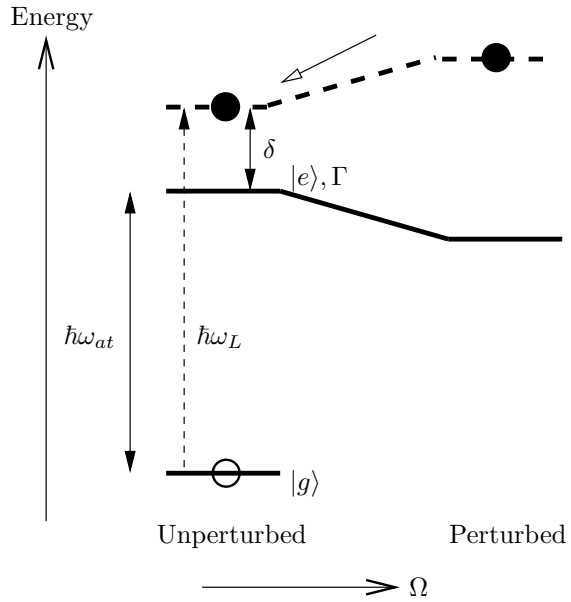

Figure 3.1: Eigenenergies of a two-level atom interacting with an external electric field (blue-detuned, $\delta > 0$). The ground state $|g\rangle$ and the excited state $|e\rangle$ (with spontaneous damping rate Γ) are separated by energy $\hbar\omega_{at}$. The incoming electric field has a frequency ω_L and a corresponding Rabi frequency Ω, which increases with light field intensity. The solid circle represents a "dressed-atom", i.e. a system of atom plus photon [63, 64]. Under perturbation from the external electric field, the atomic levels and the "dressed-atom" have their energies shifted by the a.c. Stark effect [65]. This shift increases with Rabi frequency when the light field is blue-detuned, hence the dipole force (empty-head arrow) will push the "dressed-atom" towards intensity minima.

dipole potential $V(\boldsymbol{r})$ is given by

$$V(\boldsymbol{r}) = \frac{\hbar\Gamma}{8}\,\frac{\Gamma}{\delta}\,\frac{I(\boldsymbol{r})}{I_s} \quad \text{with} \quad \delta \gg \Gamma \quad \text{and} \quad \delta \gg \Omega, \tag{3.1}$$

where $I(\boldsymbol{r}) = \varepsilon_0 c\big|\boldsymbol{E}(\boldsymbol{r})\big|^2/2$ is the light field intensity (time-averaged energy current density) at the center-of-mass position $\boldsymbol{r}$ of the atom and I_s is the saturation intensity of the atom under consideration and Ω is the Rabi frequency,

$$\Omega = \frac{\langle g|\boldsymbol{p}_d \cdot \boldsymbol{E}(\boldsymbol{r})|e\rangle}{\hbar}, \tag{3.2}$$

where $\boldsymbol{p}_d$ is the dipole moment of the atom.

For multi-level atoms, the situation is more complicated as the dipole potential

now depends on the particular atomic ground state sub-level under consideration. However, if the laser detuning δ is much larger than the fine and hyperfine structure splittings of the atomic electronic transition, then all ground state atomic sub-levels will essentially experience the same dipole potential. This common potential turns out to be given by Eq. (3.1) as well. Hence, by conveniently tailoring the space and time dependence of the laser field, one can produce a great variety of dipole potentials and thus manipulate the ground state atomic motion.

Optical lattices are periodic intensity patterns of light obtained through the interference of several monochromatic laser beams [68]. By loading ultracold atoms into such artificial crystals of light one obtains periodic arrays of atoms. Indeed, as seen from Eq. (3.1), when the light field is blue-detuned from the atomic resonance ($\delta > 0$), the atoms can be trapped in the field-intensity minima whereas for red-tuned light ($\delta < 0$) they can be trapped at the field intensity maxima. Such arrays of ultracold atoms trapped in optical lattices have been used in a wide variety of experiments. As recently demonstrated by the observation of the Mott-Hubbard transition with degenerate gases [69], they have proven to be a unique tool to mimic, test and go beyond phenomena observed until now in the condensed-matter realm [70, 71]. They also have a promising potential for the implementation of quantum simulators and for quantum information processing purposes [72–74].

3.2 Possible laser configurations of a perfect lattice

As is discussed in Sec. 2.3.1, the simplest honeycomb potential could be decomposed into six Fourier components (besides the trivial constant solution) with equal coefficients. To create this simplest possible optical lattice with honeycomb structure, we can superpose three coplanar traveling coherent plane waves that have

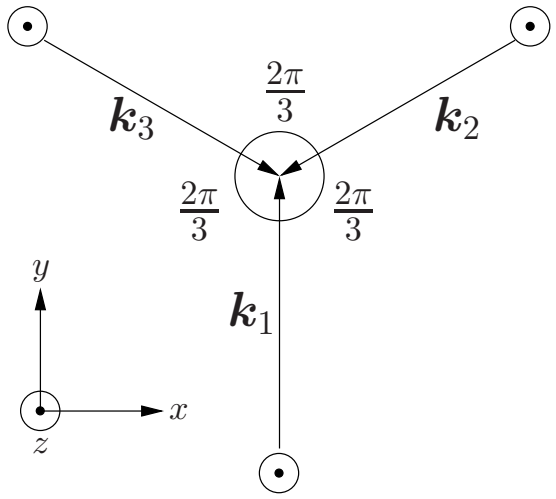

Figure 3.2: The coplanar three-beam configuration used to generate the honeycomb lattice. All beams have the same frequency, strength and linear polarization orthogonal to their common propagation plane. The honeycomb lattice under consideration is obtained for blue-detuned beams with respective angles $2\pi/3$. For these symmetric laser beams, the time-averaged radiation pressure — albeit small at large detuning — vanishes in this configuration. By reversing the propagation direction of one of the lasers, such that $\boldsymbol{k}_1 = \boldsymbol{k}_2 + \boldsymbol{k}_3$, say, a triangular lattice of a different geometry is formed. We will, however, exclusively deal with the $\boldsymbol{k}_1 + \boldsymbol{k}_2 + \boldsymbol{k}_3 = 0$ case.

the same angular frequency $\omega_L = ck_L$, the same field strength $E_0 > 0$, the same polarization and the three wave vectors $\boldsymbol{k}_a$ form a trine: their sum vanishes and the angle between any two of them is $2\pi/3$,

$$\boldsymbol{k}_1 + \boldsymbol{k}_2 + \boldsymbol{k}_3 = 0\,, \quad \boldsymbol{k}_a \cdot \boldsymbol{k}_b = k_L^2\Big(\frac{3}{2}\delta_{ab} - \frac{1}{2}\Big) \tag{3.3}$$

with $a, b = 1, 2, 3$ [68]. As is illustrated in Fig. 3.2, we choose the xy-plane as the common plane of propagation and, to be specific, use

$$\boldsymbol{k}_1 = k_L \boldsymbol{e}_y\,, \qquad \left.\begin{matrix} \boldsymbol{k}_2 \\ \boldsymbol{k}_3 \end{matrix}\right\} = k_L \frac{\mp\sqrt{3}\boldsymbol{e}_x - \boldsymbol{e}_y}{2} \tag{3.4}$$

for the parameterization of the wave vectors.

Further, we take all fields to be linearly polarized orthogonal to the plane, so

that the three complex field amplitudes are given by

$$\boldsymbol{\mathcal{E}}_a(\boldsymbol{r},t) = E_0\, \mathrm{e}^{\mathrm{i}(\boldsymbol{k}_a\cdot\boldsymbol{r}\,-\,\phi_a)}\mathrm{e}^{-\mathrm{i}\omega_L t}\,\boldsymbol{e}_z \tag{3.5}$$

where ϕ_a is the phase of the ath field for time $t = 0$ at $\boldsymbol{r} = 0$[1]. We note that a joint shift of the reference points in time and space,

$$t \to t - \frac{1}{3\omega_L}\sum_a \phi_a\,, \quad \boldsymbol{r} \to \boldsymbol{r} + \frac{2}{3k_L^2}\sum_a \phi_a \boldsymbol{k}_a\,, \tag{3.6}$$

removes the phases ϕ_a from Eq. (3.5), so that the simple choice $\phi_1 = \phi_2 = \phi_3 = 0$ is permissible, and we adopt this convention. In an experimental implementation, one would need to stabilize the phase differences $\phi_a - \phi_b$ to prevent a rapid jitter of the lattice that could perturb the atoms trapped in the potential minima.

The dipole potential (3.1) generated by the electric field $\boldsymbol{E} = \sum_a \boldsymbol{\mathcal{E}}_a$ is of the form

$$V(\boldsymbol{r}) = V_0\big|f(\boldsymbol{r})\big|^2 = V_0 v(\boldsymbol{r}) \quad \text{with } V_0 = \frac{\hbar\Gamma}{8}\frac{\Gamma}{\delta}\frac{I_0}{I_s}\,, \tag{3.7}$$

where I_0 is the intensity associated with the field strength E_0. The total dimensionless field amplitude $f(\boldsymbol{r})$ and the dimensionless optical potential $v(\boldsymbol{r})$ are given by

$$f(\boldsymbol{r}) = 1 + \exp(-\mathrm{i}\boldsymbol{b}_1\cdot\boldsymbol{r}) + \exp(\mathrm{i}\boldsymbol{b}_2\cdot\boldsymbol{r}) \tag{3.8}$$

and

$$v(\boldsymbol{r}) = 3 + 2\cos(\boldsymbol{b}_1\cdot\boldsymbol{r}) + 2\cos(\boldsymbol{b}_2\cdot\boldsymbol{r}) + 2\cos\left((\boldsymbol{b}_1+\boldsymbol{b}_2)\cdot\boldsymbol{r}\right)\,, \tag{3.9}$$

where the reciprocal primitive vectors are $\boldsymbol{b}_1 = \boldsymbol{k}_3 - \boldsymbol{k}_1$ and $\boldsymbol{b}_2 = \boldsymbol{k}_1 - \boldsymbol{k}_2$. In terms of the laser wave vector k_L or the laser wavelength $\lambda_L = 2\pi/k_L$, we express the

[1] We have used the same symbol t for real time and tunneling amplitude. However, it is clear from the context the meaning of t and there should not be any confusion.

various important parameters of a honeycomb lattice as

$$\begin{aligned} \text{(magnitude of primitive lattice vector)} \quad \Lambda &= \left|\boldsymbol{a}_a\right| = \frac{4\pi}{3k_L} = \frac{2\lambda_L}{3}, \\ \text{(magnitude of reciprocal lattice vector)} \quad \kappa &= \left|\boldsymbol{b}_a\right| = \sqrt{3}k_L, \\ \text{(lattice parameter)} \quad a &= \left|\boldsymbol{c}_a\right| = \frac{\Lambda}{\sqrt{3}} = \frac{4\pi}{3\kappa} = \frac{2\lambda_L}{27}. \end{aligned} \tag{3.10}$$

Contour plot of the dipole potential (3.7) generated by blue detuned lasers is shown in Fig. 3.3. We mention in passing that red detuned ($\delta < 0$) lasers give $V_0 < 0$ and there is only one potential minimum in each primitive cell Σ. Upon trapping atoms in these potential minima, one gets a triangular lattice that is not of graphene type. This situation is interesting in view of quantum magnetism and frustration phenomena [71] but it is irrelevant to the system studied in this work.

When the optical lattice is instead blue-detuned ($\delta > 0$), V_0 is positive and atoms are "weak-field seekers". The potential minima coincide with the minima of the electric field strength, and the maxima coincide as well. By an appropriate choice of the coordinate system, the maxima locate at the Bravais sites and the dimensionless potential (3.9) has its maximal value of $v(\mathbf{0}) = 9$ at the corners O, P, Q, R of the diamond-shaped primitive cell Σ; see Fig. 2.1 and Fig. 3.3.

Two different potential minima, given by the zeros of the total dimensionless field amplitude $f(\boldsymbol{r})$, are found in Σ at

$$\boldsymbol{r}_{\text{A}} = \tfrac{1}{3}(\boldsymbol{a}_1 + \boldsymbol{a}_2) = \frac{\Lambda}{\sqrt{3}}\boldsymbol{e}_x \quad \text{and} \quad \boldsymbol{r}_{\text{B}} = 2\boldsymbol{r}_{\text{A}}\,, \tag{3.11}$$

respectively. The minima are organized in a honeycomb structure reminiscent of the positions of the carbon atoms in graphene sheets, hence there are two different sublattices of potential minima, one made up of A sites and the other made up of B sites. Halfway between two neighboring minima, the potential has saddle points where $v(\boldsymbol{r}) = 1$. They are located at the center and at the middle of the edges of Σ;

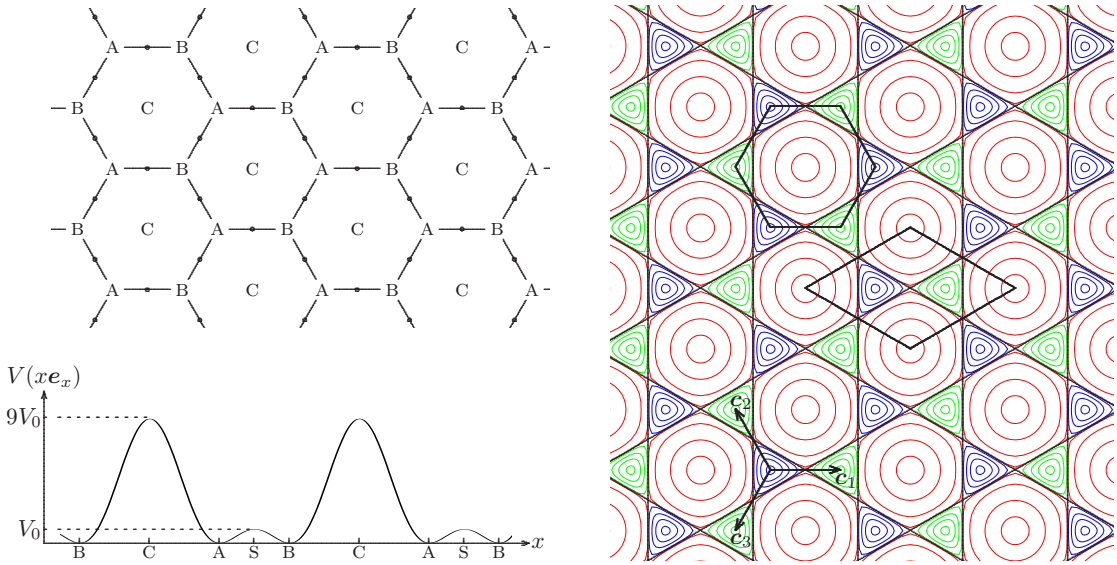

Figure 3.3: **Left:** The honeycomb pattern composed of the triangular lattices of minima at sites A and B, of maxima at sites C, as well as of the saddle points between neighboring A and B sites (marked by dots). The bottom plot shows the potential along the x axis which is one of the ...ABCABC... lines with $x = 0$ at a C site. The saddle points S appear as local maxima here, with a height that is one ninth of the global maxima at sites C. Cold atoms trapped in this optical potential would be found at the A and B sites. **Right:** Equipotential lines for the optical honeycomb potential (3.7). Along the straight black lines that connect the saddle points, we have $V(\boldsymbol{r}) = V_0$. The (red) closed circular curves filling out a hexagonal area are centered at the points of maximal potential; from inside out the respective values are $V(\boldsymbol{r}) = 8V_0$, $5V_0$, $2V_0$, and $1.05V_0$. The closed curves filling out areas of the shape of equilateral triangles are centered at the minima that constitute the A sublattice (blue) or the B sublattice (green); along the curves the potential has the values $V(\boldsymbol{r}) = 0.95V_0$, $0.6V_0$, $0.3V_0$, and $0.05V_0$. One primitive diamond-shaped unit tile Σ spanned by $\boldsymbol{a}_1$ and $\boldsymbol{a}_2$ is traced out. It contains two different minima, one of A-type (in blue, on the left inside) and one of B-type (in green, on the right inside). The trine of the A $\to$ B displacement vectors (2.3) is indicated as well. Finally, for completeness, we also trace out the Bravais Wigner-Seitz unit tile. It is a hexagon centered at a potential maximum and with potential minima at its corners.

see Fig. 3.3. As the saddle points on opposite sides of Σ are connected by Bravais displacements, there are therefore three nonequivalent triangular sublattices of saddle points, and we thus count three saddle points per primitive cell. In the vicinity of the minima, the potential is isotropic such that the local potential may be approximated by an isotropic harmonic oscillator potential. In contrast, the local potential at the saddle point is anisotropic.

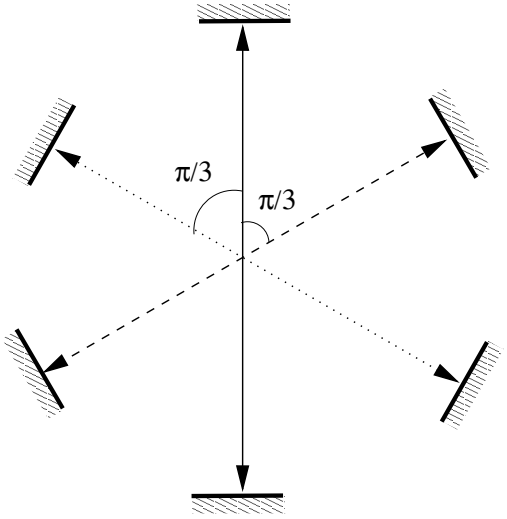

Figure 3.4: Schematic diagram of producing a honeycomb optical lattice by superposing three independent standing waves, which are created using counter-propagating laser beams. Frequency beating and polarization selection can be used so that the interference between the standing waves are time-averaged to zero.

All the matters discussed above are clearly illustrated in Fig. 3.3, where we clearly identify the various triangular sublattices. Cold fermionic atoms trapped in this optical potential would be found at the A and B sites, similar to the binding of electrons in graphene to the carbon atoms.

Before closing this section, we would like to remark that there are many possible laser configurations to create a honeycomb optical potential besides the one proposed in Fig. 3.2. Three other possible configurations include: (1) reversing the propagation direction of one of the lasers in Fig. 3.2 such that $\boldsymbol{k}_1 = \boldsymbol{k}_2 + \boldsymbol{k}_3$, (2) superposing three *independent* standing waves (created by counter-propagating laser beams), of the same wavelength and with equal intensity, whose wave vectors form the trine of Fig. 3.2; see Fig. 3.4, and (3) passing a strong laser beam through a hologram to generate the desired trapping patterns, a method known as holographic optical tweezers (HOTs) [75–78]; see Fig. 3.5. All alternatives will result in the dimensionless optical potential (3.9) but with a redefinition of the reciprocal primitive vectors $\boldsymbol{b}_i$. Other configurations that involve more laser beams may not be feasible in practice due to space limitations.

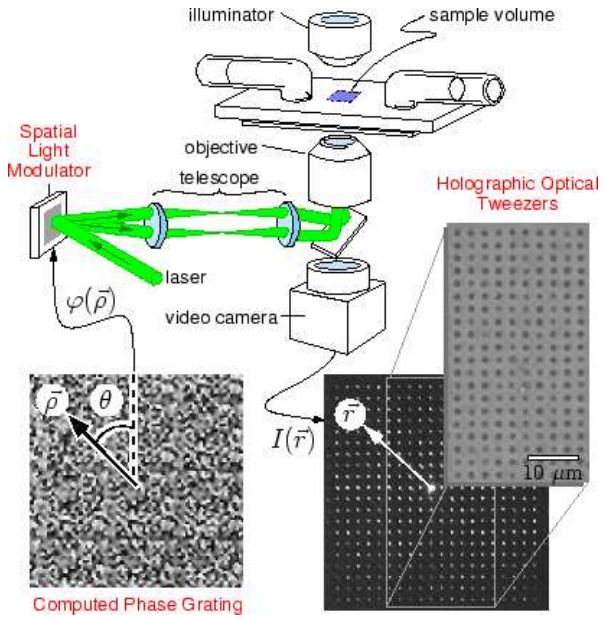

Figure 3.5: Schematic diagram of the holographic optical tweezers method. A single collimated laser beam is split into several beams by a computer-generated diffraction grating (the spatial light modulator). The diffracted beams then pass through the objective lens and create an optical trap at the focal plane of the objective lens. Reprinted from Ref. [76], Copyright(2002), with permission from Elsevier.

In the second alternative, we can choose the linear polarization of a standing wave to be in-plane and the other two waves to have their linear polarizations perpendicular to the plane. Acoustic-optical modulator can then be used to introduce a frequency difference[2] between the three pairs of standing waves. Due to the frequency differences, the (residual) interference between any two standing waves is time-averaged to zero [69]. The orthogonal polarizations will further minimize the interference on top of the frequency beating. Similar to the configuration proposed in Fig. 3.2, we need to stabilize the phase difference to prevent a rapid jitter of the lattice.

Finally, in the HOT method, a single laser beam is used and, usually, it does not require a complex hologram. Several algorithms have been proposed to generate the hologram that most accurately produces the desired pattern, among which the fastest algorithm is to compute the position-dependent phase associated with

[2]In Ref. [69], a frequency difference of 30 MHz was reported.

a linear combination of the desired beams and to simply discard the associated amplitude variations [79]. However, the resulting trapping pattern tends to contain many ghost traps at symmtery-dictated positions and there are large variations in the trap intensities from their designed values [78]. A probably more versatile variant of it called *generalized phase gradient* method was proposed by Palima *et al.*, in which the phase mask is simply patterned after the desired intensity pattern [80].

3.3 Optical lattice and graphene

In graphene sheets, the electrostatic potential that governs the dynamics of electrons, the sum of the Coulomb potentials of the carbon ions, exhibits the symmetries associated to a honeycomb pattern. Microscopically, the optical dipole potential of Eqs. (3.7) and (3.9) differs markedly from the graphene potential. In particular, the very strong forces that the electrons in graphene experience close to the ions have no counterpart in the optical lattice, and the interaction between the atoms loaded into the optical potential is quite different from the electric repulsion between electrons. Nevertheless, the common symmetry group implies great similarities between the band structures of the two potentials. In the respective parameter regimes, when the spatial overlap between neighboring atomic orbitals or between vibrational states of neighboring optical potential wells is small, the tight-binding approximation is valid and the effective Hamilton operators are virtually identical, i.e. Eq. (2.32). In particular, experiments made with atoms offers new knobs to play with and, with due attention to the difference between the two physical systems, these observations may deepen our understanding about phenomena observed with graphene samples.

3.4 Tunneling parameter in a perfect honeycomb lattice

In an ideal honeycomb lattice, the effective tight-binding model (2.32) is characterized by a single parameter t, which is simply the tunneling parameter between neighboring lattice sites. Since the optical potential (3.7) is regular, we can attempt to calculate t analytically using Eq. (2.27) under certain approximations, or to extract the value of t from a numerically calculated band structure using Eq. (2.30). The calculated t is expressed in terms of experimentally-controlled parameters, thus provides a useful guide to experimentalists. Both methods for obtaining t will be illustrated in the following subsections.

3.4.1 Gaussian approximation of Wannier function

By analogy with the LCAO method, we rely on the harmonic approximation of the potential wells around sites A and B, that is to approximate the lowest energy band Wannier functions $w_{0,\mathrm{A}}$ and $w_{0,\mathrm{B}}$ by the corresponding harmonic ground state wave functions. The small perturbation is given by the difference between the exact full Hamilton operator and the Hamilton operator of a local harmonic oscillator. Equation (2.27) has to be modified accordingly by writing the actual Wannier state as (we omit the band index as we will always be dealing with the ground energy band)

$$|\boldsymbol{R}_a\rangle = \sum_{n=0}^{\infty} |\boldsymbol{R}_a^{(n)}\rangle \approx |\boldsymbol{R}_a^{(0)}\rangle + |\boldsymbol{R}_a^{(1)}\rangle, \quad a = \mathrm{A}, \mathrm{B} \tag{3.12}$$

where the superscript denotes the order of approximation and $\left|\boldsymbol{R}_a^{(0)}\right\rangle$ is the normalized local harmonic oscillator ground state. To enforce the orthonormality of

Wannier states (2.24), we have, to first order approximation,

$$\langle \boldsymbol{R}_{\rm A}^{(0)}|\boldsymbol{R}_{\rm B}^{(0)}\rangle \approx -\langle \boldsymbol{R}_{\rm A}^{(1)}|\boldsymbol{R}_{\rm B}^{(0)}\rangle - \langle \boldsymbol{R}_{\rm A}^{(0)}|\boldsymbol{R}_{\rm B}^{(1)}\rangle. \tag{3.13}$$

Next, we employ the completeness of energy states $|n_{\rm LHO}\rangle$ of local harmonic oscillator (LHO), i.e. $\mathbb{1} = \sum_n |n_{\rm LHO}\rangle\langle n_{\rm LHO}|$, to express $\langle \boldsymbol{R}_{\rm A}^{(0)}|H|\boldsymbol{R}_{\rm B}^{(1)}\rangle$ in terms of harmonic oscillator ground state. Since the trapped atoms only populate the lowest vibrational levels when the potential wells are sufficiently deep, the Hamilton operator has negligible off-diagonal elements that connect LHO ground state to LHO excited states. Hence,

$$\begin{aligned}
\langle \boldsymbol{R}_{\rm A}^{(0)}|H|\boldsymbol{R}_{\rm B}^{(1)}\rangle &= \sum_n \langle \boldsymbol{R}_{\rm A}^{(0)}|H|n_{LHO}^{\rm (A)}\rangle\langle n_{LHO}^{\rm (A)}|\boldsymbol{R}_{\rm B}^{(1)}\rangle \approx \langle \boldsymbol{R}_{\rm A}^{(0)}|H|\boldsymbol{R}_{\rm A}^{(0)}\rangle\langle \boldsymbol{R}_{\rm A}^{(0)}|\boldsymbol{R}_{\rm B}^{(1)}\rangle, \\
\langle \boldsymbol{R}_{\rm A}^{(1)}|H|\boldsymbol{R}_{\rm B}^{(0)}\rangle &\approx \langle \boldsymbol{R}_{\rm A}^{(1)}|\boldsymbol{R}_{\rm B}^{(0)}\rangle\langle \boldsymbol{R}_{\rm B}^{(0)}|H|\boldsymbol{R}_{\rm B}^{(0)}\rangle.
\end{aligned} \tag{3.14}$$

Substituting Eqs. (3.12), (3.13) and (3.14) into Eq. (2.27), we arrive at

$$\begin{aligned}
\epsilon_0 &\approx E_0, \\
t &\approx -\langle \boldsymbol{R}_{\rm A}^{(0)}|(H-E_0)|\boldsymbol{R}_{\rm B}^{(0)}\rangle,
\end{aligned} \tag{3.15}$$

where $E_0 = \langle \boldsymbol{R}_{\rm A}^{(0)}|H|\boldsymbol{R}_{\rm A}^{(0)}\rangle = \langle \boldsymbol{R}_{\rm B}^{(0)}|H|\boldsymbol{R}_{\rm B}^{(0)}\rangle$. This is identical to the expression (32) in [52]. A simple check on expression (3.15) shows that the approximated t is invariant under arbitrary energy shift in the Hamilton operator, i.e. $H \to H + \text{constant}$.

From the optical potential (3.7), we find

$$V(\boldsymbol{r}_a + \boldsymbol{r}) \approx \frac{3}{4}V_0\kappa^2\boldsymbol{r}^2 = \frac{m\omega_0^2}{2}\boldsymbol{r}^2 \quad \text{for } a = {\rm A}, {\rm B} \quad \text{with} \quad \hbar\omega_0 = 3\sqrt{V_0 E_R}\,, \tag{3.16}$$

where $E_R = \hbar^2 k_L^2/(2m)$ is the recoil energy of the atom. In terms of $\ell = \sqrt{\hbar/(m\omega_0)}$,

the familiar length unit of the harmonic oscillator, the ground state wave function is

$$w_{\mathrm{A}}^{(0)}(\boldsymbol{r}) = w_{\mathrm{B}}^{(0)}(\boldsymbol{r}) \approx \frac{1}{\sqrt{\pi}\ell}\,\mathrm{e}^{-\frac{1}{2}\boldsymbol{r}^2/\ell^2}\,. \tag{3.17}$$

From this we get $E_{\mathrm{A}} = E_{\mathrm{B}} = E_0 \approx \hbar\omega_0$ and the overlap integrals are simply

$$\langle \boldsymbol{R}_{\mathrm{A}}^{(0)} | \boldsymbol{R}_{\mathrm{B}}^{(0)} \rangle = \exp\left(-\frac{2\pi^2}{9}\sqrt{\frac{V_0}{E_R}} \right). \tag{3.18}$$

Keeping in mind that $V_0 \gg E_0 \gg E_R$ in the tight-binding regime, $\langle \boldsymbol{R}_{\mathrm{A}}^{(0)} | \boldsymbol{R}_{\mathrm{B}}^{(0)} \rangle \ll 1$ and we find from Eq. (3.15)

$$t \approx \left(\frac{\pi^2}{3} - 1 \right) V_0 \, \exp\left(-\frac{2\pi^2}{9}\sqrt{\frac{V_0}{E_R}} \right), \tag{3.19}$$

to leading order. However, since the hopping amplitude is given by the overlap integral of the localized wave functions w_{A} and w_{B} of two neighboring sites, we see that the value of t crucially depends on the tails of these wave functions. Wannier functions often decay exponentially [57, 58] and, therefore, they cannot be realistically approximated by Gaussian wave functions. Hence Eq. (3.19) can, at best, serve as a rough underestimate [81]. In the next section we will derive a reliable and accurate estimate of the tunneling amplitudes in the tight-binding regime by use of the instanton method.

3.4.2 Semi-classical approach

Using k_L^{-1}, $\sqrt{V_0/m}$, V_0, and $\sqrt{m/(k_L^2 V_0)}$ as length, velocity, energy, and time units, respectively, the Schrödinger equation can be conveniently recast into a dimensionless form that features an effective Planck's constant $\hbar_e$ (we keep the same symbols for the rescaled variables for simplicity and t in the equation refers

to time),

$$\mathrm{i}\hbar_e\partial_t\psi = -\frac{\hbar_e^2}{2}\boldsymbol{\nabla}^2\psi + v(\boldsymbol{r})\psi\,, \quad \hbar_e = \sqrt{\frac{2E_R}{V_0}}\,, \tag{3.20}$$

with $v(\boldsymbol{r})$ given by Eq. (3.9), here expressed in rescaled units. In the tight-binding approximation it is assumed that $V_0 \gg E_R$, and thus $\hbar_e \ll 1$. In this situation, semiclassical methods, which relies on the asymptotic expansion in ascending powers of $\hbar_e$, provide very efficient and very accurate ways for evaluating dynamical and spectral quantities of interest. They generally amount to evaluating integrals with the aid of semiclassical expressions for the quantum propagator, derived from its Feynman-path integral formulation through stationary-phase approximations around the classical trajectories [82].

For example, it is well-known that the energy splitting between the two lowest energy levels of an atom moving in a one-dimensional symmetric double well can be accurately calculated using the WKB method [82]. This WKB method can be extended to several dimensions and in the sequel we will derive a semiclassical estimate of t for the honeycomb lattice using the method proposed by Mil'nikov and Nakamura [83]. It amounts to evaluating t using the classical complex trajectory (in rescaled units) that connects A and B through the classically forbidden region — the so-called instanton trajectory.

Using $\hbar\omega_0$ as an order of magnitude for the vibrational level inside a potential well, we see that in the rescaled units, this energy is $\hbar\omega_0/V_0 = 3\hbar_e/\sqrt{2} \ll 1$. So we can simply look for the instanton trajectory at zero energy. In rescaled units, the hopping amplitude is then expressed as

$$\frac{t}{V_0} = \alpha\sqrt{\hbar_e}\mathrm{e}^{-S_0/\hbar_e}\,, \tag{3.21}$$

where S_0 is the (rescaled) classical action along the zero-energy instanton trajectory, and the numerical factor α is obtained from integrating out the fluctuations

around the zero-energy instanton trajectory (see below).

As the zero-energy instanton fully runs in the classically forbidden region, the variables take on complex values. For our particular case, the good parameterization turns out to keep $\boldsymbol{r}$ real while taking the time $t = \mathrm{i}\tau$ and $\boldsymbol{p} = -\mathrm{i}\tilde{\boldsymbol{p}}$ purely imaginary with τ and $\tilde{\boldsymbol{p}}$ real. Hamilton's classical equations of motion in the new variables are just obtained from the original ones by flipping $v(\boldsymbol{r})$ to $-v(\boldsymbol{r})$. The symmetry of the potential dictates that the zero-energy instanton trajectory is simply the straight line connecting site A to B (see Fig. 3.3), hence

$$\frac{1}{2}\left(\frac{dx}{d\tau}\right)^2 - v(x\boldsymbol{e}_x) = \text{energy} = 0 \tag{3.22}$$

with the instanton trajectory given by $\boldsymbol{r}_0 = x\boldsymbol{e}_x$. In the following we calculate the instanton between A and A+$\boldsymbol{c}_1$. We first re-express the instanton trajectory in the rescaled form $\boldsymbol{r}_0(\tau) = k_L a x_0(\tau)\boldsymbol{e}_x$ such that it is now measured in units of the inter-well distance a, followed by a shift of origin to the saddle point between two potential wells, i.e. $x' = x_0 - 3/2$, then the equation of motions (3.22) becomes

$$\frac{4\pi}{3\sqrt{3}}\left(\frac{dx'}{d\tau}\right) = \sqrt{2}\left(2\cos\left(\frac{2\pi}{3}x'\right) - 1\right). \tag{3.23}$$

Upon integration, it yields the instanton solution

$$\tan[\pi x_0(\tau)/3] = -\sqrt{3}\,\coth[3\sqrt{2}\tau/4]\,. \tag{3.24}$$

The boundary conditions are $x_0 = 1$, $\dot{x}_0 = 0$ when $\tau \to -\infty$ and $x_0 = 2$, $\dot{x}_0 = 0$ when $\tau \to \infty$, meaning that the instanton starts at A with zero velocity and ends at B with zero velocity, the whole process requiring an infinite amount of time. This is indeed what is expected as both endpoints of the instanton are unstable in the reversed potential picture. Since the energy associated with this instanton

trajectory is zero, the classical action is simply

$$S_0 = \int_{k_L a}^{2k_L a} dx\ \sqrt{2v(\boldsymbol{r})}|_{y=0} = \sqrt{2}\int_{k_L a}^{2k_L a} dx\ \big|f(x, y=0)\big|$$
$$= -\sqrt{2}\int_{k_L a}^{2k_L a} dx\ \left(1 + 2\cos\frac{\sqrt{3}}{2}x\right) = 4\sqrt{2}\left(1 - \frac{\pi}{3\sqrt{3}}\right) \approx 2.237\,, \quad (3.25)$$

where $f(x, y)$ is given by (3.8).

The computation of α proves technically more demanding. Following Ref. [83], it is given by the product $\alpha_1\alpha_2$ with

$$\alpha_1 = \sqrt{\frac{S_0}{2\pi}}\sqrt{\frac{\det[-\partial_\tau^2 + \omega_0^2]}{\det'[-\partial_\tau^2 + \omega_x^2(\tau)]}}\,,$$
$$\alpha_2 = \sqrt{\frac{\det[-\partial_\tau^2 + \omega_0^2]}{\det[-\partial_\tau^2 + \omega_y^2(\tau)]}}\,. \quad (3.26)$$

Here $\omega_a^2(\tau) = (\partial_a^2 v)(\boldsymbol{r}_0)$ $(a = x, y)$ is the second derivative of the rescaled potential along the zero-energy instanton trajectory $\boldsymbol{r}_0(\tau)$ while ω_0 is the frequency of the rescaled harmonic potential approximation around A; see Eq. (3.16). In rescaled units, we have $\omega_0 = 3/\sqrt{2}$. The prime in the formula for α_1 means that the determinant is calculated by excluding the eigenspace of the operator $-\partial_\tau^2 + \omega_x^2$ with the smallest eigenvalue.

The determinants of the differential operators involved in the computation of α stem from the linear stability analysis of the dynamical flow in the neighborhood of the zero-energy instanton trajectory as encapsulated in the monodromy matrix. They can be straightforwardly computed from solutions of the linear Jacobi-Hill equations of degree 2 associated with these differential operators [84]. For example, α_2 is solved as

$$\alpha_2 = \lim_{T\to\infty}\sqrt{\frac{J_0(T)}{J(T)}} \quad (3.27)$$

where the Jacobi fields $J(\tau)$ and $J_0(\tau)$ satisfy the differential equations

$$\frac{d^2J(\tau)}{d\tau^2} - \omega_y^2(\tau)J(\tau) = 0\,, \tag{3.28a}$$

$$\frac{d^2J_0(\tau)}{d\tau^2} - \omega_0^2 J_0(\tau) = 0\,, \tag{3.28b}$$

with initial conditions

$$\begin{aligned} J_0(-T) &= J(-T) = 0\,, \\ \dot{J}_0(-T) &= \dot{J}(-T) = 1\,. \end{aligned} \tag{3.29}$$

The interested reader is referred to [83, 84] for details. We simply give here some of the important steps to arrive at the final result for the honeycomb lattice. α_1 is contributed by the Gaussian fluctuations around the instanton with the spatial coordinate lying on the classical path (the straight line connecting two neighboring lattice sites), hence it is computed similar to a 1D problem. It can be simplified into the form (see Eq. (18) of Ref. [83])

$$\alpha_1 = P\sqrt{\frac{\omega_0}{\pi}}, \tag{3.30}$$

where P is a constant determined by the asymptotic form of the solution to the Jacobi equation

$$\frac{d^2J(\tau)}{d\tau^2} - \omega_x^2(\tau)J(\tau) = 0. \tag{3.31}$$

It is easily verified that the time derivative of the instanton $\eta(\tau) \equiv \dot{x}_0(\tau)$ is a solution to the Jacobi equation (3.28b) such that

$$\eta(\tau) = \frac{3\sqrt{6}}{4\pi}\frac{1-\tanh^2(3\sqrt{2}\tau/4)}{1+\frac{1}{3}\tanh^2(3\sqrt{2}\tau/4)} \xrightarrow{\tau\to\pm\infty} \frac{P}{4\pi/(3\sqrt{3})}\exp(-\omega_0|\tau|) \tag{3.32}$$

and $P = 3\sqrt{2}$. With $\omega_0 = 3/\sqrt{2}$, we obtain $\alpha_1 = \sqrt{\frac{27\sqrt{2}}{\pi}} \approx 3.486$.

In contrast, the pre-factor α_2 is contributed by the Gaussian fluctuations with transverse coordinates (with respect to the classical path). Solving Eq. (3.28b) yields $J_0(\tau) = \frac{\sinh(\omega_0(\tau+T))}{\omega_0}$ such that $J_0(T) \approx \frac{1}{2\omega_0}\exp(2\omega_0 T)$ for large T. To solve Eq. (3.28a), $J(T)$ is re-expressed in terms of $\eta(\tau)$, which is another solution of Eq. (3.28a) with the initial conditions

$$\eta(-T) = 1,\ \dot{\eta}(-T) = \omega_0 \tag{3.33}$$

such that

$$J(\tau) = \eta(-T)\eta(\tau)\int_{-T}^{\tau} \eta^{-2}(\tau')d\tau'. \tag{3.34}$$

At $\tau = T$, we thus have

$$J(T) = \eta(T)\int_{-T}^{T} \eta^{-2}(\tau')d\tau'. \tag{3.35}$$

For large negative τ, we can neglect the difference between $\omega_y(\tau)$ and ω_0,

$$\omega_y(\tau) = -9\cos\left(\frac{2\pi}{3}x_0(\tau)\right)\Big|_{x_0(\tau)\approx 1} \approx \omega_0, \tag{3.36}$$

to arrive at

$$\eta(\tau) \approx \mathrm{e}^{\omega_0(\tau+T)}. \tag{3.37}$$

Since $[-\partial_\tau^2 + \omega_y^2(\tau)]$ does not have vanishing eigenvalues, $\eta(\tau)$ is exponentially large everywhere in the interval $[-T, T]$ except near $\tau = -T$ when T is large. We can thus substitute $\eta(\tau)$ by its asymptotic behaviour (3.37) into Eq. (3.35) to obtain

$$J(T) = \frac{\eta(T)}{2\omega_0}. \tag{3.38}$$

The computation of $\eta(T)$ is simplified through relating Eq. (3.28a) to the Riccati equation

$$\frac{d\nu(\tau)}{d\tau} + \nu(\tau)^2 = \omega(\tau)^2,\ \nu(-T) = \omega_0, \tag{3.39}$$

where $\nu(\tau)$ and $\eta(\tau)$ are connected by the transformation

$$\eta(\tau) = \exp \int_{-T}^{\tau} d\tau' \nu(\tau') \tag{3.40}$$

while the ratio of the Jacobi fields becomes

$$\frac{J(\tau)}{J_0(\tau)} \approx \exp \int_{-T}^{T} d\tau \left(\nu(\tau) - \omega_0\right). \tag{3.41}$$

The value of α_2 is evaluated numerically to be

$$\alpha_2 = \exp -\frac{1}{2} \int_{-T}^{T} d\tau \left(\nu(\tau) - \omega_0\right) \approx 0.449 \quad \text{and} \quad \alpha = \alpha_1 \alpha_2 \approx 1.565\,. \tag{3.42}$$

Recasting the semiclassical calculation of the tunneling amplitude in units of the recoil energy finally yields

$$\frac{t}{E_R} \approx 1.861 \left(\frac{V_0}{E_R}\right)^{3/4} \exp\left[-1.582 \sqrt{\frac{V_0}{E_R}}\right]. \tag{3.43}$$

The same type of scaling laws has been obtained in the case of the two-dimensional square optical lattice [81, 85]. In the square-lattice geometry, however, the potential is separable and the semiclassical calculation proves much simpler as it reduces to using the well-known Mathieu equation for a one-dimensional periodic potential.

3.4.3 Exact numerical diagonalization

Plugging Bloch's theorem (2.12) into Eq. (3.20), we get a family of partial differential equations for the $u_{n\boldsymbol{k}}$s labeled by the Bloch vector $\boldsymbol{k} \in \Omega$ in the same

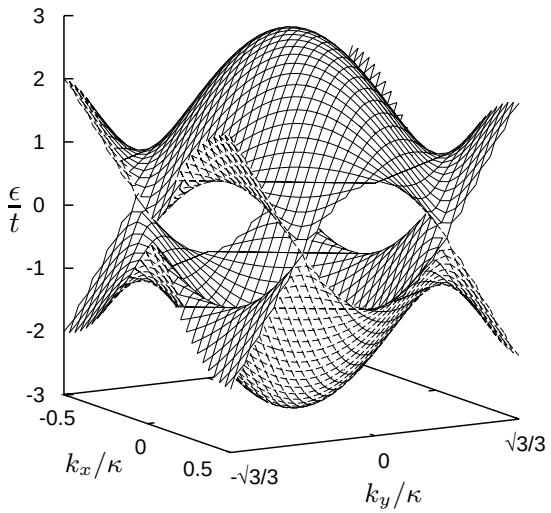

Figure 3.6: Numerically calculated band structure of the two lowest energy bands for $\hbar_e = 0.25$ at discrete points in the Brillouin zone Ω. The same conventions as in Fig. 2.4 are adopted. The value of t is determined by requiring that $\epsilon_\pm = \pm 3t$ at the center Γ of the Brillouin zone. The similarity with Fig. 2.4 shows that at $V_0 = 32E_R$ the tight-binding regime has already been reached.

rescaled units as in the previous paragraph. The band structure is then extracted by numerically solving

$$\begin{aligned} \mathcal{H}_{\boldsymbol{k}} u_{n\boldsymbol{k}}(\boldsymbol{r}) &= \epsilon_{n\boldsymbol{k}} u_{n\boldsymbol{k}}(\boldsymbol{r})\,, \\ \mathcal{H}_{\boldsymbol{k}} &= \frac{\hbar_e^2}{2}(-\mathrm{i}\boldsymbol{\nabla} + \boldsymbol{k})^2 + v(\boldsymbol{r}) \end{aligned} \tag{3.44}$$

for each $\boldsymbol{k} \in \Omega$ (expressed now in units of k_L).

The $u_{n\boldsymbol{k}}$s being $\mathcal{B}$-periodic as in Eq. (2.11), they are conveniently Fourier expanded in the reciprocal lattice $\tilde{\mathcal{B}}$ according to

$$u_{n\boldsymbol{k}}(\mathbf{r}) = \sum_{\boldsymbol{Q}\in\tilde{\mathcal{B}}} C_{n\boldsymbol{Q}}\, e^{\mathrm{i}\boldsymbol{Q}\cdot\mathbf{r}}. \tag{3.45}$$

Substituting Eq. (3.45) into Eq. (3.44), we can obtain the matrix representation of $\mathcal{H}_{\boldsymbol{k}}$ in the basis of $C_{n\boldsymbol{Q}}$, where $C_{n\boldsymbol{Q}}$s are ordered according to the increasing order of $|\boldsymbol{Q}|$. This matrix representation is sparse and banded, i.e. the lowest two

eigenvalues have relatively few non-zero $C_{n\boldsymbol{Q}}$s, leaving $C_{n\boldsymbol{Q}}$s with large $|\boldsymbol{Q}|$ to be practically zero. The actual computation can thus be carried out by enlarging the size of the matrix until the lowest few eigenvalues converge to the required accuracy and the number of non-zero $C_{n\boldsymbol{Q}}$s for all the converged eigenvalues are smaller than the size of the matrix. Typically, the convergence of the lowest 15 eigenvalues is sufficient to ensure the accuracy of the lowest two eigenvalues. The energy bands obtained in this way are exact and one can investigate their dependance on $\hbar_e$ as done in Fig. 3.6 and Fig. 3.7.

The essential feature is to realize that for an ideal honeycomb lattice, the band degeneracies at points K and K' are generic and do not depend on the actual value of the effective Planck's constant. Indeed the existence of two degeneracy points in the first Brillouin zone for the honeycomb lattice is a general consequence of the point group symmetries of the lattice; see Sec. 2.3.

This can be nicely illustrated in the weak V_0 limit (or equivalently when $\hbar_e$ is large). In this case, the particles are quasi-free since the energy of the bands are larger than V_0, that is above the saddle point separating the A and B sites (see Fig. 3.7), hence $u_{n\boldsymbol{k}}(\boldsymbol{r}) \approx 1$ and $C_{n\boldsymbol{Q}}$ is very small compared to $C_{n\boldsymbol{0}}$. The band spectrum can be understood in two steps. First, one folds the parabolic dispersion relation of the free particle into the first Brillouin zone (repeated-zone scheme [47]) and then one couples crossing levels at Bragg planes by the weak potential. At K_1, three plane waves fold with the same kinetic energy, namely $\boldsymbol{K}_1 = \boldsymbol{k}_1$, $\boldsymbol{K}_2 = \boldsymbol{k}_2$ and $\boldsymbol{K}_3 = \boldsymbol{k}_3$ (see Fig. 2.2). The weak periodic potential then couples these three plane wave states and the coupling matrix elements are all identical. As an illustration, substituting Eq. (3.45) into Eq. (3.44), we can obtain the coupling matrix in $C_{n\boldsymbol{Q}}$

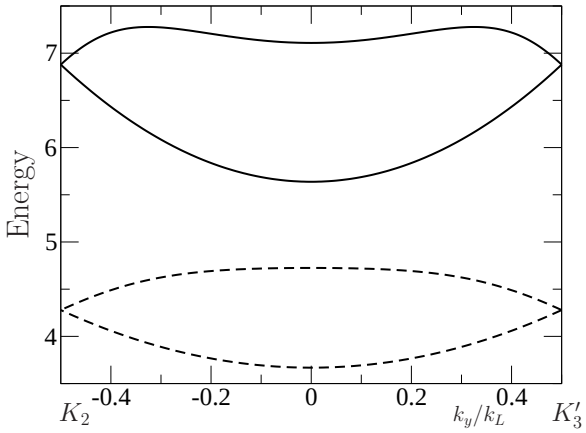

Figure 3.7: Band structure for nearly-free particles moving in a weak honeycomb optical potential in units of V_0. The first 2 levels are plotted as a function of k_y/k_L at $k_x/k_L = \sqrt{3}/2$, so along the vertical edge of Ω from K_2 to K_3'; see Fig. 2.2. The solid curves are obtained for $\hbar_e = \sqrt{2E_R/V_0} = \sqrt{10}$ and the dashed ones for $\hbar_e = \sqrt{5}$. As one can see the band structure is rather flat in the band centre but the levels curvature increases when $\hbar_e$ is increased. For small V_0 values, the energy of the bands are larger than V_0, that is above the saddle point separating the A and B sites, emphasizing that the corresponding Bloch states are not anymore localized in these two sites. The Dirac degeneracies in the ground state obtained at the Brillouin zone corners are generic and can be inferred from group-theoretic considerations. Note however that the conical intersections do not extend much over the first Brillouin zone when the potential is weak but start to spread when $\hbar_e$ is decreased.

representation at point K_1 as

$$\pm \begin{pmatrix} 3 & 1 & 1 \\ 1 & 3 & 1 \\ 1 & 1 & 3 \end{pmatrix} \begin{pmatrix} C_{\mathbf{0}} \\ C_{\boldsymbol{b}_1} \\ C_{-\boldsymbol{b}_2} \end{pmatrix} = \left(\epsilon_{\boldsymbol{K}} - \frac{\hbar_e^2 \boldsymbol{K}^2}{2} \right) \begin{pmatrix} C_{\mathbf{0}} \\ C_{\boldsymbol{b}_1} \\ C_{-\boldsymbol{b}_2} \end{pmatrix}, \quad \text{where} \quad V_0 = \pm \big| V_0 \big|. \tag{3.46}$$

In energy units of $\big|V_0\big|$, the eigenstates of this 3×3 matrix split into a singlet $\frac{1}{\sqrt{3}}(1,1,1)$ with eigenvalue $= \pm 5$ and a doublet $\{\frac{1}{\sqrt{2}}(1,0,-1), \frac{1}{\sqrt{6}}(1,-2,1)\}$ with eigenvalue $= \pm 2$. When V_0 is negative, the singlet is the ground state which is consistent with the triangular Bravais lattice obtained in this case ($\delta < 0$). When V_0 is positive ($\delta > 0$), the doublet becomes the ground state and features the tip of the conical intersection between the two sub-bands when the quasi-momentum is moved away from K; see Fig. 3.7.

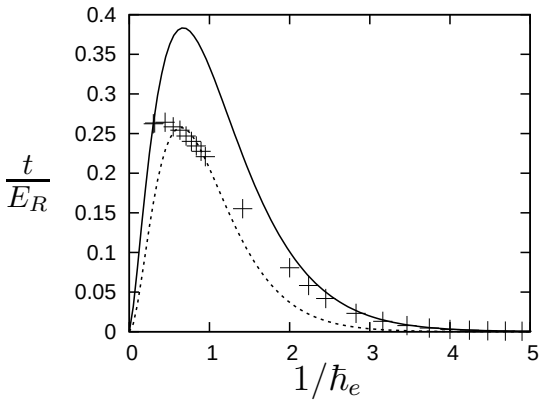

Figure 3.8: The hopping parameter t in units of the recoil energy E_R (crosses) as a function of the inverse of the effective Planck's constant $\hbar_e = \sqrt{2E_R/V_0}$ as obtained from the exact numerical computation. The harmonic approximation (dashed curve) and the semiclassical calculation (solid curve) of the hopping parameter have been added for comparison even if their range of validity is restricted to the tight-binding regime $\hbar_e \ll 1$.

The transition from a quasi-free particle to a tight-binding description occurs as $C_{n\boldsymbol{Q}}$ of higher energy becomes important such that the 3×3 matrix has to be enlarged. The transition value of $\hbar_e$ can be estimated when the energy difference is comparable to the sum of non-diagonal elements. In other words,

$$\text{energy difference} = \frac{\hbar_e^2}{2}(4-1) \approx 12 \Rightarrow \hbar_e \approx \sqrt{8}. \tag{3.47}$$

This transition is shown in Fig. 3.7 with two values around $\hbar_e = \sqrt{8}$.

From the exact numerical calculation, one can extract the slope of the dispersion relation at the Dirac points[3] and then the corresponding tunneling strength t as a function of $\hbar_e^{-1}$; see Fig. 3.8. Figure 3.9 gives the comparison between the exact calculation, the harmonic and the semiclassical calculations as a function of $\hbar_e^{-1}$ in the tight-binding regime where $\hbar_e \ll 1$. As one can see, the harmonic approximation is way off whereas the semiclassical estimate proves excellent. The deviation of the semi-classical estimate from the numerical t as one leaves the

[3]In the tight-binding regime, the slope is identical to $\frac{3at}{2}$ plus a negligible contribution from the next-nearest-neighbor tunneling amplitude.

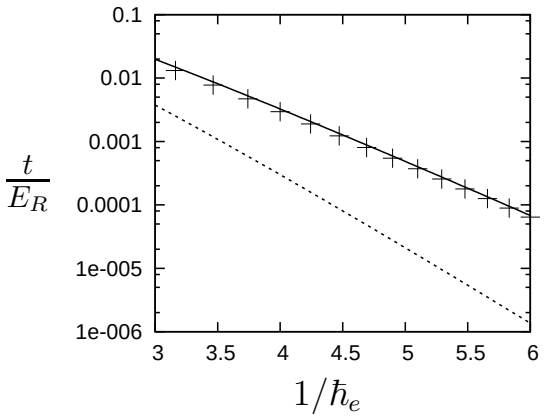

Figure 3.9: The hopping parameter t (in units of the recoil energy E_R) as a function of the inverse effective Planck's constant $\hbar_e = \sqrt{2E_R/V_0}$ in the tight-binding regime where $\hbar_e \ll 1$. As one can see, the harmonic approximation (dashed curve) is completely off. For example at $V_0 = 32E_R$ (or $\hbar_e = 0.25$), t is underestimated by a factor 10 and the discrepancy gets worse as V_0 increases. On the other hand, the agreement between the semiclassical calculation (solid curve) and the exact numerical computation (crosses) just proves excellent.

tight-binding regime might be a consequence of the significant contribution of the next-nearest-neighbor tunneling amplitude to the slope of the dispersion relation. However, our conjecture remains to be verified.

3.4.4 Reaching the massless Dirac fermion regime

In a typical experiment, $V_0 > 10E_R$ and $t \approx 0.0583E_R$ at $V_0 = 10E_R$. As can be seen from Fig. 3.7, for the conical intersection at the Dirac points to spread significantly over the Brillouin zone Ω, one needs to reach the tight-binding regime where V_0 is large enough (typically $V_0 > 10E_R$ will do). Taylor expansion of $\left|Z_{\boldsymbol{k}}\right|$ around the Dirac point gives

$$\left|Z_{\boldsymbol{K}+\boldsymbol{q}}\right| = \frac{3t}{2}a\left|\boldsymbol{q}\right|\sqrt{1+2g(\theta)a\left|\boldsymbol{q}\right|}, \tag{3.48}$$

where $g(\theta) = \cos^3\theta - \frac{3}{4}\cos\theta$, $\boldsymbol{q}$ being the small displacement from a Dirac point and θ is the angle between $\boldsymbol{q}$ and $\boldsymbol{a}_1$. Since $0 < \left|g(\theta)\right| < \frac{1}{4}$, it is sufficient to have

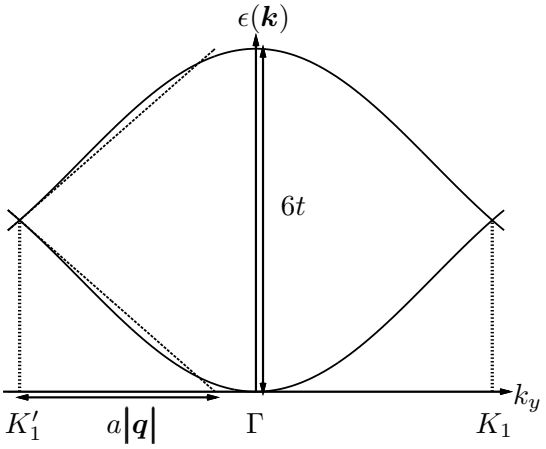

Figure 3.10: Cut of the linear dispersion approximation along Oy at $k_x = 0$ in the first Brillouin zone Ω as compared to the actual band spectrum in the tight-binding regime. At half-filling, the Fermi energy cuts the band spectrum at the Dirac points K and K'. Doping the system away from half-filling moves the Fermi energy up or down but the system can still be described in terms of massless Dirac fermions provided $a|\boldsymbol{q}| \ll 2$, i.e. provided the change in the Fermi energy is much less than the band-width $W = 6t$ itself. By the same token, thermal excitations of the system can still be described as thermal massless Dirac fermions provided $k_B T \ll W$.

$a|\boldsymbol{q}| \ll 2$ for the band structure to be well approximated by a linear dispersion relation around the Dirac points. The available energy range ΔE is thus set by the band-width $W = 6t$, namely $\Delta E \ll W$. So tuning the filling factor away from half-filling and residual thermal fluctuations will keep the system in the massless Dirac fermions regime provided $\mu, k_B T \ll W$ (Fig. 3.10). For example, at $V_0 = 32E_R$, the temperature constraint, as derived from Eq. (3.43), is $T < T_R/50$ whereas it is $T < T_R/2$ at $V_0 = 10E_R$. Choosing ^{6}Li atoms as the experimental candidate, the resonant recoil temperature $T_R = 3.5$ μK [86] and $T < 1.75$ μK at $V_0 = 10E_R$ while the current state-of-art technology is able to achieve minimum temperature of $0.05T_R = 0.175$ μK with 10^5 atoms (MIT experiments using Na atoms, see Ref. [31]). There is thus room left for reaching the massless Dirac fermions regime within the current state-of-art cooling technology.

3.5 Summary

We have proposed four ways for realizing a perfect honeycomb optical lattice. With the given optical potential, we estimated the tunneling amplitude using LCAO method, semi-classical method and exact diagonalization of the Hamilton operator. A comparison shows that the the semi-classical evaluation agrees well with the exact diagonalization in the regime $\hbar_e \ll 1$. We attributed the inaccuracy of the LCAO method to the incorrect approximation of the tail behaviour of the Wannier function. We showed that the temperature needed to access the massless Dirac fermion regime is within the reach of current technology. Finally, we have also provided an estimate of the optical potential strength at which our description of the fermions changes from quasi-free particle to localized particles.

Chapter 4

Distorted honeycomb optical lattice

The description of elementary excitations as massless Dirac fermions depends upon the very presence of the two conical intersections in the band structure. However, the existence of conical degeneracies is in turn based on group-theoretical arguments on the hexagonal symmetry of an ideal honeycomb lattice (see Sec. 2.3). In practice, it is impossible to control the laser configuration to the point of infinite accuracy, where all intensities and alignment angles are the same. Such imperfection would break the hexagonal symmetry that, following the group-theoretical arguments presented in Sec. 2.3, only one-dimensional representation is possible, therefore the conical degeneracies, if exist, cannot be predicted from the space group symmtery of the lattice anymore. We will show in the following that the massless Dirac fermion is indeed quite robust in the *tight-binding regime* and will survive small imperfections that are easily within experimental reach.

4.1 Possible distortions of the optical lattice

To simplify the analysis, we consider in-plane laser beams with different (positive) strengths $E_n = s_n E_0$ and with respective angles away from $2\pi/3$, see Fig. 4.1(a). It is important to note that we will always stick to imperfections which are compatible with a two-point Bravais cell. They will only induce distortions of the hexagonal spatial structure of the field minima but without breaking this pattern.

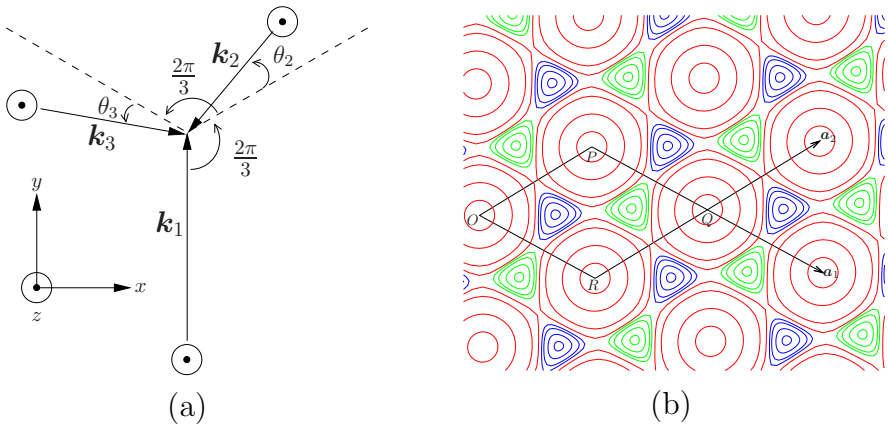

Figure 4.1: (a) The asymmetric in-plane 3-beam configuration. Three monochromatic and linearly-polarized laser beams with wave vectors $\boldsymbol{k}_n$ interfere with different strengths $E_n = s_n E_0$ $(n = 1, 2, 3)$. The respective angles depart from $2\pi/3$. (b) Distorted optical lattice obtained with $\vartheta_3 = \vartheta_2 = 5 \times 10^{-2}$ and $s_1 = 1$, $s_2 = 1.03$, $s_3 = 0.97$. The color convention is the same as in Fig. 3.3. For weak enough distortions, the primitive diamond-shape cell Σ still contains two field minima as evidenced in the plot.

The new optical lattice potential is now given by $V'(\boldsymbol{r}) = V_0 \left| f'(\boldsymbol{r}) \right|^2$ with the new total dimensionless field amplitude

$$f'(\boldsymbol{r}) = s_1 + s_3 \exp(-\mathrm{i}\boldsymbol{b}'_1 \cdot \boldsymbol{r}) + s_2 \exp(\mathrm{i}\boldsymbol{b}'_2 \cdot \boldsymbol{r}). \tag{4.1}$$

Here the $\boldsymbol{b}'_n$ $(n{=}1{,}2)$ feature the new reciprocal lattice basis vectors defined by $\boldsymbol{b}_1 = \boldsymbol{k}_3 - \boldsymbol{k}_1$ and $\boldsymbol{b}_2 = \boldsymbol{k}_1 - \boldsymbol{k}_2$ and the new parameterization of the wave vectors

is given by

$$\begin{aligned}
\boldsymbol{k}_1 &= k_L \boldsymbol{e}_y, \\
\boldsymbol{k}_2 &= k_L \Big(-\cos(\pi/6 + \theta_2)\boldsymbol{e}_x - \sin(\pi/6 + \theta_2)\boldsymbol{e}_y \Big), \\
\boldsymbol{k}_3 &= k_L \Big(\cos(\pi/6 - \theta_3)\boldsymbol{e}_x - \sin(\pi/6 - \theta_3)\boldsymbol{e}_y \Big).
\end{aligned} \tag{4.2}$$

They define in turn a new set of Bravais lattice basis vectors $\boldsymbol{a}'_n$ giving rise to a new primitive diamond-shaped cell Σ'. Unless the angle mismatches vanish, the new Bravais and reciprocal lattices are no longer hexagonal but oblique with no special symmetry except for inversion. As a consequence, the new first Brillouin zone Ω' is still a hexagon but *no longer a regular one*.

Since we assume a two-point primitive cell, the minima of the new optical potential still identify with zeros of $f'(\boldsymbol{r})$. We can differentiate Eq. (4.1) to obtain the minima that satisfy

$$\begin{aligned}
\cos(\boldsymbol{b}'_1 \cdot \boldsymbol{r}) &= \frac{s_2^2 - s_3^2 - s_1^2}{2 s_1 s_3}, \\
\cos(\boldsymbol{b}'_2 \cdot \boldsymbol{r}) &= \frac{s_3^2 - s_2^2 - s_1^2}{2 s_1 s_2},
\end{aligned} \tag{4.3}$$

subject to the condition $s_2 \sin(\boldsymbol{b}'_2 \cdot \boldsymbol{r}) = s_3 \sin(\boldsymbol{b}'_1 \cdot \boldsymbol{r})$ such that both $\boldsymbol{b}'_1 \cdot \boldsymbol{r}$ and $\boldsymbol{b}'_2 \cdot \boldsymbol{r}$ lie in the same quadrant. Correspondingly, the new displacement vectors that connect an A site to its three nearest B sites are

$$\begin{aligned}
\boldsymbol{c}'_1 &= \left(1 - \frac{\boldsymbol{b}'_1 \cdot \boldsymbol{r}}{\pi}\right) \boldsymbol{a}'_1 + \left(1 - \frac{\boldsymbol{b}'_2 \cdot \boldsymbol{r}}{\pi}\right) \boldsymbol{a}'_2, \\
\boldsymbol{c}'_2 &= -\left(\frac{\boldsymbol{b}'_1 \cdot \boldsymbol{r}}{\pi}\right) \boldsymbol{a}'_1 + \left(1 - \frac{\boldsymbol{b}'_2 \cdot \boldsymbol{r}}{\pi}\right) \boldsymbol{a}'_2, \\
\boldsymbol{c}'_3 &= \left(1 - \frac{\boldsymbol{b}'_1 \cdot \boldsymbol{r}}{\pi}\right) \boldsymbol{a}'_1 - \left(\frac{\boldsymbol{b}'_2 \cdot \boldsymbol{r}}{\pi}\right) \boldsymbol{a}'_2.
\end{aligned} \tag{4.4}$$

4.2 Criteria for massless Dirac fermions

The criteria for the existence of massless Dirac fermions is obtained by considering unbalanced tunneling amplitudes within the tight-binding regime [87]. The situation corresponds to slightly distorted honeycomb lattice where each lattice site still possesses three nearest neighbors but the tunneling amplitudes in the three directions might be unequal. In a real graphene, such distortion can be achieved through stretching the graphene sheet. The tight-binding energy is given by $\epsilon_{\pm,\boldsymbol{k}} = \pm\big|Z_{\boldsymbol{k}}\big|$, where $Z_{\boldsymbol{k}}$ is defined in Eq. (2.27). The degeneracies are found at points $\boldsymbol{k}_D \in \Omega$ canceling $Z_{\boldsymbol{k}} = 0$. This condition boils down to geometrically sum up three vectors to zero in the two-dimensional plane, with the three vectors forming a closed triangle when connected head to tail; see Fig. 4.2. As such, a solution is only possible provided the hopping amplitudes satisfy one of the norm inequalities given by

$$\Big|\big|t_2\big| - \big|t_3\big|\Big| \leq \big|t_1\big| \leq \big|t_2\big| + \big|t_3\big| \tag{4.5}$$

and cyclic permutations such that the sum of magnitude of any two vectors is greater than the third one. If this is the case, defining the angles $\varphi_{1,2} = \arg t_{2,3} - \arg t_1$, the Dirac points solve

$$\begin{aligned}
\cos(\boldsymbol{k}_D\cdot\boldsymbol{a}_1' - \varphi_1) &= \frac{\big|t_3\big|^2 - \big|t_2\big|^2 - \big|t_1\big|^2}{2\big|t_1 t_2\big|},\\
\cos(\boldsymbol{k}_D\cdot\boldsymbol{a}_2' - \varphi_2) &= \frac{\big|t_2\big|^2 - \big|t_3\big|^2 - \big|t_1\big|^2}{2\big|t_1 t_3\big|},
\end{aligned} \tag{4.6}$$

subject to the condition

$$\big|t_2\big|\sin(\boldsymbol{k}_D\cdot\boldsymbol{a}_1' - \varphi_1) + \big|t_3\big|\sin(\boldsymbol{k}_D\cdot\boldsymbol{a}_2' - \varphi_2) = 0. \tag{4.7}$$

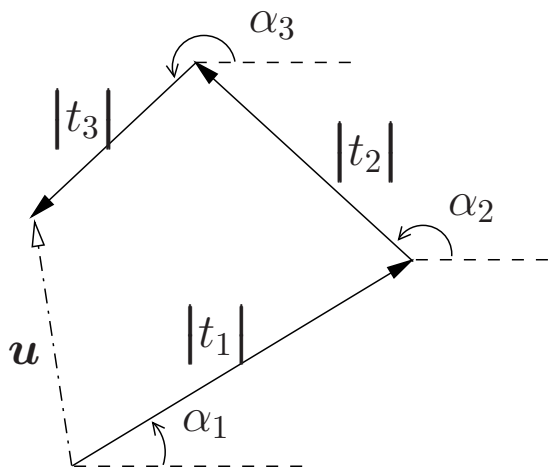

Figure 4.2: The condition $Z_{\boldsymbol{k}} = 0$ is equivalent to cancel the resultant vector $\boldsymbol{u}$ of three vectors, each with length $|t_n|$ and polar angle $\alpha_n = \boldsymbol{k} \cdot \boldsymbol{c}_n + \arg(t_n)$. There will always be a solution provided one of the norm inequalities $\big||t_2| - |t_3|\big| \leq |t_1| \leq |t_2| + |t_3|$ (and cyclic permutations) is satisfied.

We find the important result that the system self-adapts to changes in the hopping amplitudes by shifting the Dirac points away from the corners of the Brillouin zone until the norm inequalities (4.5) break and degeneracies disappear. Thus, provided the hopping imbalance is not too strong, the massless Dirac fermions do survive imperfections in the system and the hexagonal symmetry breaking.

We illustrate this important feature in the simple case of only one unbalanced hopping amplitude, namely $t_1 = -\gamma t$, $t_2 = t_3 = -t$. We further choose γ real and $0 < |\gamma| \leq 2$ for the Dirac points to exist. We then find two Dirac points D_γ and D'_γ given by $\boldsymbol{k}_D = -\boldsymbol{k}'_D = \varphi_0(\boldsymbol{b}_2 - \boldsymbol{b}_1)$ where $\varphi_0 \in [0, 1/2]$ solves $\cos(2\pi\varphi_0) = -\gamma/2$. This means that the two Dirac points D_γ and D'_γ move along opposite paths in the Brillouin zone Ω. The fact that Dirac points always come in by pairs of opposite location in Ω is generic [88]. When γ is increased from 0 to 2, D_γ starts at $\boldsymbol{k}_0 = (3k_L/4)\,\mathbf{e}_y$ for $\gamma = 0$, then moves along axis Oy and reach corner K_1 at $\gamma = 1$. Note that when $\gamma \to 0$, the physical situation is that of weakly coupled "zig-zag" linear chains. For $\gamma > 1$, D_γ leaves Ω but a translation in reciprocal lattice brings it back on the vertical edges of Ω (technically we get two copies of

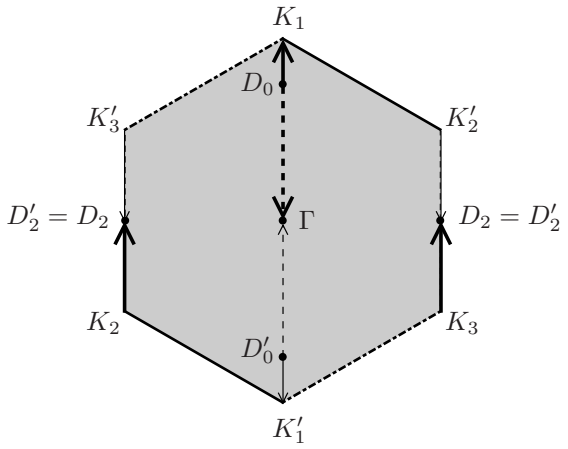

Figure 4.3: When the three hopping amplitudes t_n are unbalanced, the Dirac points are shifted in the Brillouin zone Ω and disappear when the norm inequality $\big||t_2| - |t_3|\big| \leq |t_1| \leq |t_2| + |t_3|$ is no longer satisfied. We depict here how the Dirac points D_γ and D'_γ move in Ω when only one hopping amplitude is unbalanced, namely $t_1 = -\gamma t$ and $t_2 = t_3 = -t$. Points D_γ (thick path) and D'_γ (thin path) move along opposite paths. Increasing γ from 0, point D_γ starts at D_0 and moves upward. It reaches point K_1 at $\gamma = 1$ (balanced amplitudes case) then moves along the vertical edge of Ω where it reaches its middle point D_2 at $\gamma = 2$. The Dirac points cease to exist when $\gamma > 2$. For negative γ, D_γ moves downward from D_0 (dotted thick path), reaches the zone center Γ for $\gamma = -2$ and then ceases to exist for $\gamma < -2$.

the same point). D_γ reaches the middle of the vertical edge at $\gamma = 2$ where it merges with D'_γ into a *single* Dirac point, see Fig. 4.3. As soon as $\gamma > 2$, the degeneracy is lifted and the massless Dirac fermions do not exist anymore. For negative γ, D_γ and D'_γ move back from $\pm(3k_L/4)\,\mathbf{e}_y$ to the centre Γ of the Brillouin zone where they merge and disappear, see Fig. 4.3. The fact that Dirac points can only merge at the centre and mid-edge points of Ω is also generic [88].

As a side remark, the linear dispersion around the shifted Dirac points is no longer isotropic, i.e. $\epsilon_{\pm,\boldsymbol{K}+\boldsymbol{q}} = \hbar\sqrt{v_\parallel^2 \boldsymbol{q}_\parallel^2 + v_\perp^2 \boldsymbol{q}_\perp^2}$ and $v_\parallel \neq v_\perp$. Similar anisotropic dispersion relation may be achieved by applying a periodic potential to a homogeneous sample of graphene [89]. However, the origins of the anisotropy are quite different in the two situations. In the former case of distorted lattice, the excitations travel with larger group velocity in the direction with larger tunneling amplitude, which is intuitively clear. In the latter case of graphene under periodic

potential, it is noted that the group velocity is largest in the direction of crossing potential barrier and this phenomenon has been attributed to chiral tunneling of Dirac fermions [89, 90].

In the next section, we will examine separately the effect of field strength imbalance and alignment angle mismatch in the spirit of unequal tunneling amplitudes.

4.3 Transition between semi-metal and band insulator

4.3.1 Critical field strength imbalance

To give an estimate of the critical field strength imbalance beyond which the Dirac points cannot survive, we consider the simplest case of only one unbalanced laser beam and no angle mismatch, namely $\theta_2 = \theta_3 = 0$, $s_1 = 1 + \eta$ and $s_2 = s_3 = 1$. In this case the Bravais lattice, the reciprocal lattice, the primitive cell Σ and the Brillouin zone Ω are *not* modified, but the positions of minima within Σ are shifted. The new optical potential $V'(\boldsymbol{r}) = V_0 v'(\boldsymbol{r})$ reads

$$\begin{aligned} v'(\boldsymbol{r}) &= v(\boldsymbol{r}) + 2\eta\,\delta v(\boldsymbol{r}) + \eta(\eta+2), \\ \delta v(\boldsymbol{r}) &= \cos(\boldsymbol{b}_1\cdot\boldsymbol{r}) + \cos(\boldsymbol{b}_2\cdot\boldsymbol{r}), \end{aligned} \tag{4.8}$$

where $v(\boldsymbol{r})$ is given by Eq. (3.9). Note that when only one field strength is unbalanced, the corresponding potential still displays a reflection symmetry. In the present case, it is the Ox-reflection symmetry because $V'(\boldsymbol{r})$ is invariant under the exchange $\boldsymbol{b}_1 \leftrightarrow \boldsymbol{b}_2$. Requiring now that the primitive cell Σ exhibits two field minima imposes $-1 \leq \eta \leq 1$. Their positions in Σ are given by $\boldsymbol{r}'_{\mathrm{A,B}} = \varphi_{\mathrm{A,B}}\,(\boldsymbol{a}_1 + \boldsymbol{a}_2)$ with $\cos(2\pi\varphi_{\mathrm{A,B}}) = -(1+\eta)/2$. Their mid-point $\boldsymbol{r}'_{\mathrm{S}} = (\boldsymbol{r}'_{\mathrm{A}} + \boldsymbol{r}'_{\mathrm{B}})/2 = (\boldsymbol{a}_1 + \boldsymbol{a}_2)/2$ is a saddle point and defines the potential barrier height V'_{S} to cross to go from A

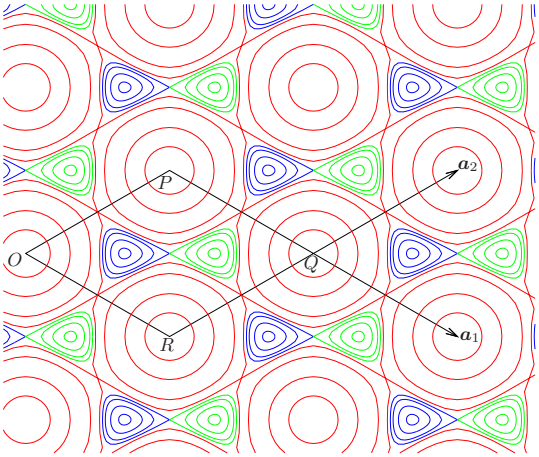

Figure 4.4: Slightly distorted lattice obtained with vanishing mismatch angles and one unbalanced field strength, namely $s_1 = 10/9$ and $s_2 = s_3 = 1$. The color convention is the same as in Fig. 3.3. In this particular case the hexagon of field minima is slightly squeezed along the horizontal axis Ox and the vectors $\boldsymbol{c}'_n$ connecting a given minimum to its three nearest neighbors have now different lengths. In the situation depicted $|\boldsymbol{c}'_2| = |\boldsymbol{c}'_3| \neq |\boldsymbol{c}'_1|$. In turn, due to the reflection symmetry about Ox, the tight-binding hopping amplitudes satisfy $|t_2| = |t_3| \neq |t_1|$.

and B in Σ. One finds $V'_s = (\eta - 1)^2 V_0$.

As a whole the field minima organize in a hexagon which is stretched (η negative) or compressed (η positive) along Ox, see Fig. 4.4. As a consequence two of the three new vectors $\boldsymbol{c}'_n$ joining one minimum to its three nearest neighbors will have equal length. In the present situation we get $|\boldsymbol{c}'_2| = |\boldsymbol{c}'_3| \neq |\boldsymbol{c}'_1|$. The potential barrier height V''_s to cross to go from A to B along $\boldsymbol{c}'_2$ and $\boldsymbol{c}'_3$ is given by the corresponding saddle points located at the middle of the edges of Σ. One finds $V''_s = (\eta + 1)^2 V_0$.

Now, when η is increased from 0, the minima move closer along $\boldsymbol{c}'_1$ and move away along $\boldsymbol{c}'_2$ and $\boldsymbol{c}'_3$. At the same time, the potential barrier V'_s along $\boldsymbol{c}'_1$ is lowered and the the potential barrier V''_s along $\boldsymbol{c}'_2$ and $\boldsymbol{c}'_3$ is increased. As a net effect, in the tight-binding picture, we expect the tunneling amplitude $|t_1|$ to increase while $|t_2|$ and $|t_3|$ decrease. We get the opposite conclusion when η is lowered from 0. Since the potential is invariant through $\boldsymbol{b}_1 \leftrightarrow \boldsymbol{b}_2$, we further have $|t_2| = |t_3|$ and we recover the case of one unbalanced hopping amplitude analyzed in the previous

section.

By inspection of the semiclassical expression (3.21), we expect the ratio $\left|t_1/t_2\right|$ to scale as $\exp(\Delta S(\eta)/\hbar_e)$ at leading order, where $\Delta S(\eta)$ is the action difference between the two instanton trajectories linking sites A and B along $\boldsymbol{c}_2'$ and $\boldsymbol{c}_1'$ respectively. For small enough η we expect $\Delta S(\eta)$ to grow linearly with η, the slope being positive since the ratio $\left|t_1/t_2\right|$ should increase with η. The Dirac degeneracies disappear when this ratio is 2 (see previous section), thus we get the semiclassical prediction that this will happen when $\eta \propto \hbar_e$. This result can also be inferred by saying that the Dirac points will disappear as soon as the perturbing potential $2\eta\delta V(\boldsymbol{r})$, see Eq. (4.8), strongly mixes the unperturbed states. This will happen when the corresponding coupling energy equals the mean level spacing of the unperturbed system, which is approximately $\hbar\omega_0$ in the tight-binding regime, and we get back to the prediction $\eta \propto \hbar_e$.

To check our semiclassical prediction we have computed, for each value of the effective Planck's constant $\hbar_e$, the ground state and first excited-state levels for different values of η and we have extracted the corresponding critical value η_c for which the Dirac degeneracies are lifted. Figure 4.5 gives an example of the band structure obtained at $\hbar_e = 1/\sqrt{40} \approx 0.16$ for η ranging from 0 to 0.054. We have then plotted η_c as a function of $\hbar_e$, see Fig. 4.6. We have fitted the data with the quadratic fit function $\alpha\hbar_e + \beta\hbar_e^2$ and found $\alpha \approx 0.1074$ and $\beta \approx 0.0624$ enforcing the very good agreement obtained with our linear prediction in the semiclassical regime $\hbar_e \ll 1$. The quadratic correction could certainly be inferred from semiclassical higher-order corrections.

We would like to emphasize at this point that increasing or decreasing η from 0 is not symmetrical. When η is decreased from 0, the Dirac degeneracies are predicted to disappear when $\left|t_1/t_2\right| \to 0$. However the best that we can do is to let $\eta \to -1$. This unfortunately means that one laser beam is almost extinguished

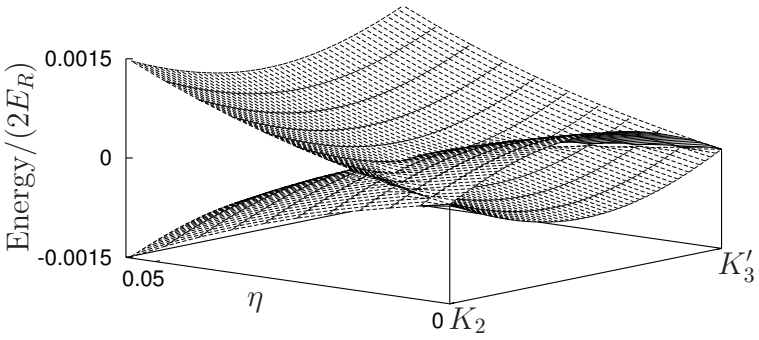

Figure 4.5: The band diagram for the two lowest levels as a function of η for $V_0 = 80E_R$ ($\hbar_e \approx 0.158$). The bands are plotted along the vertical straight line joining the Dirac points K_2 and K_3' of the balanced situation; see Fig. 2.2. The origin of energy is fixed at the Fermi energy for a half-filled band and all bands have been shifted such that the upper and lower bands intersect at zero energy difference.

and the situation is more that of very weakly coupled one-dimensional chains, an interesting situation that is proposed for spin-gap system [91]. We thus see that decreasing slightly η from 0 does not harm the Dirac degeneracies. They move inside Ω but do survive. On the other hand, increasing slightly η from 0 does destroy the Dirac degeneracies as soon as $\eta \sim \hbar_e$.

As one can see from the plots, the tolerance about the intensity mismatch of the laser beams increases with $\hbar_e$, or equivalently when the optical lattice depth V_0 decreases. On the other hand, as we have already seen, the Dirac cones do not extend much over the Brillouin zone if V_0 is too small. So there is a trade-off to make. The situation is however really favorable since the intensity mismatch tolerance is already in the 10% range for $V_0 \sim 10E_R$. This means that the massless Dirac fermions prove quite robust and should be easily accessed experimentally.

4.3.2 Critical in-plane angle mismatch

We now estimate the critical angle mismatch when all laser beams have the same intensities ($s_1 = s_2 = s_3 = 1$). We see from Eq. (4.1) that the new optical potential still displays the exchange symmetry $\boldsymbol{b}_1' \leftrightarrow \boldsymbol{b}_2'$ and thus a reflection invariance with

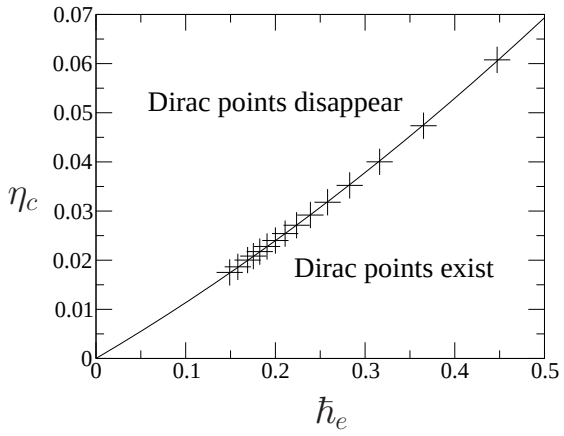

Figure 4.6: The critical laser strength imbalance η_c at which the Dirac degeneracies are lifted as a function of the effective Planck's constant $\hbar_e = \sqrt{2E_R/V_0}$. The solid line corresponds to a quadratic fit of the numerical data. The linear coefficient is $\alpha \approx 0.1074$ while the quadratic one is $\beta \approx 0.0624$. As one can see our numerical results are in good agreement with our semiclassical prediction $\eta_c \propto \hbar_e$. The degree of control of the intensity imbalance of the laser fields gets more stringent as the optical lattice depth V_0 is increased. Nevertheless, at already $V_0 = 20E_R$ ($\hbar_e \approx 0.3$), the laser intensities should all be equal within 8% which does not sound particularly demanding.

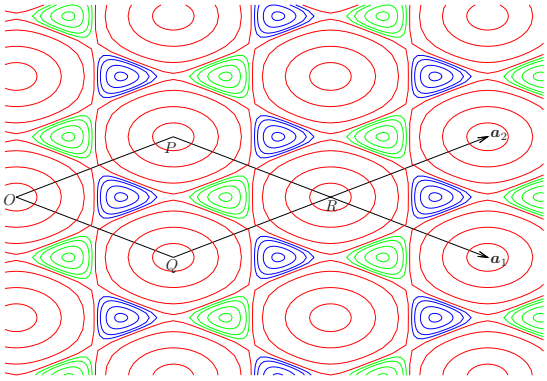

Figure 4.7: Distorted lattice obtained with balanced field strengths $s_n = 1$ and angle mismatch $\theta_3 = -\theta_2 = -\pi/10$. The color convention is the same as in Fig. 3.3. In this particular case the hexagon of field minima is stretched along the horizontal axis Ox and the vectors $\boldsymbol{c}'_n$ connecting a given minimum to its three nearest neighbors have now different lengths. In the situation depicted $|\boldsymbol{c}'_2| = |\boldsymbol{c}'_3| \neq |\boldsymbol{c}'_1|$. In turn, due to the reflection symmetry about Ox, the tight-binding hopping amplitudes satisfy $|t_2| = |t_3| \neq |t_1|$.

respect to their bisectrix. In the following we stick to the simple case where $\theta_3 = -\theta_2 = \theta$ and θ is small. In this case both the Bravais lattice, the reciprocal lattice, the Brillouin zone Ω and the diamond-shaped primitive cell Σ get modified.

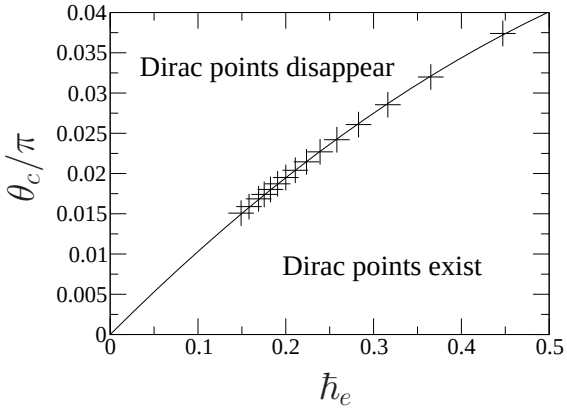

Figure 4.8: The critical angle mismatch θ_c (in units of π) beyond which the Dirac degeneracies disappear as a function of the effective Planck's constant $\hbar_e = \sqrt{2E_R/V_0}$. The dashed line corresponds to a quadratic fit of the numerical data. The linear coefficient is 0.109 while the quadratic one is -0.0577. As one can see our numerical results are in good agreement with our semiclassical prediction $\theta_c \propto \hbar_e$. The degree of control of the angle mismatch gets more stringent as the optical lattice depth V_0 is increased. Nevertheless, at already $V_0 = 20E_R$ ($\hbar_e \approx 0.3$), the angle mismatch should be less than 5° which is not particularly demanding.

The new reciprocal basis vectors turn out to be $\boldsymbol{b}'_1 = \boldsymbol{b}_1 + \boldsymbol{\delta b}_1$, $\boldsymbol{b}'_2 = \boldsymbol{b}_2 + \boldsymbol{\delta b}_2$ where $\boldsymbol{\delta b}_1 = (\theta/\sqrt{3})\,\boldsymbol{b}_2$ and $\boldsymbol{\delta b}_2 = (\theta/\sqrt{3})\,\boldsymbol{b}_1$. Since the exchange symmetry $\boldsymbol{b}_1 \leftrightarrow \boldsymbol{b}_2$ is again preserved, the new potential continues to display the Ox-reflection invariance. Figure 4.7 gives a plot of the new potential structure for $\theta = -\pi/10$.

This situation boils down again to the case of one unbalanced tunneling amplitude. Indeed, the angle between the $\boldsymbol{b}'_1$ and $\boldsymbol{b}'_2$ decreases when θ is increased from 0. In turn the angle between the corresponding $\boldsymbol{a}'_n$ increases and the hexagon structure made by the A and B minima get compressed along Ox. The opposite conclusion holds when θ is decreased from 0. We get again the situation where $\left|t_2\right| = \left|t_3\right| \neq \left|t_1\right|$ and $\left|t_1/t_2\right| \geq 1$ when $\theta \geq 0$ and vice-versa. Like for the field strength imbalance, the situations $\theta > 0$ and $\theta < 0$ are not symmetric. The masless Dirac fermions prove more sensitive to *closing* the angle between the $\boldsymbol{b}'_n$, which corresponds to $\theta_3 = -\theta_2 = \theta > 0$. This is because $\left|t_1/t_2\right|$ increases and the threshold $\left|t_1/t_2\right| = 2$ is more rapidly hit. This is the situation we explore.

Applying the same reasoning as before, we thus predict the critical angle mis-

match beyond which the massless Dirac fermions are destroyed to scale as $\theta_c \propto \hbar_e$. Again, to get θ_c as a function of $\hbar_e$, we numerically compute the band structure at a given $\hbar_e$ for different in-plane mismatch angles θ and then extract the value θ_c for which the Dirac degeneracy is lifted. We then repeat the procedure for different $\hbar_e$. As one can see, our prediction is in very good agreement with the numerical calculations (see Fig. 4.8) and well supported by a quadratic fit. As θ_c increases with $\hbar_e$, there is a trade-off to make between reaching the tight-binding regime where V_0 is large and achieving an experimentally reasonable angle mismatch tolerance which requires V_0 to be small. The trade-off turns out to be a favorable one since already for $V_0 = 20E_R$ ($\hbar_e \approx 0.3$), one gets a tolerance of about 5° on the laser beams alignment. We expect the same type of scaling for small out-of-plane angle mismatches. Furthermore, when several small distortions combine, their effects should add up and thus the critical imperfection threshold should still scale with $\hbar_e$.

As an overall conclusion we see that massless Dirac fermions are quite robust to moderate lattice distortions. Demonstrating them in an experiment should not be particularly demanding in terms of the control of the laser configuration.

4.4 Distorted lattice with weak optical potential

We have seen in Chapter 3 that massless Dirac fermions exist in an ideal honeycomb optical lattice (regardless of the optical potential strength) because of the point group symmtery while their existence in a deep optical lattice (the tight-binding regime) can be analyzed in terms of a geometrical relation between three tunneling amplitudes to the nearest neighbors. We shall attempt in the following to reconcile these two pictures on the origin of massless Dirac fermions and extend the reasoning to a distorted lattice with arbitrary weak optical potential strength. The analysis

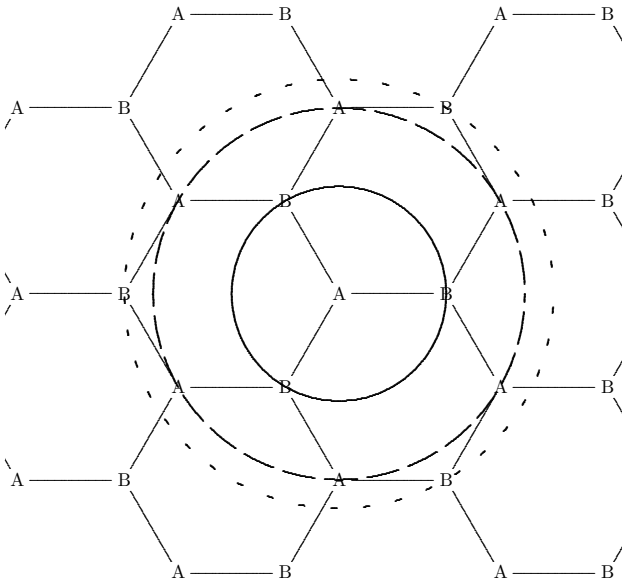

Figure 4.9: The neighbors of an A-site. From inside out, the circles (centered on an A-site) pass through 3 nearest neigbors (solid circles, B-sites), 6 next-nearest neighbors (dashed circles, A-sites) and 3 next-next-nearest neighbors (dotted circles, B-sites).

is broken down into asking two questions: (1) under what condition would the two bands intersect, and (2) under what condition would the dispersion relations around the intersection points remain to be conical.

The first question has been addressed in Ref. [88]. As we decrease the optical potential strength from a tight-binding regime, we have to include the next-nearest-neighbor hoppings, followed by the next-next-nearest-neighbor hoppings and so on, as the optical potential strength is decreased, see Fig. 4.9. The Hamilton operator (2.34) has to be written in a more general form (treating the two sublattices as equivalent),

$$H = \sum_{\boldsymbol{k}\in\Omega,\sigma} (f^\dagger_{\mathrm{A}\boldsymbol{k}\sigma}, f^\dagger_{\mathrm{B}\boldsymbol{k}\sigma}) \mathcal{H}_{\boldsymbol{k}} \begin{pmatrix} f_{\mathrm{A}\boldsymbol{k}\sigma} \\ f_{\mathrm{B}\boldsymbol{k}\sigma} \end{pmatrix}, \quad \mathcal{H}_{\boldsymbol{k}} = \begin{pmatrix} Y_{\boldsymbol{k}} & \tilde{Z}_{\boldsymbol{k}} \\ \tilde{Z}^*_{\boldsymbol{k}} & Y_{\boldsymbol{k}} \end{pmatrix}, \tag{4.9}$$

where

$$Y_{\boldsymbol{k}} = \sum_{\boldsymbol{R}\in\mathcal{B}} t_s(\boldsymbol{R}) \mathrm{e}^{\mathrm{i}\boldsymbol{k}\cdot\boldsymbol{R}} \quad \text{with} \quad t_s(\boldsymbol{R}) = \langle w_{\boldsymbol{R}_\mathrm{A}} | H | w_{\boldsymbol{R}_\mathrm{A}+\boldsymbol{R}} \rangle \tag{4.10}$$

and

$$\tilde{Z}_{\boldsymbol{k}} = \sum_{\boldsymbol{R}\in\mathcal{B}} t_d(\boldsymbol{R}) \mathrm{e}^{\mathrm{i}\boldsymbol{k}\cdot(\boldsymbol{c}_1' + \boldsymbol{R})} \quad \text{with} \quad t_d(\boldsymbol{R}) = \langle w_{\boldsymbol{R}_\wedge} | H | w_{\boldsymbol{R}_\wedge + \boldsymbol{c}_1' + \boldsymbol{R}} \rangle. \tag{4.11}$$

In this convention, t_s is the tunneling parameter between sites of the same sublattice while t_d refers to the tunneling parameter between sites of different sublattices. In particular, $t_s(\mathbf{0})$ is the on-site energy ϵ_0 and $t_d(\mathbf{0}) = -t$ is the nearest-neighbor tunneling parameter, following our convention in the tight-binding regime. For each value of $\boldsymbol{k} \in \Omega$, the two bands are split by the energy $2|\tilde{Z}_{\boldsymbol{k}}|$, hence we may continue to use Fig. 4.2 for analysis on the band intersection points, but we have to change the closed triangle to a closed polygon, with the number of sides determined by the number of tunneling amplitudes included in the analysis. Clearly, any arbitrary small distortion of the lattice (that does not break the equivalence between the two sublattices) will distort the closed polygon such that the bands intersect at two $\boldsymbol{k}$ points other than the $\boldsymbol{K}$ and $\boldsymbol{K}$' points. In fact, this was investigated in Ref. [88] and it was found that the intersection points would move and merge at fixed points in the 1BZ when the values of tunneling parameters are changed. Therefore, we may conclude that it is sufficient to explain the band intersection points within the tunneling picture.

The second question is about how far does the conical region extend around an intersection point. This question has to be answered by analyzing $Y_{\boldsymbol{k}}$ and this was not carried out in Ref. [88], since the paper focused on the tight-binding regime. In Fig. 4.10, we illustrate the effect of the next-nearest-neighbor tunneling parameter t_{nn} in an ideal honeycomb lattice. Each lattice site has six next-nearest neighbors (Fig. 4.9) with equal tunneling parameters in these six directions. As the optical potential strength is decreased, t_{nn} increases in magnitude and results in the bending of the upper band. Consequently, the region around the Dirac points

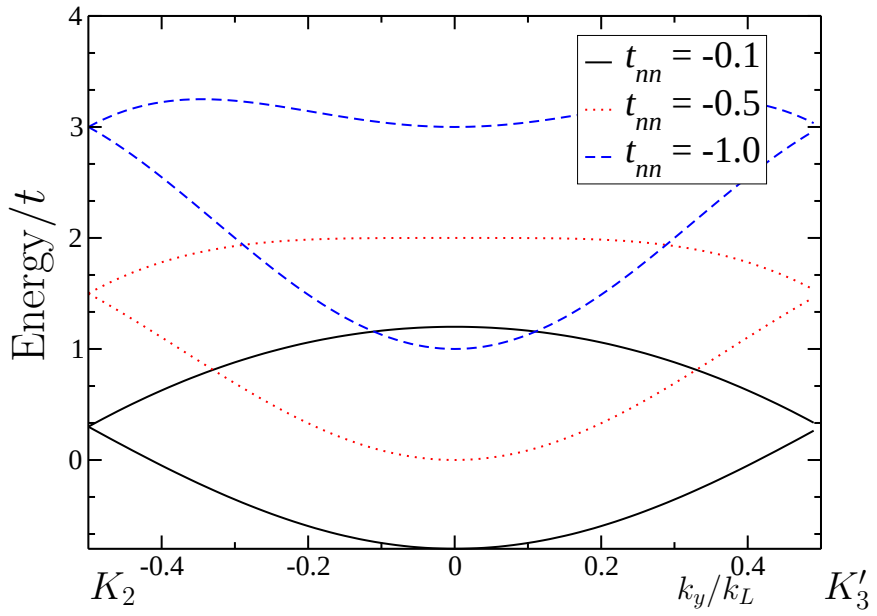

Figure 4.10: Effect of the next-nearest-neighbor tunneling parameter t_{nn}. The on-site energy ϵ_0 is set to zero and the nearest-neighbor tunneling parameter is set to $-t = -1$. The bending of the upper band is more obvious and the turning points ($\frac{\partial}{\partial k_y}\text{Energy}\big|_{k_x=0.5\kappa} = 0$) move closer to K_2 and K_3' when t_{nn} becomes comparable to $-t$.

with linear dispersion relation is reduced, as we have discussed in the previous chapter. Nevertheless, the symmetry of the perfect honeycomb lattice guarantee that $Y_{\boldsymbol{K}+\boldsymbol{q}} = \text{constant} + \mathcal{O}(\boldsymbol{q}^2)$ for small $|\boldsymbol{q}|$, hence there is a finite region with conical dispersion around the Dirac points for arbitrary weak potential strength such that Dirac fermions are robust to arbitrary small distortion. In these sense, symmetry of the lattice seems to be important.

As a side remark, the curve obtained from exact numerical diagonalization at $\hbar_e = \sqrt{2E_R/V_0} = \sqrt{10}$ in Fig. 3.7 is well fitted with the tunneling picture by including tunneling to a total of twelve neighbors. The choice of parameters are the on-site energy $\epsilon_0 = 5.36021$, the nearest-neigbor tunneling parameter $-t = -1.75509$, the next-nearest-neighbor tunneling parameter $t_{nn} = -0.506245$ and the next-next-nearest-neighbor tunneling parameter $t_{nnn} = -0.339996$, all in units of V_0.

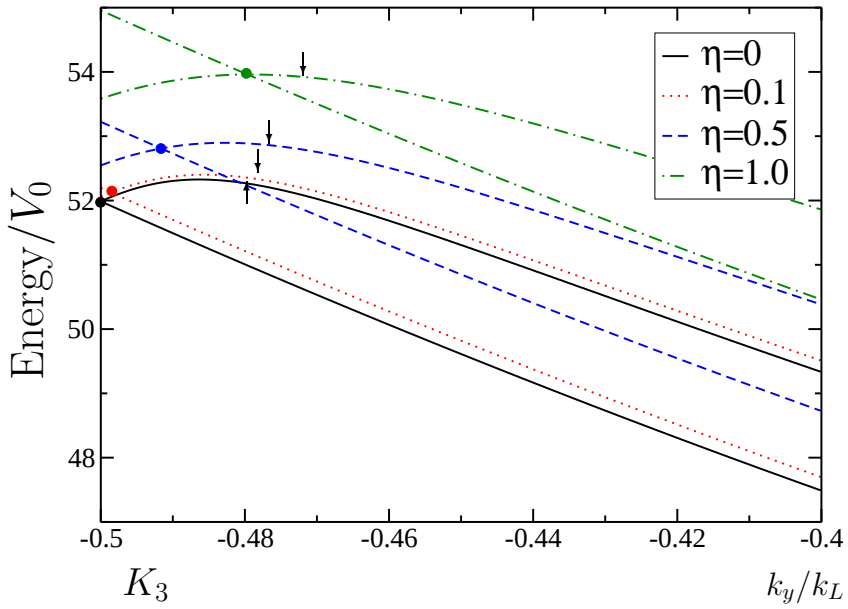

Figure 4.11: The energy dispersion along the straight line connecting point K_3 ($k_y/k_L = -0.5$) and K_2' ($k_y/k_L = 0.5$) in Fig. 4.3 for several imbalance intensity distortion parameters η at $\hbar_e = 10$. For each value of η, a solid circle (which has the same color as the curve) marks the point of intersection of the energy bands. The massless Dirac fermions vanish when the lower band intersects the upper band at the point where the upper band bends downwards (marked by the black arrow), hence giving a criteria of critical distortion parameters distinct from that of the tight-binding regime.

We shall now demonstrate the answers to the two questions by calculating the energy dispersion using the nearly-free electron model; see Eqs. (3.44), (3.45) and (3.46). We consider a point $\boldsymbol{k}$ that lies on the straight line connecting K_3 and K_2' in Fig. 4.3. The distortion being considered is the unbalanced laser intensity analyzed in Sec. 4.3.1. Choosing a total of twelve coefficients ($C_{\boldsymbol{0}}$, $C_{\pm\boldsymbol{b}_1}$, $C_{\pm\boldsymbol{b}_2}$, $C_{\pm(\boldsymbol{b}_1+\boldsymbol{b}_2)}$, $C_{\boldsymbol{b}_2-\boldsymbol{b}_1}$, $C_{-2\boldsymbol{b}_1}$, $C_{-2\boldsymbol{b}_1-\boldsymbol{b}_2}$, $C_{-\boldsymbol{b}_1-2\boldsymbol{b}_2}$ and $C_{-2\boldsymbol{b}_1-2\boldsymbol{b}_2}$) as basis, we construct a 12×12 matrix, with its eigenvalues giving the dispersion relation of the perturbed system. To check the accuracy of this method, a dispersion relation exactly the same as Fig. 3.7 is obtained for $-0.5 \leq k_y/k_L \leq 0$ at $\hbar_e = \sqrt{10}$ [1].

We numerically diagonalize the matrices at $\hbar_e = 10$ for different values of

[1] In Fig. 3.7, the energy dispersion is plotted along the line connecting K_2 and K_3'. By inversion, it is identical to the dispersion along the line connecting K_3 and K_2'.

distortion parameter η and find that, similar to the tight-binding regime, the Dirac points also move towards the center of the edge of 1BZ and merge as the honeycomb lattice is distorted; see Fig. 4.11. This observation has been explained in answering our first question. However, the dispersion relation is different from the tight-binding energy dispersion, the important difference being the downward bending of the upper branch for a small distance away from K_3. This has been shown as an effect of the next-nearest-neigbor tunneling (plus tunneling to farther neighbors of the same sublattice) in our analysis of second question. From the figure, the effect of distortion appears to be shifting the lower band upwards while shifting the upper band downwards. Consequently, the massless Dirac fermions will vanish when the lower band intersects the upper band at the point where the upper band bends downwards, hence giving a criteria of critical distortion parameters distinct from that of the tight-binding regime. Therefore, the picture of tunneling parameters forming a closed polygon only guarantees that the upper and the lower bands intersect at some points in the 1BZ, but it does not guarantee that the elementary excitations around these points of intersection to be described by the Weyl-Dirac Hamiltonian. Nevertheless, since the bending always exists at some distance from K_3 for arbitray weak optical potential, we can conclude that the massless Dirac fermions are robust to arbitrary small distortion at weak optical potential. In this sense, the existence of Dirac fermions appears to be a combined effect of symmetry of the perfect lattice and the tunneling picture.

4.5 Inequivalent potential wells

We briefly mention here how to distort the optical lattice in a systematic manner as it allows for an experimental control of the mass of the Dirac fermions as well as for a continuous switch from a honeycomb lattice to a triangular one [52, 53].

In Sec. 2.3.1, we observed that the honeycomb potential (3.7) is the simplest of all graphene-type potentials, characterized by choosing $V_{0,0}$ and $V_{1,0}$ real (in fact, positive) while putting all unrelated coefficients in Eq. (2.16) to zero. Now, letting $V_{1,0}$ to acquire a phase φ, such that $\mathrm{e}^{-\mathrm{i}\varphi}V_{1,0}$ is positive, will break the reflection symmetry of the honeycomb potential.

In the $\boldsymbol{r}$-dependent part of the dimensionless potential (3.9), this phase φ is introduced by the replacement

$$\sum_{a=1}^{3}\cos(\boldsymbol{b}_a\cdot\boldsymbol{r})\to\sum_{a=1}^{3}\cos(\boldsymbol{b}_a\cdot\boldsymbol{r}+\varphi)\,, \tag{4.12}$$

where $\boldsymbol{b}_3=-\boldsymbol{b}_1-\boldsymbol{b}_2$. This is implemented by the second alternative method suggested near the end of Sec. 3.2, that is by superimposing three *independent* standing waves, of the same wavelength and with equal intensity. As a consequence of the incoherent superposition, the time-shift of (3.6) is not available, and the $\boldsymbol{r}$ replacement alone cannot remove all three phases of the standing waves. One can, however, shift $\boldsymbol{r}$ such that the three phases are the same, and then one has an intensity pattern proportional to the right-hand side of (4.12).

Most of the hexagon structure of Fig. 3.3 remains unchanged by this modification: lattice sites A, B, C continue to be the locations of local minima and maxima, whereas the saddle points S acquire new positions on the ... ABCABC... lines.

Figure 4.12 confirms that, for small φ values, the minima of the honeycomb dipole potential are still organized in a hexagonal pattern but we now have *different* potential depths at sites A and B. The potential energy mismatch is $2\epsilon\approx 8V_0\big|\varphi\big|/\sqrt{3}$. In view of (2.28) and (2.31), this means that the Dirac fermions acquire a mass $m_*\propto\big|\varphi\big|$ or, in other words, that the Dirac degeneracies are lifted. The possibility of fine-tuning the mass of the Dirac fermions through the parameter φ is an interesting experimental knob to play with.

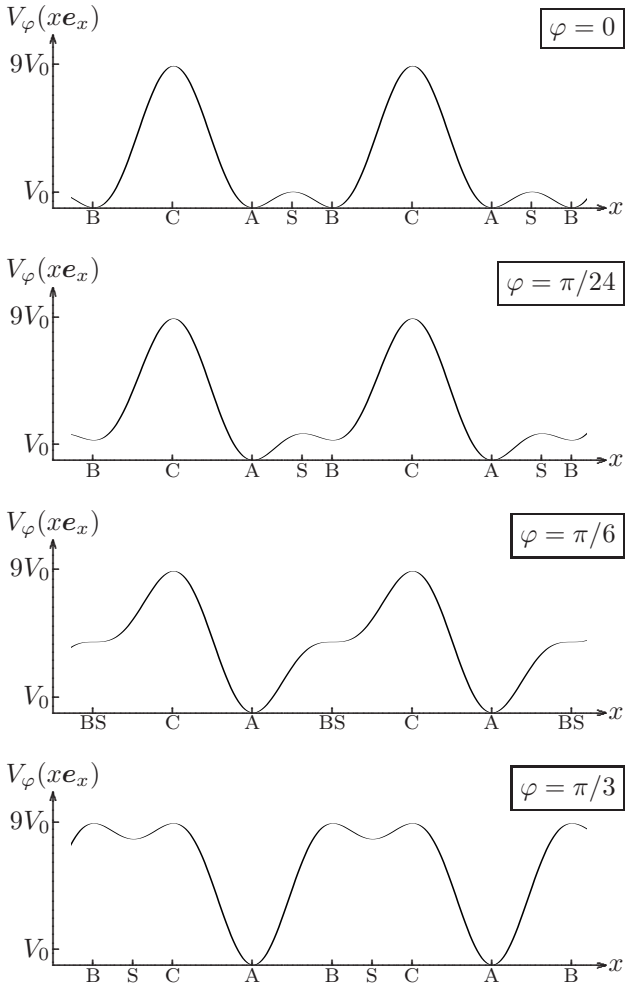

Figure 4.12: For various values of the phase parameter φ of (4.12), the plot shows the potential energy along a ... ABCABC... line in Fig. 3.3. The top plot, for $\varphi = 0$, repeats the bottom-left plot of Fig. 3.3 for reference. The degeneracy between sites A and B is lifted for the small φ value of $\varphi = \pi/24$, the saddle points have moved closer to the B sites, where we continue to have local minima. In this situation the Dirac fermions acquire a mass $m_* \propto |\varphi|$. When $\varphi = \pi/6$, the saddle points S coincide with the B sites, and we have cubic saddle points there. Finally, in the bottom plot, we have $\varphi = \pi/3$ and the saddle points are halfway between adjacent B and C sites, with potential maxima at both of them. Except for a displacement, the potential in the bottom plot is the negative of the potential in the top plot, and thus identical with the honeycomb potential (3.7) for red rather than blue detuning of the three running wave lasers. For ease of comparison, the potential constants are adjusted such that the maxima and minima are at $V = 0$ and $V = 9V_0$, respectively, for all φ values.

Increasing $|\varphi|$ further, one can also see that, for the particular values $|\varphi| = \pi/6$ and $\pi/2$, the three sublattices of saddle points merge into a single triangular lattice, which coincides with the A, B, or C lattice, respectively; see Fig. 4.12.

This merging of a potential minimum or maximum with three saddle points, leads to a peculiar third-order saddle point. For $\varphi = \pi/6$, say, the S sites merge with the B sites and we have

$$\sum_a \cos(\boldsymbol{b}_a \cdot \boldsymbol{r} + \varphi)\Big|_{\varphi=\pi/6} \approx -\frac{1}{6}\sum_a \big[\boldsymbol{b}_a \cdot (\boldsymbol{r} - \boldsymbol{r}_{\mathrm{B}})\big]^3 \tag{4.13}$$

for $\big|\boldsymbol{r} - \boldsymbol{r}_{\mathrm{B}}\big| \ll \kappa^{-1}$, hence a cubic saddle point rather than the usual quadratic saddle point.

An unpolarized ultracold gas of spin-$\frac{1}{2}$ fermions loaded into such a potential at half-filling would lead to two fermions per well. By driving the system through attractive interactions, one could even get a Mott insulator of fermion pairs. By switching off all interactions and setting $\varphi = 0$, one should be able to study oscillations of atoms between the A and B sublattices.

4.6 Other kinds of distortions

There are many other kinds of lattice distortions encountered in an actual experiment, e.g. the presence of a harmonic trap, the gaussian profile of laser beams and the jitter of optical lattice due to phase fluctuations. In the following, we shall give some specific references on the effects of the disorders and how they were circumvented by other researchers, but these references do not exhaust the possibilities.

- *Harmonic trap*: A harmonic trapping potential is needed to confine the atoms and to restrict the size of the atomic cloud, but this harmonic trap breaks the translation symmetry of the honeycomb optical lattice and it is no longer meaningful to discuss the energy band structure, which is a dispersion relation between single-particle energy and the crystal momentum. However,

Block and Nygaard show that a local density approximation can be used to understand the density of states of the harmonically-confined lattice system [92]. Furthermore, they show that the Dirac points do survive locally in the trap (demonstrated by plotting the density of states as a function of energy and distance from the trap center) and the Dirac points give rise to a unique spatial density profile for a non-interacting Fermi gas.

- *Gaussian beam profile*: In the calculations performed, we have assumed that the laser fields are described by plane waves. In real experiments, the cross-sections of the laser beams show a Gaussian intensity profile. Consequently, there is an energy offset between neighboring lattice wells and, when the sample size is much smaller than the beam waists, this energy offset can be approximated by a harmonic potential [73, 92]. Hence, we can apply the analysis done for a harmonic trap.

- *Phase fluctuations*: When the phase fluctuations of the laser beams are much slower than the typical time scale of the dynamics of the trapped atoms, the atoms will follow the lattice translation adiabatically. However, when the fluctuations are fast, the rapid jitter of the optical lattice could perturb the trapped atoms. To stabilize the relative phase difference between the laser beams, the use of a Michelson-type interferometer is reported in Ref. [93] and a phase stability better than 0.1° for as long as 30 ms was achieved.

4.7 Summary

We have analyzed the distorted honeycomb optical lattice and we have shown that in the tight-binding regime ($\hbar_e \ll 1$), the presence of Dirac fermions is determined by the geometrical relations of the three direction-dependent tunneling amplitudes. For small distortions, the Dirac points move around in the 1st BZ and they vanish

when distortion parameter exceeds a threshold value. Based on a semi-classical evaluation of t, we argued that Dirac fermions disappear when the perturbation due to the lattice distortion equals the energy level spacing of local harmonic oscillator. Our analysis is supported by the numerical data obtained from separate considerations of distortions due to imbalance laser intensities and mis-alignment of the laser beams. Our results show that the precision needed in experiments to observe massless Dirac fermions is achievable. Furthermore, we can easily tune the laser parameters across the transition so that we can ascertain if a physical phenomenon originates from massless Dirac fermions. In an attempt to understand the universal origin of massless Dirac fermions, we showed that massless Dirac fermions can exists in a distorted lattice with weak potential. However, the criteria of the critical distortion parameter is distinct from that in the tight-binding regime. We also proposed a laser configuration that breaks the equivalence between the two sublattices by changing a phase of the standing waves. This relative phase is not removable by a redifinition of spatial and temporal origin. The resulting quasi-particles are massive. In the last part of the chapter, we briefly examined other possible forms of distortion and outlined the solutions used by other researchers to circumvent the problem.

Chapter 5

Interacting system I: Model and methods

5.1 Feshbach resonance: tuning interactions between fermions

The recent advances in cold atom experiments enable us to simulate condensed matter phenomena using optical lattices. One of the notable achievements in cold atom experiments is the ability to tune the interaction strength between fermionic atoms using Feshbach resonances [81, 94]. The concept of Feshbach resonances was first proposed in nuclear physics in the context of reactions forming a compound nucleus [95]. The basic idea behind it can be illustrated using a two-channel model [31, 81]. Atoms are prepared in an open channel with a corresponding interaction potential $V_{\mathrm{op}}(\boldsymbol{r})$. As two atoms undergo a collision at low incident energy, the open channel is coupled to another closed channel with potential $V_{\mathrm{cl}}(\boldsymbol{r})$. When the magnetic moments of the colliding states in the open and close channel differ, we can tune the energy of a bound state in the close channel with respect to the open channel by the means of a magnetic field. A scattering resonance

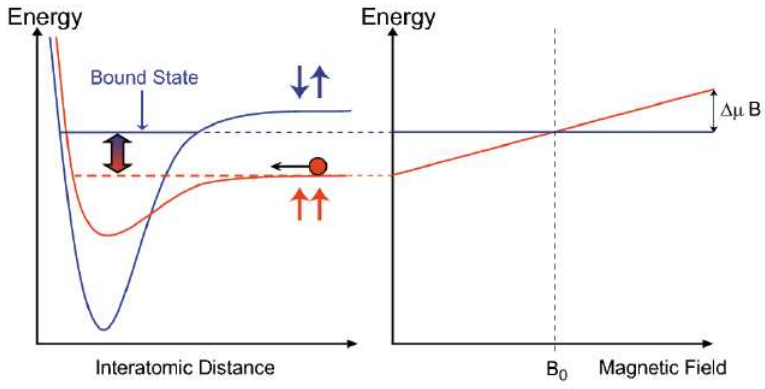

Figure 5.1: Atoms entering in the triplet state (open channel) are coupled to a singlet bound molecular state (closed channel). The bound state can be brought into resonance with the incoming state by changing the external magnetic field strength. The Feshbach resonance occurs at B_0 in the figure. Reprinted from Ref. [31], with kind permission of Società Italiana di Fisica.

occurs when the energy of the bound state is close to 0 such that it resonantly couples to the collision state in the open channel; see Fig. 5.1. The situation is similar to the Breit-Wigner problem where the resonance introduces an additional scattering phase shift. Since the scattering length is related to an effective s-wave interaction, we are able to change the effective interaction strength between the cold atoms simply by using an external uniform magnetic field. Besides magnetic field, Feshbach resonance induced optically using one- or two-photon transitions has been reported recently [96]. Also, when atoms are loaded into an optical lattice, we may simply tune the more relevant parameter, the ratio of the interaction strength over the tunneling amplitude, by changing the laser intensities, hence the lattice depth and the tunneling amplitude.

The van de Waals attraction between atoms gives rise to a centrifugal barrier in the effective potential for atoms in scattering states with non-zero angular momentum l in the relative motion. This barrier height, in terms of temperature, is of the order of 1 mK for typical atomic masses. Since experiments are usually carried out at temperature well below that, the $l \neq 0$ scattering states are frozen

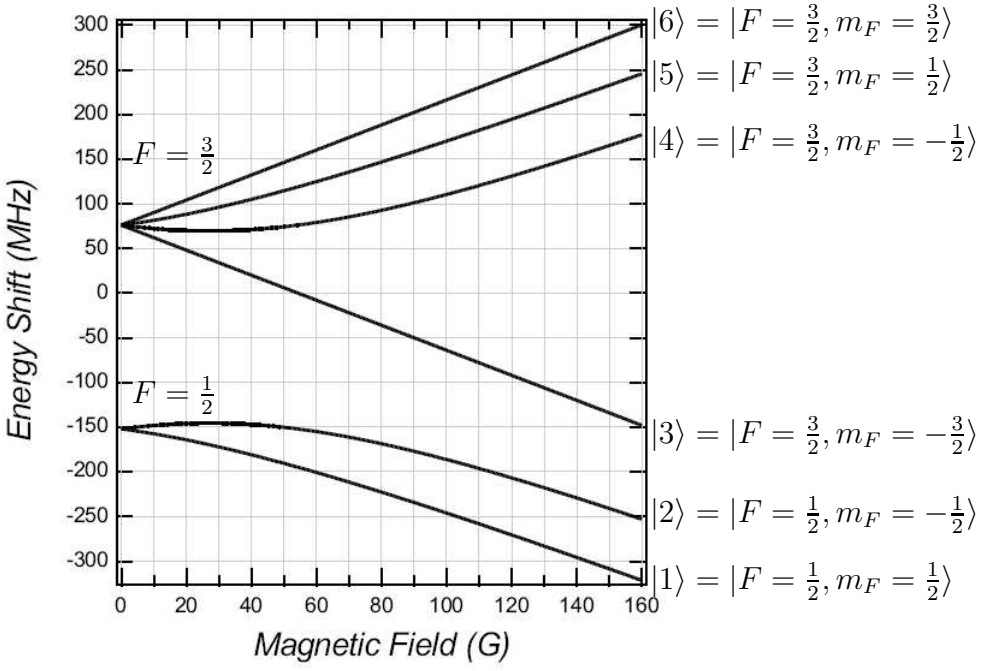

Figure 5.2: Magnetic-field dependence of $2^2S_{1/2}$ ground state of ^{6}Li. F is the quantum number for total atomic angular momentum and m_F is its value projected in the direction of magnetic field. At high field, the good quantum numbers are m_S and m_I, which are the projection of spin angular momentum and nuclear angular momentum, respectively. The labels $|1\rangle$–$|6\rangle$ are used in some literature, such as Ref. [97]. Possible candidates for simulation of Hubbard model are $|1\rangle$ and $|2\rangle$. For this choice, a Feshbach resonance is found at magnetic field near $B = 830G$ ($1G = 10^{-4}T$) [98]. There is an additional advantage that, at such a strong magnetic field, the hyperfine splittings might be neglected and the two fermionic species will experience the same optical dipole potential; see Sec. 3.1. Adapted from Ref. [86], which is licensed under the Creative Commons Attribution-NonCommercial-ShareAlike License (http://creativecommons.org/licenses/by-nc-sa/1.0).

out and the collision process is dominated by s-wave collisions if fermionic atoms of two different hyperfine states are used. In the tight-binding regime where atoms are localized in optical potential wells, the inter-atomic interactions are on-site, i.e. two fermionic atoms with different hyperfine states interact only if they are at the same lattice site. Denoting the two hyperfine states as spin-↑ and spin-↓, the physics of these effective spin-1/2 interacting fermions is encapsulated within the Hubbard model with on-site interactions [99, 100].

Potential candidates of the fermionic species are hyperfine states $|1\rangle = |F =$

$\frac{1}{2}, m_F = \frac{1}{2}\rangle$ and $|2\rangle = |F = \frac{1}{2}, m_F = -\frac{1}{2}\rangle$ of ^{6}Li; see Fig. 5.2. The choice has three advantages: (1) the scattering length is zero at zero external field so that we can change the system from interacting to non-interacting by simply turning off the magnetic field [86], (2) near the Feshbach resonance (at magnetic field $B \approx 830G$), the hyperfine energy is small compared to the Zeeman energy, hence the two fermionic species will experience the same optical dipole potential and (3) for the "broad" resonance involved, we can remove the closed channel molecular state from the picture by introducing an effective potential (e.g. an attractive spherical well or a regularized contact interaction) acting on the atoms in the open channel such that the physics is independent of the nature of the molecular state [31].

However, the chosen species are high-field seekers, hence they cannot be trapped in a magnetic trap. The problem can be solved either by trapping and cooling the atoms directly in an optical trap or magnetically trap and cool some other ^{6}Li atomic mixture, followed by transfering the mixture to an optical trap and finally convert the mixture to the required species using some methods [86].

A realization of Feshbach molecules using the ^{6}Li states ($|1\rangle$ and $|2\rangle$) has been decribed in both Refs. [23] and [101]. A gas of ^{6}Li atoms is first prepared in state $|1\rangle$ in a Nd-doped yttrium aluminium garnet (Nd-YAG) crossed beam optical dipole trap. Magnetic field is then increased from 5 to 1060 G, and a Zeeman transition between $|1\rangle$ and $|2\rangle$ is driven with a 76 MHz rf field to prepare a balanced mixture of the two states. The coherence between the two state is lost after 100 ms such that any single atom from the trap is described by either the state $|1\rangle$ or $|2\rangle$ but not a linear combination of them. At this magnitude of magnetic field strength, the good quantum numbers are the electronic spin angular momentum S and the total nuclear angular momentum I (the electronic orbital angular momentum $L = 0$) instead of the total angular momentum F. In this scenario, we have two atoms (one

from state $|1\rangle \approx |m_S = -\frac{1}{2}, m_I = 1\rangle$ and the other from $|2\rangle \approx |m_S = -\frac{1}{2}, m_I = 0\rangle$ [86]) colliding with parallel electronic spins, hence an electronic spin triplet, in the open channel; see Fig. 5.1. The differing nuclear spins will ensure that the Pauli exclusion principle is obeyed. Since the electronic spin singlet and triplet have a magnetic moment difference of $2\mu_B$ [102, 103], where μ_B is the Bohr magneton, a Feshbach resonance can be obtained by changing the energy of the colliding atoms in the open channel close to that of an electronic spin singlet bound state in the closed channel.

5.2 Hubbard model

In the following, we shall consider cold fermionic atoms loaded into a general honeycomb optical lattice in the tight-binding regime with on-site interactions between the fermions. The two sublattices are equivalent such that the non-interacting valence and conduction bands are not gapped. The second quantized grand-canonical Hamilton operator that describes this system thus reads

$$\begin{aligned} H &= H_K + H_V + H_\mu, \\ H_K &= -t \sum_{\langle \boldsymbol{i},\boldsymbol{j}\rangle,\sigma} \left(f^\dagger_{\boldsymbol{i}\sigma} f_{\boldsymbol{j}\sigma} + f^\dagger_{\boldsymbol{j}\sigma} f_{\boldsymbol{i}\sigma} \right), \\ H_V &= -U \sum_{\boldsymbol{i}} (n_{\boldsymbol{i}\uparrow} - 1/2)(n_{\boldsymbol{i}\downarrow} - 1/2), \\ H_\mu &= -\mu \sum_{\boldsymbol{i},\sigma} n_{\boldsymbol{i}\sigma}, \end{aligned} \tag{5.1}$$

where $\langle \boldsymbol{i}, \boldsymbol{j} \rangle$ denotes pairs of nearest neighbors on the lattice, $\sigma = \uparrow, \downarrow$ denotes the two possible spin states of the fermions, $f^\dagger_{\boldsymbol{i}\sigma}$ and $f_{\boldsymbol{i}\sigma}$ are the creation and annihilation operators of a fermion with spin state σ at site $\boldsymbol{i}$ and $n_{\boldsymbol{i}\sigma} = f^\dagger_{\boldsymbol{i}\sigma} f_{\boldsymbol{i}\sigma}$ is the corresponding number operator. H_K is the same as Eq. (2.32), which describes the hopping process between nearest neighbors, except that we have specialized

into an ideal honeycomb lattice with equal hopping amplitudes in all directions, $t = \left|t_{\boldsymbol{ij}}\right|$. H_V describes the on-site interaction, where $U > 0$ when the interaction is attractive while $U < 0$ when interaction is repulsive. In subsequent analysis, we will be mostly dealing with the fermionic attractive Hubbard model (FAHM) as we focus on BCS-BEC crossover on a honeycomb lattice. Lastly, μ is the chemical potential whose value fixes the average total fermionic density

$$\rho = \frac{1}{2N_c}\sum_{\boldsymbol{i},\sigma}\langle n_{\boldsymbol{i}\sigma}\rangle.$$

It is defined such that $\mu = 0$ corresponds to a half-filled lattice, i.e. $\rho = 1$, for all interaction strength U.

In general, the eigenvalue problem for the Hamilton operator (5.1) is difficult to solve analytically due to the presence of quartic terms in H_V. Hence, we often have to resort to mean-field approximations or to quantum Monte Carlo (QMC) method to solve it numerically. In the following, we will explain briefly determinant quantum Monte Carlo (DQMC) algorithm that is used in our study and the maximum entropy method (MaxEnt) that is used to extract frequency-dependent information through analytic continuation of the imaginary-time data from DQMC. Since the content is technical in nature, readers may instead proceed to the next chapter for analysis on DQMC data and the Hubbard model.

5.3 Numerical methods

5.3.1 Determinant quantum Monte Carlo (DQMC)

Probability density function

To calculate the equilibrium property of the system at finite but low temperature, we first look at its grand partition function,

$$\mathcal{Z} = \mathrm{Tr}(\mathrm{e}^{-\beta H}), \tag{5.2}$$

where $\beta = 1/(k_B T)$ is the inverse temperature and Tr is the sum over all number of particles and over all site occupations. The trace could be evaluated by breaking the exponential into a product of three pieces using the Suzuki-Trotter decomposition, which says that

$$e^{-\Delta\tau(A+B)} = e^{-\Delta\tau A} e^{-\Delta\tau B} + \mathcal{O}(\Delta\tau^2) \tag{5.3}$$

for small $\Delta\tau$, hence

$$\begin{aligned}
\mathcal{Z} &= \mathrm{Tr}\left(e^{-\beta H}\right) \\
&= \mathrm{Tr}\left(\prod_{l=1}^{M} e^{-\Delta\tau H_l}\right) \\
&= \mathrm{Tr}\left(\prod_{l=1}^{M} (e^{-\Delta\tau H_{K,l}} e^{-\Delta\tau H_{V,l}} e^{-\Delta\tau H_{\mu,l}})\right) + \mathcal{O}(\Delta\tau^2),
\end{aligned} \tag{5.4}$$

where we have decomposed the partition function into contributions from M time slices, $H = \sum_{l=1}^{M} H_l = \sum_{l=1}^{M} (H_{K,l} + H_{V,l} + H_{\mu,l})$ and $\beta = M\Delta\tau$. It is to be noted[1] here that the Trotter index l in H_l actually goes with the states of H_l, hence the matrix elements of $e^{-\Delta H_l}$, while the second-quantized form of H_l is just identical

[1] I want to thank Professor Wang Jiansheng for pointing this out to me.

to H. Hence, the index l is there just for us to keep track of the index of the matrix element of H, but not to H itself. We have also set $\hbar = 1$ for convenience. For our purpose, a sufficiently small value of $\Delta\tau$ is $0.125/t$.

The quartic terms in $e^{-\Delta\tau H_{V,l}}$ can be written as a bilinear form using the discrete Hubbard-Stratonovich (HS) transformation [104]. Since we are dealing with attractive interactions ($U \geq 0$), the HS transformation is carried out by coupling the auxiliary HS field $h_{\boldsymbol{i}l}$ to the total number of fermions, $n_{\boldsymbol{i}\uparrow l} + n_{\boldsymbol{i}\downarrow l}$ at the site $\boldsymbol{i}$ and time slice l,

$$e^{U\Delta\tau(n_{\boldsymbol{i}\uparrow l}-\frac{1}{2})(n_{\boldsymbol{i}\downarrow l}-\frac{1}{2})} = \frac{1}{2}e^{-\frac{U\Delta\tau}{4}} \sum_{h_{\boldsymbol{i}l}=\pm 1} e^{\lambda h_{\boldsymbol{i}l}(n_{\boldsymbol{i}\uparrow l}+n_{\boldsymbol{i}\downarrow l}-1)} \text{ with } \cosh\lambda = e^{\frac{U\Delta\tau}{2}}. \quad (5.5)$$

We now rewrite the grand-canonical partition function into a form with only bilinear terms in the exponential,

$$\mathcal{Z} = \left(\frac{1}{2}e^{-\frac{U\Delta\tau}{4}}\right)^{MN} \mathrm{Tr}_h e^{-\lambda\sum_{\boldsymbol{i},l} h_{\boldsymbol{i}l}} \mathrm{Tr}\left(\prod_{l=1}^{M}\prod_{\sigma=\uparrow,\downarrow}(e^{-\Delta\tau\sum_{\boldsymbol{ij}} f^{\dagger}_{\boldsymbol{i}\sigma}K_{\boldsymbol{ij}}f_{\boldsymbol{j}\sigma}} e^{\sum_{\boldsymbol{i}} f^{\dagger}_{\boldsymbol{i}\sigma}V^{\sigma}_{\boldsymbol{i}l}f_{\boldsymbol{i}\sigma}})\right), \quad (5.6)$$

where $V^{\sigma}_{\boldsymbol{i}l} = \lambda h_{\boldsymbol{i}l} + \mu\Delta\tau$, $K_{\boldsymbol{ij}} = -\left|t_{\boldsymbol{ij}}\right|$ if site $\boldsymbol{i}$ and site $\boldsymbol{j}$ are nearest neighbours, N is the total number of lattice sites and Tr_h denotes the sum over all possible HS field configurations.

With the exponents in bilinear form, the fermionic operators could be traced out to give [37, 105]

$$\begin{aligned}\mathcal{Z} &= \left(\frac{1}{2}e^{-\frac{U\Delta\tau}{4}}\right)^{MN} \mathrm{Tr}_h e^{-\lambda\sum_{\boldsymbol{i},l} h_{\boldsymbol{i}l}} \prod_{\sigma} \det[\mathbb{1} + B^{\sigma}_{M}B^{\sigma}_{M-1}\ldots B^{\sigma}_{1}] \\ &= \left(\frac{1}{2}e^{-\frac{U\Delta\tau}{4}}\right)^{MN} \mathrm{Tr}_h \rho(h) \\ &= \left(\frac{1}{2}e^{-\frac{U\Delta\tau}{4}}\right)^{MN} \mathcal{Z}_{\text{eff}}, \end{aligned} \quad (5.7)$$

where $B_l^\sigma \equiv e^{-\tau K} e^{V_l^\sigma}$ and the effective probability distribution function (PDF)[2] $\rho(h) = \rho_\uparrow(h) \times \rho_\downarrow(h)$ is a product of the spin-$\uparrow$ and spin-$\downarrow$ components, with the spin-σ component proportional to $\det[\mathbb{1} + B_M^\sigma(h) B_{M-1}^\sigma(h) \dots B_1^\sigma(h)]$. We can thus interpret $\mathcal{Z}_{\text{eff}}$ as the effective grand-canonical partition function.

For each data point (temperature, interaction strength, lattice and density), 20 simulations of different random seeds are performed, each with 1000 to 2000 warm-up sweeps and 2000 measurement sweeps[3]. The statistical average of the 20 simulations is then reported. In a typical simulation, a random HS field configuration is first generated. In each sweep itself, the Metropolis algorithm is used to perform local moves to flip the HS variable at a given site and a given imaginary time. The updating of the HS variables involve fast rank-one updates that are discussed in greater details in Refs. [105] and [107]

Measurement: Correlation functions

From Eq. (5.4), we see that the Hamilton operator has acquired a new label, the imaginary time $\tau = l \times \Delta\tau$. With it, we can introduce a convenient mathematical tool called the Matsubara Green's function, which is a time-ordered product not along the real time but along the imaginary time axis. It is especially useful for time-dependent correlation function because the analytical continuation to the physically relevant retarded function in frequency space is just trivial. In general, we define the imaginary time evolution of an operator $\mathcal{O}$ by

$$\mathcal{O}(\tau) = \mathrm{e}^{(\tau - \tau')H}\, \mathcal{O}(\tau')\, \mathrm{e}^{-(\tau - \tau')H}. \tag{5.8}$$

[2]Since the determinants could be negative, the correct PDF is $\big|\rho(h)\big|$. However, because the two determinants have the same sign in our study, $\big|\rho(h)\big| = \rho(h)$. The minus sign problem is thus avoided [106].

[3]A sweep literally means sweeping through each site in a lattice once. The lattice has a spatial dimension of two and a temporal dimension of one.

The correspondence of the above equation to the real time evolution can be done by the substitution $\tau = \mathrm{i}t$, where t is a complex time.

Numerical data that could be obtained from DQMC are correlation functions. They are divided into equal-'time' and unequal-'time' correlation functions, with the most important of all being the single-particle Green's functions. Given two operators $\mathcal{O}_1$ and $\mathcal{O}_2$, their equal-'time' correlation function is

$$\langle \mathcal{O}_1 \mathcal{O}_2 \rangle = \frac{1}{\mathcal{Z}} \mathrm{Tr} \left(\mathcal{O}_1 \mathcal{O}_2 \, \mathrm{e}^{-\beta H} \right) = \frac{1}{\mathcal{Z}_{\mathrm{eff}}} \mathrm{Tr}_h \Big(\langle \mathcal{O}_1 \mathcal{O}_2 \rangle_h \, \rho(h) \Big), \tag{5.9}$$

where we have defined the average of $\mathcal{O}_1 \mathcal{O}_2$ over a given HS field configuration $\{h_{il}\}$ as

$$\langle \mathcal{O}_1 \mathcal{O}_2 \rangle_h \equiv \frac{e^{-\lambda \sum_{i,l} h_{il}}}{\rho(h)} \mathrm{Tr} \left(\mathcal{O}_1 \mathcal{O}_2 \prod_{l,\sigma} (e^{-\Delta\tau \sum_{ij} f^\dagger_{i\sigma} K_{ij} f_{j\sigma}} e^{\sum_i f^\dagger_{i\sigma} V^\sigma_{il} f_{i\sigma}}) \right) \tag{5.10}$$

and $\langle \cdot \rangle$ denotes the quantum statistical average at temperature T.

The important equal-'time' single-particle Green's functions of the l-time slice can thus be obtained as the elements of an $N \times N$ matrix,

$$\begin{aligned} \langle f_{i\sigma}(l) f^\dagger_{j\sigma}(l) \rangle_h &= [\mathrm{g}^\sigma_l]_{ij}, \\ \mathrm{g}^\sigma_l &= (\mathbb{1} + B^\sigma_{l-1} B^\sigma_{l-2} \ldots B^\sigma_1 B^\sigma_M \ldots B^\sigma_l)^{-1}. \end{aligned} \tag{5.11}$$

On the other hand, obtaining unequal-'time' single-particle Green's functions is computationally more expensive as it involves inverting matrices of dimensions $(Np) \times (Np)$, where p is an integer in the range $1 \leq p \leq M$ [108]. Again, the Green's functions could be expressed as the elements of some $N \times N$ matrices,

$$\begin{aligned} \langle f_{i\sigma}(l_1) f^\dagger_{j\sigma}(l_2) \rangle_h &= [B^\sigma_{l_1} B^\sigma_{l_1-1} \ldots B^\sigma_{l_2+1} \mathrm{g}^\sigma_{l_2+1}]_{ij}, \; l_1 > l_2, \\ \langle f^\dagger_{i\sigma}(l_1) f_{j\sigma}(l_2) \rangle_h &= [(\mathbb{1} - \mathrm{g}^\sigma_{l_2+1})(B^\sigma_{l_1} B^\sigma_{l_1-1} \ldots B^\sigma_{l_2+1})^{-1}]_{ij}, \; l_1 > l_2. \end{aligned} \tag{5.12}$$

Having computed the equal- and unequal-'time' Green's functions for a fixed HS configuration, we can calculate all correlation functions in terms of the single-particle Green's functions using Wick's theorem. Indeed, it can be shown by expanding in eigenstates that Wicks' theorem holds for a *fixed HS configuration*[4] [37, 109],

$$\langle f^\dagger_{\boldsymbol{i}_1}(l_1) f_{\boldsymbol{i}_2}(l_2) f^\dagger_{\boldsymbol{i}_3}(l_3) f_{\boldsymbol{i}_4}(l_4)\rangle_h = \langle f^\dagger_{\boldsymbol{i}_1}(l_1) f_{\boldsymbol{i}_2}(l_2)\rangle_h \langle f^\dagger_{\boldsymbol{i}_3}(l_3) f_{\boldsymbol{i}_4}(l_4)\rangle_h + \langle f^\dagger_{\boldsymbol{i}_1}(l_1) f_{\boldsymbol{i}_4}(l_4)\rangle_h \langle f_{\boldsymbol{i}_2}(l_2) f^\dagger_{\boldsymbol{i}_3}(l_3)\rangle_h. \quad (5.13)$$

The spin indices have been omitted in Eq. (5.13) since the spin-↑ and spin-↓ channels can be easily factorized.

Anticipating discussions on the BCS-BEC crossover in the next chapter, we briefly mention here some of the physical quantities or correlation functions measured in our DQMC simulations.

- **Density-density correlation**:

  The presence of a density wave is signaled by the spatial modulation in the density-density correlation function,

  $$D_{\boldsymbol{ij}} = \langle n_{\boldsymbol{i}} n_{\boldsymbol{j}}\rangle, \quad (5.14)$$

  where $n_{\boldsymbol{i}} = \sum_\sigma n_{\boldsymbol{i}\sigma}$ measures the total number of fermions on site $\boldsymbol{i}$. We define the density wave structure factors of the uniform sector $S^u_{\mathrm{dw}}(\boldsymbol{q})$ and the staggered sector $S^s_{\mathrm{dw}}(\boldsymbol{q})$ in terms of the density-density correlations for

[4] Given a fixed HS configuration, the effective Hamilton operator becomes quadratic and Wick's theorem thus holds.

$\boldsymbol{q} \in \Omega$,

$$S^{u}_{\mathrm{dw}}(\boldsymbol{q}) = \frac{1}{N}\sum_{\boldsymbol{i},\boldsymbol{j}} \mathrm{e}^{\mathrm{i}\boldsymbol{q}\cdot(\boldsymbol{r_i}-\boldsymbol{r_j})}\, D_{\boldsymbol{ij}}, \tag{5.15}$$
$$S^{s}_{\mathrm{dw}}(\boldsymbol{q}) = \frac{1}{N}\sum_{\boldsymbol{i},\boldsymbol{j}} \mathrm{e}^{\mathrm{i}\boldsymbol{q}\cdot(\boldsymbol{r_i}-\boldsymbol{r_j})}(-1)^{\boldsymbol{i}+\boldsymbol{j}}\, D_{\boldsymbol{ij}},$$

with the site index $\boldsymbol{i}$ being even on A sites and odd on B sites while $\boldsymbol{r}_i$ is the position vector of the center of the primitive unit cell that the site $\boldsymbol{i}$ belongs to. We will focus on the structure factor from the staggered sector that varies uniformly over unit cells, $S_{\mathrm{dw}} = S^{s}_{\mathrm{dw}}(\boldsymbol{q} = \boldsymbol{0})$. It will diverge linearly with the total number of sites $N = 2N_c$ of the system when the fermions tend to accumulate at one sublattice at an instant.

- **Pair Green's functions**:

  In a Bose condensed phase, the phase coherence between pairs is signaled by long-range order (or quasi-long-range order for a superfluid at finite temperature) in the pair Green's function,

$$G^{\mathrm{p}}_{\boldsymbol{ij}} = \frac{1}{2}\langle \Delta^{\dagger}_{\boldsymbol{i}}\Delta_{\boldsymbol{j}} + \Delta_{\boldsymbol{i}}\Delta^{\dagger}_{\boldsymbol{j}}\rangle, \tag{5.16}$$

  where $\Delta^{\dagger}_{\boldsymbol{i}} = f^{\dagger}_{\boldsymbol{i}\uparrow} f^{\dagger}_{\boldsymbol{i}\downarrow}$ creates a pair on site i. In a way similar to the density correlations, we define a pair structure factor in the uniform sector $P^{\mathrm{u}}(\boldsymbol{q})$ and the staggered sector $P^{\mathrm{s}}(\boldsymbol{q})$ for $\boldsymbol{q} \in \Omega$,

$$P^{\mathrm{u}}(\boldsymbol{q}) = \frac{1}{N}\sum_{\boldsymbol{i},\boldsymbol{j}} \mathrm{e}^{\mathrm{i}\boldsymbol{q}\cdot(\boldsymbol{r_i}-\boldsymbol{r_j})}\, G^{\mathrm{p}}_{\boldsymbol{ij}}, \tag{5.17}$$
$$P^{\mathrm{s}}(\boldsymbol{q}) = \frac{1}{N}\sum_{\boldsymbol{i},\boldsymbol{j}} \mathrm{e}^{\mathrm{i}\boldsymbol{q}\cdot(\boldsymbol{r_i}-\boldsymbol{r_j})}(-1)^{\boldsymbol{i}+\boldsymbol{j}}\, G^{\mathrm{p}}_{\boldsymbol{ij}}.$$

  In particular, we focus on the s-wave pair structure factor $P_{\mathrm{s}} = P^{\mathrm{u}}(\boldsymbol{q} = 0)$. [5]

[5] The s index indicates the symmetry of the wave function, by analogy with the notation of

This pair structure factor diverges linearly with N when long-range order is achieved.

- **Time-displaced on-site Green's function**:

  We calculate the (imaginary) time-displaced on-site Green's function[6] (per spin component)

$$G(\tau) = \frac{1}{2N}\sum_{\boldsymbol{i},\sigma}\Big(\langle f_{\boldsymbol{i}\sigma}(\tau) f^{\dagger}_{\boldsymbol{i}\sigma}(0)\rangle\theta(\tau-\eta) - \langle f^{\dagger}_{\boldsymbol{i}\sigma}(0) f_{\boldsymbol{i}\sigma}(\tau)\rangle\theta(-\tau+\eta)\Big)\Big|_{\eta\to 0^{+}} \tag{5.18}$$

  for $-\beta \leq \tau \leq \beta$ so as to extract the spectral function $A(\omega)$ through a maximum entropy approach described in the next section. Here, $\theta(\tau)$ is the Heavisde step function,

$$\theta(\tau) = \begin{cases} 1, & \tau \geq 0 \\ 0, & \tau < 0 \end{cases} \tag{5.19}$$

  and the presence of infinitesimal η reminds us that the second term contributes at equal times. A more general definition of the Green's function is the position-depedent form given by

$$G_{\boldsymbol{ij}}(\tau) = \frac{1}{2}\sum_{\sigma}\Big(\langle f_{\boldsymbol{i}\sigma}(\tau) f^{\dagger}_{\boldsymbol{j}\sigma}(0)\rangle\theta(\tau-\eta) - \langle f^{\dagger}_{\boldsymbol{j}\sigma}(0) f_{\boldsymbol{i}\sigma}(\tau)\rangle\theta(-\tau+\eta)\Big)\Big|_{\eta\to 0^{+}}. \tag{5.20}$$

  Due to the translational invariance of the system, we can Fourier transform $G_{\boldsymbol{ij}}(\tau)$ to obtain

$$G(\boldsymbol{k},\tau) = \frac{1}{N^2}\sum_{\boldsymbol{i},\boldsymbol{j}} \mathrm{e}^{\mathrm{i}\boldsymbol{k}\cdot(\boldsymbol{r_j}-\boldsymbol{r_i})} G_{\boldsymbol{ij}}(\tau), \tag{5.21}$$

the hydrogen orbitals. Here, the on-site pair is invariant by rotation.

[6] Interested readers are strongly encouraged to read Refs. [110] and [111] for a much more detailed discussion on Green's function and its analytical properties. The information is too much to be contained in one or two pages that what is presented here is simply a rough outline.

which contains information on the system in the momentum space. However, we did not compute this more general quantity because of the much longer computational time involved.

By its definition, the Green's function $G(\tau)$ is antiperiodic under shifts of β, i.e.

$$G(\tau - \beta) = -G(\tau) \quad \text{for} \quad 0 \leq \tau \leq \beta, \tag{5.22}$$

hence we can Fourier transform it to obtain its representation at the Matsubara frequencies $\omega_n = \frac{(2n+1)\pi}{\beta}$,

$$\mathcal{G}(\mathrm{i}\omega_n) = \int_0^\beta d\tau \; G(\tau) \; \mathrm{e}^{\mathrm{i}\omega_n \tau}, \tag{5.23}$$

and the corresponding inverse function

$$G(\tau) = \frac{1}{\beta} \sum_{\mathrm{i}\omega_n} \mathcal{G}(\mathrm{i}\omega_n) \; \mathrm{e}^{-\mathrm{i}\omega_n \tau}. \tag{5.24}$$

If we now restrict the range of τ to $0 \leq \tau \leq \beta$ and insert a complete set of eigenstates of H in between $f_{\boldsymbol{i}\sigma}(\tau)$ and $f^\dagger_{\boldsymbol{i}\sigma}(0)$, we obtain $G(\tau)$ as

$$G(\tau) = \frac{1}{2N} \sum_{\boldsymbol{i},\sigma} \frac{1}{\mathcal{Z}} \sum_{m,j} \mathrm{e}^{-\beta E_j} \mathrm{e}^{-\tau(E_m - E_j)} |\langle m | f^\dagger_{\boldsymbol{i}\sigma} | j \rangle|^2 \tag{5.25}$$

and $\mathcal{G}(\mathrm{i}\omega_n)$ as

$$\mathcal{G}(\mathrm{i}\omega_n) = \frac{-1}{2N} \sum_{\boldsymbol{i},\sigma} \frac{1}{\mathcal{Z}} \sum_{m,j} \frac{\mathrm{e}^{-\beta E_m} + \mathrm{e}^{-\beta E_j}}{\mathrm{i}\omega_n - (E_m - E_j)} |\langle m | f^\dagger_{\boldsymbol{i}\sigma} | j \rangle|^2, \tag{5.26}$$

where E_m is the eigenvalue of H and $|m\rangle$ is the corresponding normalized eigenstate. In fact, $-\mathcal{G}(\mathrm{i}\omega_n)$ is described by the same function on the complex frequency plane as the retarded (advanced) Green's function at frequencies

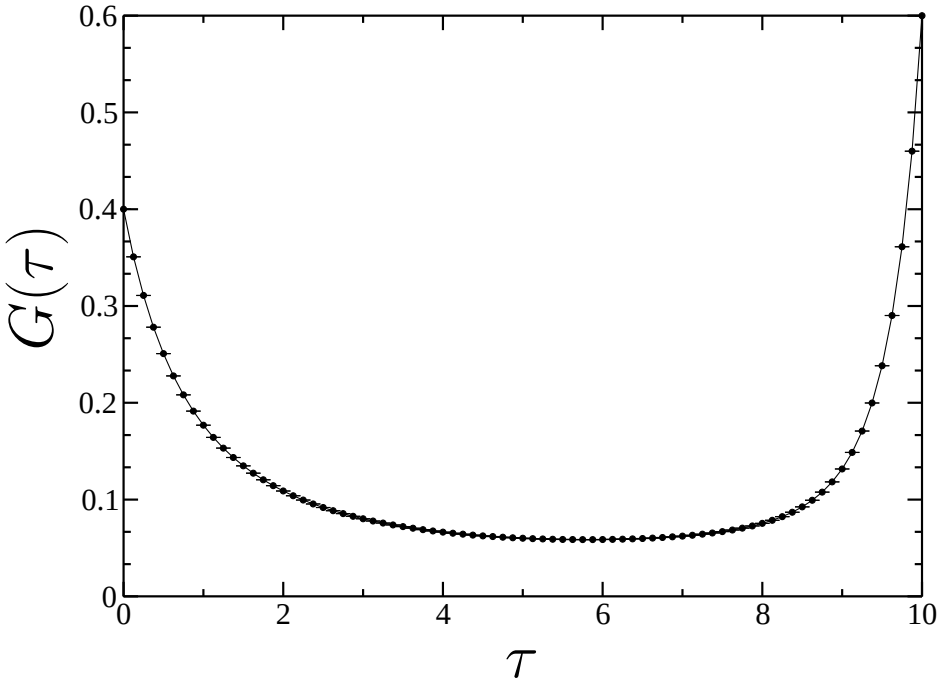

Figure 5.3: A typical Green's function $G(\tau)$ obtained in a DQMC simulation. The parameters chosen are lattice linear size $L = 9$, density $\rho = 1.2$, interaction strength $U = 2t$ and inverse temperature $\beta = 10/t$. Note that $G(\tau) \to 1 - 0.5\rho$ as $\tau \to 0^+$ and $G(\tau) \to 0.5\rho$ as $\tau \to \beta^-$.

infinitesimally above (below) the real axis, such that the retarded (advanced) Green's function can be obtained from $-\mathcal{G}(\mathrm{i}\omega_n)$ through analytic continuation, $\mathrm{i}\omega_n \to \omega + \mathrm{i}\eta$ ($\mathrm{i}\omega_n \to \omega - \mathrm{i}\eta$). Let us now rewrite $-\mathcal{G}(\mathrm{i}\omega_n)$ as

$$-\mathcal{G}(\mathrm{i}\omega_n) = \int_{-\infty}^{\infty} d\omega' \frac{A(\omega')}{\mathrm{i}\omega_n - \omega'}, \tag{5.27}$$

where the spectral function is given by

$$A(\omega) = \frac{1}{2N} \sum_{\boldsymbol{i},\sigma} \frac{1}{\mathcal{Z}} \sum_{m,j} \delta\big(\omega - (E_m - E_j)\big) \big|\langle m| f^{\dagger}_{\boldsymbol{i}\sigma} |j\rangle\big|^2 (\mathrm{e}^{-\beta E_m} + \mathrm{e}^{-\beta E_j}). \tag{5.28}$$

If we have used $G(\boldsymbol{k}, \tau)$ instead of $G(\tau)$ in Eqs. (5.22) to (5.27), we can then extract the momentum-dependent spectral function $A(\boldsymbol{k}, \omega)$, which can be measured directly in the angle-resolved photo-emission experiments, and $A(\omega) = \sum_{\boldsymbol{k}} A(\boldsymbol{k}, \omega)$. Clearly, $-\mathcal{G}(\omega)$ (with ω now takes on complex values)

has simple poles on the real line of ω with the weights of the poles given by the spectral function. In the limit of zero temperature, the spectral function is reduced to the form

$$A(\omega) = \frac{1}{2N} \sum_{\boldsymbol{i},\sigma,m} \delta\big(\omega-(E_m-E_0)\big)\left|\langle m|f^\dagger_{\boldsymbol{i}\sigma}|0\rangle\right|^2+\delta\big(\omega+(E_m-E_0)\big)\left|\langle 0|f^\dagger_{\boldsymbol{i}\sigma}|m\rangle\right|^2, \tag{5.29}$$

where $|0\rangle$ is the non-degenerate ground state[7]. The first term measures particle excitations while the second term measures hole excitations. Thus, the spectral function essentially reflects the one-particle excitation spectrum, hence it enables us to distinguish between metallic, semi-metallic or gapped (solid or superfluid) states of the system. In the non-interacting limit, $|0\rangle$ is the state of the Fermi sea and $f^\dagger_{\boldsymbol{i}\sigma}$ ($f_{\boldsymbol{i}\sigma}$) only connects the ground state to the excitated states with one more particle (hole) added above (below) the Fermi sea. As a result, $\sum_{\boldsymbol{i}}\left|\langle 0|f^\dagger_{\boldsymbol{i}\sigma}|m\rangle\right|^2 = 1$ for the excited states described and $E_m - E_0$ is reduced to the eigenenergies of the single-particle Hamilton operator. A comparison between Eqs. (5.29) and (2.42) reveals that $A(\omega)$ is reduced to the density of states (with a factor of one half that comes from defining $A(\omega)$ as per site while defining $\rho(\omega)$ as per unit cell).

5.3.2 Maximum entropy method (MaxEnt)

We have explained in Sec. 5.3.1 that DQMC simulations can provide us imaginary-time-dependent correlation functions $G(\tau)$, from which we may extract the dynamical spectra $A(\omega)$. The relation between $G(\tau)$ and $A(\omega)$ can be obtained by substituting Eq. (5.27) into Eq. (5.24),

$$G(\tau) = \int_{-\infty}^{\infty} d\omega'\ A(\omega') \left(\frac{-1}{\beta} \sum_{\mathrm{i}\omega_n} \frac{\mathrm{e}^{-\mathrm{i}\omega_n\tau}}{\mathrm{i}\omega_n - \omega'} \right), \tag{5.30}$$

[7] We can easily generalize the expression to degenerate ground states.

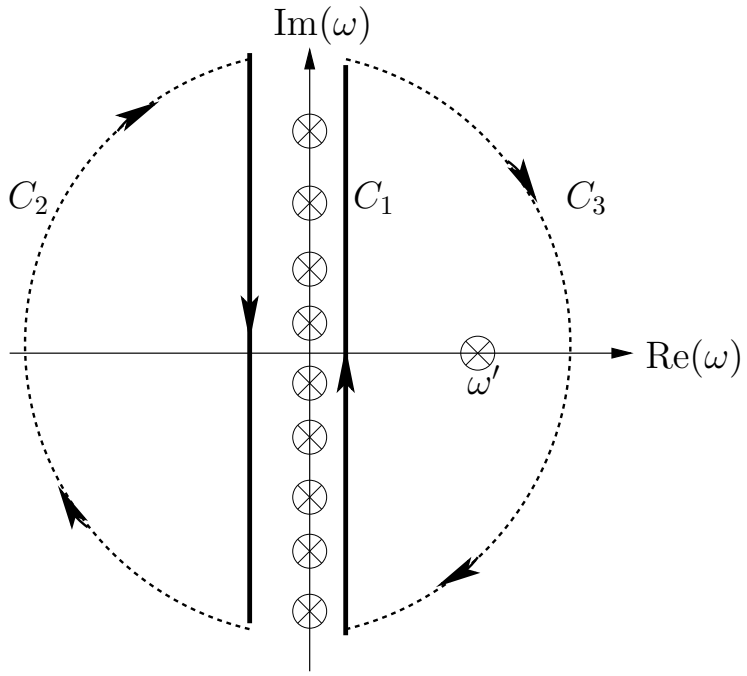

Figure 5.4: The contour in the complex ω-plane that is used to obtain the relation between $G(\tau)$ and $A(\omega)$. The crosses on the imaginary axis denote the Matsubara frequencies.

and perform the sum over Matsubara frequencies using contour integration in the complex ω-plane. We first note that the function $\beta/(1+\mathrm{e}^{-\beta\omega})$ has poles at the Matsubara frequencies, $\omega = \mathrm{i}\omega_n$, with unity residues. Applying the Cauchy's residue theorem, we can see that

$$\frac{-1}{\beta}\sum_{\mathrm{i}\omega_n}\frac{\mathrm{e}^{-\mathrm{i}\omega_n\tau}}{\mathrm{i}\omega_n-\omega'} = \frac{-1}{2\pi\mathrm{i}}\int_{C_1} d\omega\ \frac{1}{\beta}\frac{\mathrm{e}^{-\omega\tau}}{\omega-\omega'}\frac{\beta}{1+\mathrm{e}^{-\beta\omega}}, \tag{5.31}$$

where the contour C_1 (solid line) is defined in Fig. 5.4. We can add the two semi-circles with a very large radius (dotted lines), C_2 and C_3, to the contour of evaluation without changing the result. This is because, at $|\mathrm{Re}(\omega)| \gg 1$, the factor $\frac{\mathrm{e}^{\tau|\mathrm{Re}(\omega)|}}{1+\mathrm{e}^{\beta|\mathrm{Re}(\omega)|}} \approx \mathrm{e}^{(\tau-\beta)|\mathrm{Re}(\omega)|}$ ensures that C_2 makes no contribution to the integration while $\mathrm{e}^{-\tau|\mathrm{Re}(\omega)|}$ plays the same role for C_3. We now have

$$\frac{-1}{\beta}\sum_{\mathrm{i}\omega_n}\frac{\mathrm{e}^{-\mathrm{i}\omega_n\tau}}{\mathrm{i}\omega_n-\omega'} = \frac{-1}{2\pi\mathrm{i}}\int_{C_1+C_2+C_3} d\omega\ \frac{1}{\beta}\frac{\mathrm{e}^{-\omega\tau}}{\omega-\omega'}\frac{\beta}{1+\mathrm{e}^{-\beta\omega}} \tag{5.32}$$

and there is only a pole ($\omega = \omega'$) that is enclosed by the contour (see Fig. 5.4). Applying the Cauchy's residue theorem again, we arrive at

$$\frac{-1}{\beta}\sum_{\mathrm{i}\omega_n}\frac{\mathrm{e}^{-\mathrm{i}\omega_n\tau}}{\mathrm{i}\omega_n-\omega'}=\frac{\mathrm{e}^{-\omega'\tau}}{1+\mathrm{e}^{-\beta\omega'}} \tag{5.33}$$

and

$$G(\tau)=\int_{-\infty}^{\infty}d\omega\frac{\mathrm{e}^{-\tau\omega}}{1+\mathrm{e}^{-\beta\omega}}A(\omega). \tag{5.34}$$

Yet, the inversion is an ill-posed problem as it is similar to performing an inverse Laplace transform with the noisy and incomplete Monte Carlo data.

In our study, the inversion is handled through a Bayesian-based maximum entropy approach; see [112] for detailed reviews. It regards the spectral function $A(\omega)$ as the argument of a probability function and information about $A(\omega)$ prior to Monte Carlo simulations is encoded in *prior probability* while the *likelihood function* is the conditional probability of producing the generated Monte Carlo data $\tilde{G}(\tau)$ from a given $A(\omega)$. The MaxEnt approach consequently outputs the $A(\omega)$ that maximizes the *posterior probability*, which is proportional to the product of prior probability and likelihood function [113].

Maximizing the likelihood function amounts to performing a least-square fit to the Monte Carlo data. On the other hand, the prior probability is specified in terms of information theoretic entropy. This entropy is defined relative to a default model $m(\omega)$ such that in the absence of data, the output $A(\omega)$ is $m(\omega)$. The choice of $m(\omega)$ is arbitrary, but it is usually chosen as the smoothest function consistent with prior knowledge of the spectral function, such as sum rules. Hence, a flat model with a magnitude to satisfy the sum rule in the frequency range of interest is typically chosen.

There is one more free parameter left, the Lagrange multiplier α that connects χ^2 (related to least-square fit of data) and entropy S (related to prior knowledge

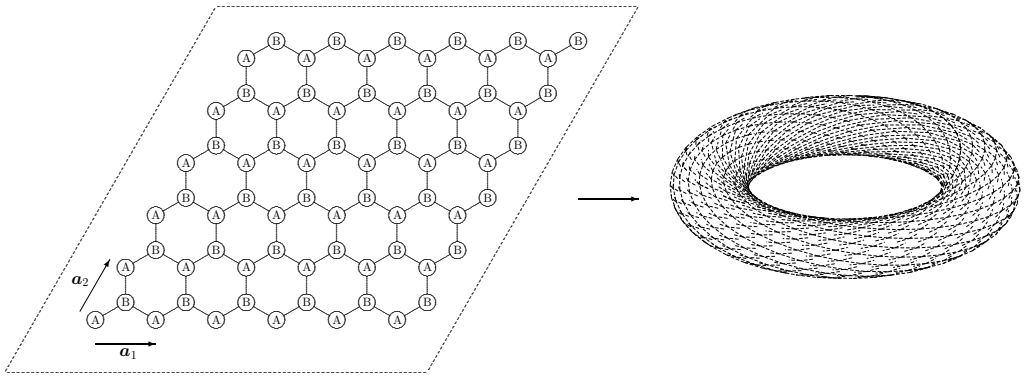

Figure 5.5: Finite honeycomb lattice of linear dimension $L = 6$. The total number of sites is $N = 2L^2 = 72$. Due to periodic boundary conditions, the finite size lattice can be wrapped onto the surface of a torus in a twisted manner. As L increases, the two radii of the torus also increase. The 1st BZ of the non-interacting particles can also be mapped onto a torus with the values of two radii determined by the lattice parameter. Single-particle states are evenly distributed on this toroidal surface, with the total number of states determined by the number of unit cells.

on spectral functions). However, this Lagrange multiplier can also be determined using Bayesian logic [114], therefore, the method leaves no parameters to adjust arbitrarily.

In summary, the calculation is carried out by parameterizing $A(\omega)$ as N δ-functions on a uniform grid of frequencies ω_l. The amplitudes A_l of the δ-functions are sampled from a probability distribution $p(A) \sim \exp[-\chi^2/\Theta + \alpha S]$. An annealing procedure is used starting from large Θ, which is then slowly reduced. For the extraction of the various spectral functions $A(\omega)$ in this work, the chi-square values, defined by

$$\chi^2 = \sum_l \left(\frac{\tilde{G}(\tau_l) - G(\tau_l)}{\Delta\tilde{G}(\tau_l)} \right)^2 , \tag{5.35}$$

where τ_l refers to the discretized imaginary time, $\Delta\tilde{G}(\tau_l)$ is the error in the Monte Carlo data $\tilde{G}(\tau_l)$ and $G(\tau_l)$ is calculated according to Eq. (5.34), are typically below 10.

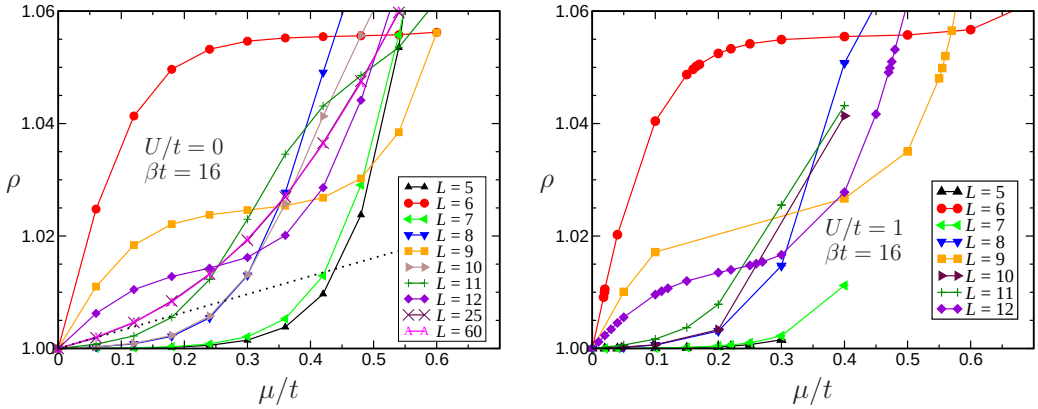

Figure 5.6: Total average density ρ *vs* chemical potential μ for $U/t = 0$ (left) and $U/t = 1$ (right) at $\beta t = 16$ and different lattice sizes L. The left figure is obtained by analytical calculation at $U = 0$. The right figure is obtained from numerical data generated by DQMC. For sizes that are not multiples of three, there is no state at half-filling and a small gap appears for small system sizes. There is no such gap when L is a multiple of three. For sizes that are multiples of three, plateaus appear away from half-filling. These plateaus are also finite-size effects and they disappear when $L \to \infty$. The dotted line in the left figure is obtained by an exact evaluation of the derivative $\partial\rho/\partial\mu|_{\mu=0}$ in the non-interacting limit when $L \to \infty$. The two figures show that the "magic number 3" effect is present even when the interaction strength U is comparable to the hopping parameter t.

5.4 Finite size lattice

In the DQMC simulations, we have used the honeycomb lattice depicted in Fig. 5.5 with periodic boundary conditions. There are L unit cells in each direction defined by the primitive vectors $\boldsymbol{a}_1$ and $\boldsymbol{a}_2$. A finite honeycomb lattice of side L then contains $N_c = L^2$ unit cells and $N = 2L^2$ sites. In the non-interacting case, the discretized energy levels are given by [3, 52]

$$\epsilon_{\pm}(k_1, k_2) = \pm t \left| 1 + e^{i2\pi k_1/L} + e^{i2\pi k_2/L} \right|,$$

where $k_1, k_2 \in \{0, 1, \cdots, L-1\}$. When L is a multiple of three, there always exist pairs (k_1, k_2) such that $\epsilon_{\pm}(k_1, k_2) = 0$, i.e. there are four states (two per spin state) located exactly at the points where the two bands meet and only two of these states will be occupied if $\rho = 1$. This does not happen when L is not a multiple

of three. As a consequence, on small finite-size systems, a small gap of order $1/L$ appears around half-filling when L is not a multiple of three (see Fig. 5.6). To avoid confusion between this gap, which is a finite-size effect, and the Mott gaps generated by interactions that are expected to appear in ordered phases, we used (especially at half-filling) sizes L that are multiples of three. This limits strongly the sizes that can be studied. In the most favorable cases, we went up to $L = 15$, that is $N = 450$ sites.

For the most time-consuming calculations done in this work, i.e. $L = 15$, we spent about a week of CPU time to compute the pair Green's function in a single simulation involving 2000 warm-up sweeps and 2000 measurement sweeps. The processor model that we had used is Intel(R) Xeon(R) X5482 which can operates at a maximum speed of 3.20GHz.

5.5 Summary

We had explained the tuning of interaction strength between fermionic atoms through Feshbash resonances and justified the use of the Hubbard model with on-site interactions to describe the cold atoms trapped in an optical lattice. We also briefly explained the DQMC algorithm, which provides us with simulated data on correlation functions, and the MaxEnt method, which enables us to extract frequency-dependent spectral function from the DQMC data. The finite size effects present in the honeycomb lattice was briefly explained. It poses serious limitations on the possible lattice sizes and makes a finite size scaling analysis of DQMC results difficult.

Chapter 6

Interacting system II: Data and Analysis

6.1 BCS-BEC crossover

In the continuum at zero temperature, as the interacting fermionic gas is driven from the weak to the strong attractive coupling limit, there is a crossover from a BCS regime of weakly-bound delocalized pairs to a Bose-Einstein condensate (BEC) of tightly-bound pairs (later called molecules for simplicity) [115–117]. At finite temperature, the Mermin-Wagner theorem prevents continuous symmetries to be broken in a two-dimensional system [118, 119], hence there is no superconducting phase transition in a Hubbard model [120, 121]. However, at finite but sufficiently low temperature, a similar BCS-molecule crossover is observed except that there is only quasi-long-range order and, consequently, no true condensate but only a superfluid. This could be understood as a consequence of the Berezinskii-Kosterlitz-Thouless (BKT) [122–124] transition at some critical temperature T_c. In this picture, the superconducting gap parameters (defined on each lattice site) are complex variables and play the role of classical spins lying on the xy-plane

which couple antiferromagnetically. We thus have an XY model of spins with antiferromagnetic interactions. Above T_c, free vortices of spins exist in the system and the spin-spin correlation function vanishes over a long distance. Below T_c, the vortices can only exist in pairs and the spin-spin correlation function still vanishes over a long distance, but now exhibits a power-law decay.

Even though our work [42] studies interacting particles on a lattice represented by a simple fermionic Hubbard model [99, 100], some aspects of the continuum limit, such as the BCS-BEC crossover, are expected to be reproduced in the discrete model. Zhao and Paramekanti have explored the attractive fermionic Hubbard model on a honeycomb lattice using mean-field theory [125] and they found a quantum phase transition (QPT) between a semi-metal and a superfluid at half-filling. Away from half-filling, they recovered the crossover already observed in the continuum limit. Recently, Su *et al.* used DQMC methods to study the BCS-BEC crossover on the honeycomb lattice away from half-filling and concluded that it was similar to the one obtained for the square lattice [126]. In the present work, we use DQMC simulations and large system sizes to study the pair formation at half-filling and attempt to determine the critical value of the coupling strength at which pairs form. We then study pairing away from half-filling by analyzing several quantities, including spectral functions.

At this point, we would like to mention a recent work by Meng *et al.* [43], published after this thesis was first drafted. Their work is similar to ours, but the numerical computations were performed using projective (temperature $T = 0$) determinant QMC simulations in the canonical ensemble at a large lattice size (up to $L = 18$) with much lower temperature ($\beta t = 40$) and smaller imaginary time step ($\Delta\tau = 0.05/t$) compared to ours. They found that, in between a semi-metal and an AF-ordered Mott insulator, the system at half-filling first turns into a quantum spin liquid [44–46] as the repulsive interaction strength increases and they related

the spin liquid to a short-range resonating valence bond liquid, a picture that was proposed for high-T_c superconductor. We will discuss their work in more detailed in Sec. 6.3.

6.2 Mean-field theory of a perfect honeycomb lattice

Before we move on, let us briefly mention the mean-field approach and its results with the important caveat that the correctness of the theory depends crucially on the spatial dimension d of the system. Above an upper critical dimension (which is 4 for an Ising model without external magnetic field and may varies for other models), the theory is good at all temperatures; it can provide the critical exponents and it is a starting point for systematic corrections, such as including the quadractic fluctuations around the mean-field solution. Below the upper but above a lower critical dimension, the mean-field theory works relatively well except near the critical point. Unfortunately, $d = 2$ is just the lower critical dimension at which our mean-field approach fails [111]. Nevertheless, as we shall see later, the mean-field theory surprisingly gives us a qualitatively correct picture when compared with Monte Carlo results, even though the numbers are quantitatively wrong.

The key idea to derive a mean-field theory is to first rewrite the partition function (5.2) into a path-integral form through fermionic coherent states, followed by a proper choice of order parameters to decouple the interaction terms. Once this is done, a stationary phase approximation is applied to the partition function to yield the mean-field solution (this is similar to finding the classical trajectory for the propagation of particles) [127]. Without going into the path-integral formalism, we can also obtain the mean-field solution by interpreting the interactions between

fermions as interactions between fermions and an effective field proportional to the order parameter. We have thus converted the many-body Hamilton operator (5.1) into a one-body problem, which can be solved easily. Alternatively, we can choose not to re-express the interaction terms but to keep only relevant terms, such as the "pairing" terms, in H_V of Eq. (5.1). A minimization of this remaining Hamilton operator within the class of generalized BCS state yields identical results [36].

In the following, we shall follow the path-integral approach to obtain the mean-field equations [127–129]. The partition function (5.2) is written as

$$\mathcal{Z} = \int D[\phi^*]D[\phi]\mathrm{e}^{-S[\phi^*,\phi]}, \tag{6.1}$$

where $\{\phi^*_{\boldsymbol{i}\sigma}(\tau), \phi_{\boldsymbol{i}\sigma}(\tau)\}$ are Grassmann variables with anti-periodic boundary condition, $\phi_{\boldsymbol{i}\sigma}(\beta) = -\phi_{\boldsymbol{i}\sigma}(0)$, while $D[\phi^*]D[\phi]$ is just a short-hand notation for the integration measure. The Euclidean action is given by

$$\begin{aligned} S[\phi^*,\phi] &= \int_0^\beta d\tau \left\{ \sum_{\boldsymbol{i},\sigma} \phi^*_{\boldsymbol{i}\sigma}(\tau)\frac{\partial}{\partial\tau}\phi_{\boldsymbol{i}\sigma}(\tau) + H[\phi^*(\tau),\phi(\tau)] \right\}, \\ H[\phi^*,\phi] &= K[\phi^*,\phi] + V[\phi^*,\phi], \end{aligned} \tag{6.2}$$

where $K[\phi^*,\phi]$ includes the kinetic energy and chemical potential while $V[\phi^*,\phi]$ is contributed by the interaction terms.

In the momentum space representation, the kinetic energy and the chemical potential are combined into

$$K[\phi^*,\phi] = \sum_{\boldsymbol{k},\sigma} (\phi^*_{\mathrm{A},\boldsymbol{k}\sigma}, \phi^*_{\mathrm{B},\boldsymbol{k}\sigma}) \begin{pmatrix} -\tilde{\mu} & Z_{\boldsymbol{k}} \\ Z^*_{\boldsymbol{k}} & -\tilde{\mu} \end{pmatrix} \begin{pmatrix} \phi_{\mathrm{A},\boldsymbol{k}\sigma} \\ \phi_{\mathrm{B},\boldsymbol{k}\sigma} \end{pmatrix}, \tag{6.3}$$

where $\tilde{\mu} = \mu - U/2$ is the actual chemical potential measured in experiments while

the attractive interaction term becomes

$$V[\phi^*,\phi] = -\frac{U}{N_c}\sum_{\substack{\boldsymbol{q},\boldsymbol{k},\boldsymbol{k'}\in\Omega \\ s=\mathrm{A,B}}} \phi^*_{s,\boldsymbol{k}+\frac{\boldsymbol{q}}{2}\uparrow}\phi^*_{s,-\boldsymbol{k}+\frac{\boldsymbol{q}}{2}\downarrow}\phi_{s,-\boldsymbol{k'}+\frac{\boldsymbol{q}}{2}\downarrow}\phi_{s,\boldsymbol{k'}+\frac{\boldsymbol{q}}{2}\uparrow}. \tag{6.4}$$

The presence of N_c in the denominator is due to our considerations of a finite lattice with N_c unit cells. Correspondingly, the sum over each of the reciprocal space vectors $\{\boldsymbol{k},\boldsymbol{k'},\boldsymbol{q}\}$ involves N_c values. From Eq. (6.4), we can see that the on-site interactions translate into interactions between all pairs of fermions with the same value of total momentum $\boldsymbol{q}$ but this value of $\boldsymbol{q}$ is preserved by the interaction. This is a consequence of translational invariance of the pair interaction potential H_V. Hence, instead of the crystal momentum $\boldsymbol{k}$ of a single particle (see Sec. 2.2), we may use the momentum $\boldsymbol{q}$ of the center-of-mass of a pair to label a two-particle eigenstate of the interacting Hamilton operator.

The Hubbard-Stratonovich transformation is introduced to decouple the interaction terms through the following identity,

$$\begin{aligned} 1 = \int D[\Delta^*_{s,\boldsymbol{q}}]D[\Delta_{s,\boldsymbol{q}}]\exp\Bigg\{\int_0^\beta d\tau \sum_{\boldsymbol{q},s=\mathrm{A,B}}\left(\Delta^*_{s,\boldsymbol{q}} - \frac{U}{\sqrt{N_c}}\sum_{\boldsymbol{k}}\phi^*_{s,\boldsymbol{k}+\frac{\boldsymbol{q}}{2}\uparrow}\phi^*_{s,-\boldsymbol{k}+\frac{\boldsymbol{q}}{2}\downarrow}\right)\left(-\frac{1}{U}\right) \\ \times\left(\Delta_{s,\boldsymbol{q}} - \frac{U}{\sqrt{N_c}}\sum_{\boldsymbol{k}}\phi_{s,-\boldsymbol{k}+\frac{\boldsymbol{q}}{2}\downarrow}\phi_{s,\boldsymbol{k}+\frac{\boldsymbol{q}}{2}\uparrow}\right)\Bigg\}, \end{aligned} \tag{6.5}$$

where $\{\Delta^*_{s,\boldsymbol{q}},\Delta_{s,\boldsymbol{q}}\}$ are bosonic fields with complex values. It will be apparent later that they serve as the order parameters as well as the effective fields which interact with the fermions.

In order to cast the partition function into a convenient form so that the Euclidean action could be written in matrix form, we employ two properties of the Grassmann variables,

1. Anti-commutation relation: $\phi_{s,\boldsymbol{k}\sigma}\phi^*_{s',\boldsymbol{k}'\sigma'} + \phi^*_{s',\boldsymbol{k}'\sigma'}\phi_{s,\boldsymbol{k}\sigma} = 0$. Using this,

$$\sum_{\boldsymbol{k},\boldsymbol{k}',s=\pm} \phi^*_{s,\boldsymbol{k}\downarrow}(\epsilon_{s,\boldsymbol{k}} - \tilde{\mu})\phi_{s,\boldsymbol{k}'\downarrow} = -\sum_{\boldsymbol{k},\boldsymbol{k}',s=\pm} \phi_{s,\boldsymbol{k}'\downarrow}(\epsilon_{s,\boldsymbol{k}} - \tilde{\mu})\phi^*_{s,\boldsymbol{k}\downarrow}. \tag{6.6}$$

2. Anti-periodic boundary condition: $\phi_{\boldsymbol{i}\sigma}(\beta) = -\phi_{\boldsymbol{i}\sigma}(0)$. Integration by parts yields

$$\begin{aligned}\int_0^\beta d\tau\phi^*(\tau)\frac{\partial}{\partial\tau}\phi(\tau) &= \underbrace{\phi^*(\tau)\phi(\tau)|_{\tau=0}^{\tau=\beta}}_{=0} - \int_0^\beta d\tau\left(\frac{\partial}{\partial\tau}\phi^*(\tau)\right)\phi(\tau) \\ &= \int_0^\beta d\tau\phi(\tau)\frac{\partial}{\partial\tau}\phi^*(\tau).\end{aligned} \tag{6.7}$$

We are now ready to cast the partition function (6.1) into

$$\mathcal{Z} = \int D[\phi^*]D[\phi]D[\Delta^*]D[\Delta]\mathrm{e}^{-S[\Delta^*,\Delta,\phi^*,\phi]} \tag{6.8}$$

with the Euclidean action given by

$$\begin{aligned}S[\Delta^*,\Delta,\phi^*,\phi] = \int_0^\beta d\tau\Big\{ &\sum_{\boldsymbol{k},\boldsymbol{q}} \Phi^\dagger_{\boldsymbol{k}}(\boldsymbol{q},\tau)[-\mathbf{G}^{-1}_{\boldsymbol{k}}(\boldsymbol{q},\tau)]\Phi_{\boldsymbol{k}}(\boldsymbol{q},\tau) \\ &+ \sum_{\boldsymbol{q},s=\mathrm{A},\mathrm{B}} \frac{|\Delta_{s,\boldsymbol{q}}(\tau)|^2}{U}\Big\}\end{aligned} \tag{6.9}$$

where the four-dimensional vector $\Phi^\dagger_{\boldsymbol{k}}(\boldsymbol{q},\tau)$ is defined as

$$\Phi^\dagger_{\boldsymbol{k}}(\boldsymbol{q},\tau) = \left(\phi^*_{\mathrm{A},\boldsymbol{k}\uparrow}(\tau), \phi^*_{\mathrm{B},\boldsymbol{k}\uparrow}(\tau), \phi_{\mathrm{A},-\boldsymbol{k}+\boldsymbol{q}\downarrow}(\tau), \phi_{\mathrm{B},-\boldsymbol{k}+\boldsymbol{q}\downarrow}(\tau)\right). \tag{6.10}$$

The inverse Green's function $\mathbf{G}^{-1}_{\boldsymbol{k}}(\boldsymbol{q},\tau)$ is given by

$$\mathbf{G}^{-1}_{\boldsymbol{k}}(\boldsymbol{q},\tau) = \begin{pmatrix} \frac{1}{N_c}G^{-1}_{0\uparrow}(\boldsymbol{k},\tau) & \Delta_{\boldsymbol{q}}(\tau) \\ \Delta^*_{\boldsymbol{q}}(\tau) & \frac{-1}{N_c}\tilde{G}^{-1}_{0\downarrow}(-\boldsymbol{k}+\boldsymbol{q},\tau) \end{pmatrix}, \tag{6.11}$$

where

$$G_{0\sigma}^{-1}(\boldsymbol{k},\tau) = \begin{pmatrix} -\partial_\tau + \tilde{\mu}_\sigma & -Z_{\boldsymbol{k}} \\ -Z_{\boldsymbol{k}}^* & -\partial_\tau + \tilde{\mu}_\sigma \end{pmatrix}, \tilde{G}_{0\sigma}^{-1}(\boldsymbol{k},\tau) = \begin{pmatrix} \partial_\tau + \tilde{\mu}_\sigma & -Z_{\boldsymbol{k}}^* \\ -Z_{\boldsymbol{k}} & \partial_\tau + \tilde{\mu}_\sigma \end{pmatrix},$$

$$\Delta_{\boldsymbol{q}}(\tau) = \frac{1}{\sqrt{N_c}} \begin{pmatrix} \Delta_{\mathrm{A},\boldsymbol{q}}(\tau) & 0 \\ 0 & \Delta_{\mathrm{B},\boldsymbol{q}}(\tau) \end{pmatrix}.$$

The significance of $\boldsymbol{q}$ is it being the momentum of a weakly-bound pair. It could be non-zero when the two spin populations are unbalanced. However, since $\mu_\uparrow = \mu_\downarrow$ in our study, bound pairs possess zero momentum to minimize their energy. Let us consider the evolution of our system from a normal state into a superfluid. In the normal state, the system is charaterized by $\Delta_{\boldsymbol{q}} = 0\ \forall \boldsymbol{q}$, hence we break up the inverse Green's function into a non-interacting part and the self-energy. We rewrite the sum in the Euclidean action as

$$\begin{aligned} \sum_{\boldsymbol{k},\boldsymbol{q}} \Phi_{\boldsymbol{k}}^\dagger(\boldsymbol{q},\tau)[-\mathbf{G}_{\boldsymbol{k}}^{-1}(\boldsymbol{q},\tau)]\Phi_{\boldsymbol{k}}(\boldsymbol{q},\tau) = &\sum_{\boldsymbol{k}} \Phi_{\boldsymbol{k}}^\dagger(\mathbf{0},\tau)[-\mathbf{G}_0^{-1}(\tau)]_{\boldsymbol{k}}\Phi_{\boldsymbol{k}}(\mathbf{0},\tau) \\ &+ \sum_{\boldsymbol{k},\boldsymbol{q}} \Phi_{\boldsymbol{k}}^\dagger(\boldsymbol{q},\tau)\boldsymbol{\Sigma}_{\boldsymbol{q}}(\tau)\Phi_{\boldsymbol{k}}(\boldsymbol{q},\tau), \end{aligned} \tag{6.12}$$

where the non-interacting part is

$$[\mathbf{G}_0^{-1}(\tau)]_{\boldsymbol{k}} = \begin{pmatrix} G_{0\uparrow}^{-1}(\boldsymbol{k},\tau) & 0 \\ 0 & -\tilde{G}_{0\downarrow}^{-1}(-\boldsymbol{k},\tau) \end{pmatrix} \tag{6.13}$$

and the self-energy is

$$\boldsymbol{\Sigma}_{\boldsymbol{q}}(\tau) = \begin{pmatrix} 0 & \Delta_{\boldsymbol{q}}(\tau) \\ \Delta_{\boldsymbol{q}}^*(\tau) & 0 \end{pmatrix}. \tag{6.14}$$

The non-interacting Green's function is readily found to be

$$G_{0\sigma}(\boldsymbol{k},\tau) = \frac{1}{\beta}\sum_{n} \frac{\mathrm{e}^{-\mathrm{i}\omega_n\tau}}{(\mathrm{i}\omega_n+\tilde{\mu}_\sigma)^2 - |Z_{\boldsymbol{k}}|^2} \begin{pmatrix} \mathrm{i}\omega_n+\tilde{\mu}_\sigma & Z_{\boldsymbol{k}} \\ Z^*_{\boldsymbol{k}} & \mathrm{i}\omega_n+\tilde{\mu}_\sigma \end{pmatrix}, \tag{6.15}$$

where $\omega_n = \frac{(2n+1)\pi}{\beta}$ are the Matsubara frequencies for fermions. When the Grassmann variables are integrated out, we are left with an effective action in terms of the pairing fields,

$$S^{\mathrm{eff}}[\Delta^*,\Delta] = \int_0^\beta d\tau \left\{ \sum_{\boldsymbol{q},s=\mathrm{A,B}} \left(\frac{|\Delta_{s\boldsymbol{q}}(\tau)|^2}{U} \right) - \mathrm{Tr}\left[\log(-\mathbf{G}^{-1}_{\boldsymbol{k}}(\boldsymbol{q},\tau))\right] \right\}, \tag{6.16}$$

and we employ the identity

$$-\mathrm{Tr}\left[\log(-\mathbf{G}^{-1})\right] = -\mathrm{Tr}\left[\log(-\mathbf{G}_0^{-1})\right] + \sum_{m=1}^{\infty} \frac{1}{m}\mathrm{Tr}\left[(\mathbf{G}_0\boldsymbol{\Sigma})^m\right] \tag{6.17}$$

to expand the effective action in powers of $\{\Delta^*,\Delta\}$ close to the transition. We further consider static s-wave pairing, i.e. $\Delta_{\mathrm{A},\mathbf{0}}(\tau) = \Delta_{\mathrm{B},\mathbf{0}}(\tau) = \Delta_0$ and put the remaining $\Delta_{s,\boldsymbol{q}\neq\mathbf{0}}$ to zero. The effective action can then be expressed in the form $S^{\mathrm{eff}} = \alpha_s|\Delta_0|^2 + \beta_s|\Delta_0|^4 + \ldots$. At a finite temperature, due to the factor of $1/U$ in Eq. (6.16), α_s is arbitrarily large when $U = 0$, hence an ordered phase is not favourable. A phase transition occurs when the coefficient α_s changes sign from positive to negative value such that the $\Delta_0 = 0$ solution is no longer a stable minimum. The value of Δ_0 at which the action is minimal can thus be treated as an order parameter for the pair phase coherence. Setting $\alpha_s = 0$ at the transition and performing the evaluation at $\Delta_0 = 0$, we can then find the critical interaction strength U_c at which the phase coherence starts to exist. The corresponding mean-

field gap equation is

$$\frac{1}{U} = \frac{1}{2N_c} \sum_{\boldsymbol{k},s=\pm} \frac{\tanh(\beta\xi_{s,\boldsymbol{k}}/2)}{2\xi_{s,\boldsymbol{k}}} \quad \text{with} \quad \xi_{s,\boldsymbol{k}} = \epsilon_{s,\boldsymbol{k}} - \tilde{\mu}. \tag{6.18}$$

Away from half-filling ($\tilde{\mu} \neq 0$), the gap equation (6.18) can be satisfied for arbitrarily small U due to contributions from single-particle states at the Fermi level[1]. However, at $\tilde{\mu} = 0$, the gap equation can only be satisfied for a minimum non-zero U_c due to the vanishing density of states at the Fermi level. A numerical evaluation of the gap equation at $T = 0$ yields $U_c = 2.23t$. As will be shown later, our DQMC results show that the transition actually occurs at $U_c \approx 5t$, a significant deviation from the mean-field prediction.

6.3 Half-filled lattice

6.3.1 Spin and pseudo-spin symmetries in the Hubbard model

It is hard to solve the Hubbard model (5.1)[2], but it does not prevent us from gaining some understanding on the system by analyzing the symmetries of the Hamilton operator, the most important of all being the SO(4) symmetry, which is composed of a spin SU(2) symmetry, a pseudo-spin SU(2) symmetry and a particle-hole $\mathbb{Z}_2$ symmetry. In the present context of attractive interactions, the pseudo-spin plays a more important role than the spin SU(2) symmetry due to its relation to s-wave pairing and density wave. Below, we shall present this symmetry in the way illustrated by Zhang [130].

The Hubbard model (5.1) defined on a bipartite lattice possesses a set of oper-

[1] The Fermi level lies at $\tilde{\mu}$ instead of μ in the mean-field approximation.

[2] To date, the Hubbard model has no known analytical solution except for some limiting cases.

ators

$$J_- = \sum_{\boldsymbol{i}} (-1)^{\boldsymbol{i}} \Delta_{\boldsymbol{i}}, \quad J_+ = J_-^\dagger, \quad J_0 = \frac{1}{2} \sum_{\boldsymbol{i}} (n_{\boldsymbol{i}} - 1) \tag{6.19}$$

that obey the commutation relations $[J_0, J_\pm] = J_\pm$, $[J_+, J_-] = 2J_0$ of an SU(2) algebra. Again, the index $\boldsymbol{i}$ is even on sublattice A while odd on sublattice B. Instead of having states of the system to form the irreducible representation of this symmetry, we can find that the s-wave pairing operators

$$\Delta_- = \frac{1}{\sqrt{2}} \sum_{\boldsymbol{i}} \Delta_{\boldsymbol{i}}, \ \Delta_+ = -\Delta_-^\dagger$$

and the density wave operator

$$\Delta_0 = \frac{1}{2} \sum_{\boldsymbol{i}} (-1)^{\boldsymbol{i}} n_{\boldsymbol{i}}$$

form an irreducible tensor of rank $l = 1$ under these SU(2) algebra, in the sense that

$$[J_0, \Delta_m] = m\Delta_m, \quad [J_\pm, \Delta_m] = \sqrt{l(l+1) - m(m+1)}\Delta_{m\pm1}, \tag{6.20}$$

where $m = 0, \pm 1$. Physically, this means that the on-site pairing and density wave can be 'rotated' into each other by the pseudospin generators. To obtain the relation between the density wave structure factor S_{dw} and pair structure factor P_{s} (see Eqs. (5.16) and (5.18)), we construct an irreducible tensor of rank $l = 0$ under the pseudo-spin symmetry,

$$\Xi = \Delta_+\Delta_- + \Delta_-\Delta_+ - \Delta_0\Delta_0. \tag{6.21}$$

At half-filling, the pseudo-spin generators commute with the Hamilton operator (5.1), thus the thermal average of Ξ is invariant under pseudo-spin rotations.

μ/t	ρ	$S_{\rm dw}/2$	$P_{\rm s}$
0	1.0	1.125 ± 0.005	1.127 ± 0.001
0.9202	1.5	0.3356 ± 0.0004	10.5 ± 0.1

Table 6.1: Comparison of $P_{\rm s}$ and $S_{\rm dw}/2$ for $L = 12$, $\beta t = 20$, $U/t = 3$, and different values of μ/t. At half-filling, those quantities are equal within statistical error bars as a consequence of the SU(2) pseudo-spin symmetry of the FAHM. $S_{\rm dw}$ and $P_{\rm s}$ are small because $U < U_c$ and the system is in its semi-metallic phase. This symmetry is broken when $\mu \neq 0$ and this is confirmed by the numerical data showing that the two quantities are indeed unequal. $S_{\rm dw}$ remains small but $P_{\rm s}$ is large due to the presence of quasi-long-range order.

Atttractive Model		Repulsive Model	
Kinetic energy	$-t\left(f^{\dagger}_{\boldsymbol{i}\downarrow} f_{\boldsymbol{j}\downarrow}\right)$	Kinetic energy	$-t\left(h^{\dagger}_{\boldsymbol{j}\downarrow} h_{\boldsymbol{i}\downarrow}\right)$
Interactions	$-U\left(n_{\boldsymbol{i}\uparrow}-\frac{1}{2}\right)\left(n_{\boldsymbol{i}\downarrow}-\frac{1}{2}\right)$	Interactions	$U\left(n_{\boldsymbol{i}\uparrow}-\frac{1}{2}\right)\left(n^{h}_{\boldsymbol{i}\downarrow}-\frac{1}{2}\right)$
Doping	$-\mu(n_{\boldsymbol{i}\uparrow}+n_{\boldsymbol{i}\downarrow})$	Zeeman field	$-\mu(n_{\boldsymbol{i}\uparrow}-n^{h}_{\boldsymbol{i}\downarrow})$
Zeeman field	$-h_z(n_{\boldsymbol{i}\uparrow}-n_{\boldsymbol{i}\downarrow})$	Doping	$-h_z(n_{\boldsymbol{i}\uparrow}+n^{h}_{\boldsymbol{i}\downarrow})$
Pairing	$P_{\rm s}$	AF order (xy-plane)	$\frac{1}{N}\sum_{\boldsymbol{i},\boldsymbol{j}}(-1)^{\boldsymbol{i}+\boldsymbol{j}}\langle\tilde{S}^{x}_{\boldsymbol{i}}\tilde{S}^{x}_{\boldsymbol{j}}+\tilde{S}^{y}_{\boldsymbol{i}}\tilde{S}^{y}_{\boldsymbol{j}}\rangle$
Density wave	$S_{\rm dw}$	AF order (z-axis)	$\frac{4}{N}\sum_{\boldsymbol{i},\boldsymbol{j}}(-1)^{\boldsymbol{i}+\boldsymbol{j}}\langle\tilde{S}^{z}_{\boldsymbol{i}}\tilde{S}^{z}_{\boldsymbol{j}}\rangle$

Table 6.2: An attractive Hubbard model on a bipartite lattice can be transformed into a repulsive Hubbard model through a partial particle-hole transformation. The correspondence between the various physical quantities of the two models are shown.

We expect that the three components in Ξ contribute equally, hence $\langle\Delta_{+}\Delta_{-} + \Delta_{-}\Delta_{+}\rangle = -2\langle\Delta_0\Delta_0\rangle$. A straight-forward substitution yields $P_{\rm s} = S_{\rm dw}/2$. Indeed, our DQMC data shown in Table 6.1 support our analysis. Away from half-filling, the pseudo-spin generators no longer commute with the Hamilton operator and the equality between $P_{\rm s}$ and $S_{\rm dw}$ no longer holds.

The pseudo-spin generators in Eq. (6.19) may be written in a more transparent way to show its relation to the spin generators [131, 132]. We define the spin and

pseudo-spin vectors at a given site $\boldsymbol{i}$ as

$$\boldsymbol{S_i} = \frac{1}{2}\Psi^{\dagger}_{\mathrm{S}\boldsymbol{i}}\boldsymbol{\sigma}\Psi_{\mathrm{S}\boldsymbol{i}}, \quad \Psi_{\mathrm{S}\boldsymbol{i}} = \begin{pmatrix} f_{\boldsymbol{i}\uparrow} \\ f_{\boldsymbol{i}\downarrow} \end{pmatrix}, \tag{6.22}$$

$$\boldsymbol{J_i} = \frac{1}{2}\Psi^{\dagger}_{\mathrm{J}\boldsymbol{i}}\boldsymbol{\sigma}\Psi_{\mathrm{J}\boldsymbol{i}}, \quad \Psi_{\mathrm{J}\boldsymbol{i}} = \begin{pmatrix} f_{\boldsymbol{i}\uparrow} \\ (-1)^{\boldsymbol{i}} f^{\dagger}_{\boldsymbol{i}\downarrow} \end{pmatrix}, \tag{6.23}$$

where $\boldsymbol{\sigma}$ is the vector of standard Pauli matrices. Clearly, the spin vector can be transformed into the pseudo-spin operator and vice versa through a partial particle-hole transformation [133–136], where a spin-$\downarrow$ particle annihilation operator $f_{\boldsymbol{i}\downarrow}$ is replaced by a spin-$\downarrow$ hole creation operator $h^{\dagger}_{\boldsymbol{i}\downarrow}$,

$$(-1)^{i} h^{\dagger}_{i\downarrow} = f_{i\downarrow}, \tag{6.24}$$

while the spin-$\uparrow$ particle operators remain unchanged. The form of the kinetic term is left unchanged in the spin-$\downarrow$ holes representation. The number operator $n_{\boldsymbol{i}\downarrow}$ is accordingly transformed into $1 - n^{h}_{\boldsymbol{i}\downarrow}$, where $n^{h}_{\boldsymbol{i}\downarrow} = h^{\dagger}_{\boldsymbol{i}\downarrow} h_{\boldsymbol{i}\downarrow}$ is the number operator for holes, and, up to a redefinition of the chemical potential μ, the sign of the interaction term is reversed. Consequently, at half-filling (μ=0), the attractive model is exactly mapped onto the repulsive Hubbard model. Through correct mapping of physical quantities, we are able to understand the physics of particles interacting attractively in the picture of repulsive Hubbard model; see Table. 6.2. For example, the repulsive Hubbard model can be reduced to a Heisenberg model with antiferromagnetic (AF) coupling in the strong interaction limit. Since the antiferromagnetic ordering in the repulsive model is immediately translated into pairing correlations and density ordering in the attractive model, pairing and density ordering are expected at strong interaction and the equality $P_{\mathrm{s}} = S_{\mathrm{dw}}/2$ is just a consequence of the fact that the spin-spin correlations are the same along the

three coordinate axes in the repulsive model,

$$\sum_{\boldsymbol{i},\boldsymbol{j}}(-1)^{\boldsymbol{i}+\boldsymbol{j}}\langle\tilde{S}^x_{\boldsymbol{i}}\tilde{S}^x_{\boldsymbol{j}}\rangle = \sum_{\boldsymbol{i},\boldsymbol{j}}(-1)^{\boldsymbol{i}+\boldsymbol{j}}\langle\tilde{S}^y_{\boldsymbol{i}}\tilde{S}^y_{\boldsymbol{j}}\rangle = \sum_{\boldsymbol{i},\boldsymbol{j}}(-1)^{\boldsymbol{i}+\boldsymbol{j}}\langle\tilde{S}^z_{\boldsymbol{i}}\tilde{S}^z_{\boldsymbol{j}}\rangle, \tag{6.25}$$

where x and y are the in-plane axes and z the axis orthogonal to the lattice plane and

$$\begin{aligned}\tilde{S}^x_{\boldsymbol{i}} &= \frac{1}{2}(f^\dagger_{i\uparrow}h_{i\downarrow} + h^\dagger_{i\downarrow}f_{i\uparrow}),\\ \tilde{S}^y_{\boldsymbol{i}} &= \frac{\mathrm{i}}{2}(h^\dagger_{i\downarrow}f_{i\uparrow} - f^\dagger_{i\uparrow}h_{i\downarrow}),\\ \tilde{S}^z_{\boldsymbol{i}} &= \frac{1}{2}(n_{i\uparrow} - n^h_{i\downarrow}).\end{aligned} \tag{6.26}$$

6.3.2 Weak and strong coupling limit of the Hubbard model

The non-interacting limit of the Hubbard model (5.1) has been explained in Sec. 2.4. At half-filling, the system corresponds to a semi-metal with vanishing density of states at the Fermi level. Furthermore, its low-energy excitations are Dirac fermions. On the other hand, since a doubly-occupied or fully-empty site has its interaction energy $-|U|/2$ less than a singly-occupied site, the ground state is dominated by doubly-occupied or fully-empty sites in the limit of infinitely strong attractive interactions. We can thus project the Hamilton operator onto a subspace with exactly $N/2$ doubly-occupied sites to obtain an effective Hamilton operator that describes the ground state in this limit [137, 138]. The derivation of this effective Hamilton operator is lengthy, so we will just quote the result,

$$H_{\text{eff}} = \frac{4t^2}{U}\sum_{\langle\boldsymbol{i},\boldsymbol{j}\rangle}\boldsymbol{J}_{\boldsymbol{i}}\cdot\boldsymbol{J}_{\boldsymbol{j}}. \tag{6.27}$$

Interested readers may refer to Appendix B.1 for the derivation. This effective Hamilton operator describes a Heisenberg model of pseudo-spins locked onto the

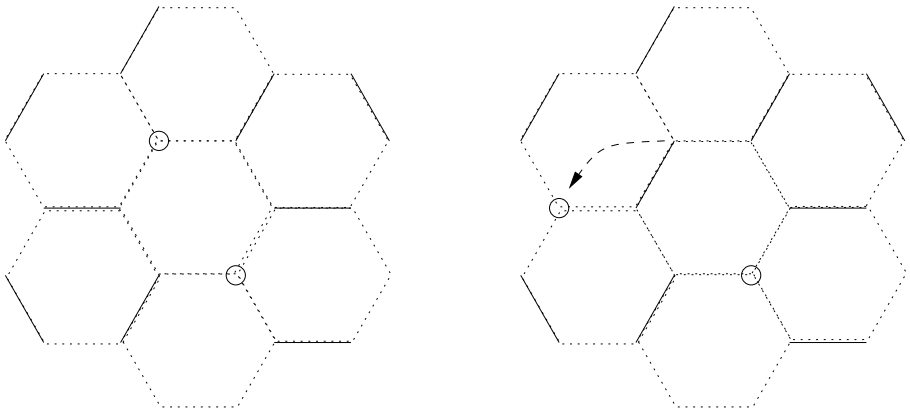

Figure 6.1: A schematic picture of resonating valence bond on the honeycomb lattice. A solid line represents a spin singlet between two lattice sites while an empty cirlce represents a hole. The dotted lines trace out the honeycomb lattice. A hole can move freely among the liquid of singlets while it costs energy to make a spin triplet excitation.

lattice sites. These pseudo-spins are free to rotate in three-dimension and they interact antiferromagnetically with the nearest neighbors. At $T = 0$, the ground state displays long-range AF order of pseudo-spins[3], i.e. there are long-range phase coherence and density order.

In between the two limiting phases, it was suggested that the system can exist as a (pseudo-)spin liquid [44–46]. Although there are various kinds of (pseudo-)spin liquids, the one that might be relevant to us (reflected by the numerical evidence from Ref. [43]) is the spin liquid with resonating valence bonds; see Fig. 6.1. It was suggested by Anderson to be the model for high-T_c superconductor [139]. From Eq. (6.27), it can be seen that it is energetically favourable to have a pseudo-spin singlet between two neighboring sites rather than a pseudo-spin triplet. Therefore, it is likely for the sytem to exist as a liquid of pseudo-spin singlets. When there is a hole (i.e. a site without a pseudo spin, which correspond to a singly-occupied lattice site in our model), the hole can move freely among the liquid of singlets because the total number of singlets is conserved. However, it costs energy to

[3]Mermin-Wagner theorem does not rule out phase transition at $T = 0$. See p. 66–67 of Ref. [131].

excite a pseudo-spin singlet to a pseudo-spin triplet, hence there is a gap in the pseudo-spin excitation spectrum. Furthermore, the singlet-singlet correlations are short-range. It was also suggested that superconductivity can be obtained in a repulsive Hubbard model by doping this spin liquid sufficiently strongly [139].

6.3.3 Transition from semi-metal to pseudo-spin liquid to superfluid and density wave

Paiva *et al.* [38] have studied the ground state of the fermionic repulsive Hubbard model (FRHM) on a honeycomb lattice a few years ago. They found a QPT from an antiferromagnetic phase at large coupling to a metallic phase at low coupling, the critical coupling strength being bounded by $4 \leq U_c/t \leq 5$. We use finite-size scaling and larger system sizes L to improve the numerical accuracy and narrow down the region of this QPT. Spin wave theory applied to Heisenberg models implies that the structure and pair structure factors at $T = 0$ scale with the number of lattice sites $N = 2L^2$ like [38, 131, 140, 141]

$$2P_{\mathrm{s}}(N) = S_{\mathrm{dw}}(N) \approx aN + b\sqrt{N} + c$$

where a, b, c are U-dependent nonnegative constants. In the disordered phase $S_{\mathrm{dw}}(N)$ is expected to reach a constant finite value as N goes to infinity, meaning that the coefficients a and b should then vanish. In the ordered phase, a should be strictly positive so that both P_{s} and S_{dw} diverge linearly with N, signaling the emergence of density and phase coherence orders. For system sizes up to $L = 15$, and using the vanishing of coefficient a to define the onset for the DW-SF phase, we infer that the critical interaction strength U_c falls within the range $5.0 < U_c/t < 5.1$ (Fig. 6.2). Meng *et al.* carried out similar procedure and found that U_c is around $4.3t$; see the curve of m_{s} in Fig. 6.3. The discrepancy between our results and

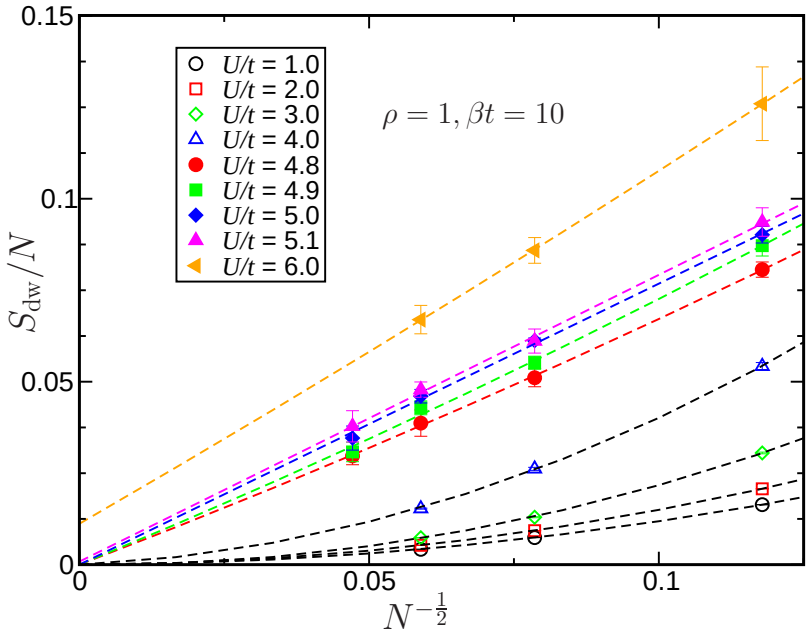

Figure 6.2: Scaling of the density wave structure factor $S_{\rm dw}$ with lattice size L at half-filling (the total number of lattice sites is $N = 2L^2$). The dashed lines are a fit of the form $S_{\rm dw}/N = a + b/\sqrt{N} + c/N$. Close to or above the transition ($U/t \gtrsim 5.0$), the coefficients a and b take on finite positive values implying that both density and phase coherence orders emerge in the thermodynamic limit $N \to \infty$. As it is seen, $S_{\rm dw}/N$ then essentially scales linearly with $1/\sqrt{N}$ and achieves the finite value a when $N \to \infty$. Below the transition ($U/t \lesssim 5$), the coefficients a and b vanish, meaning that the system reaches its disordered phase in the thermodynamic limit $N \to \infty$. As it is seen, $S_{\rm dw}/N$ then essentially scales as $1/N$ and goes to zero when $N \to \infty$. The QPT point is thus signaled by the vanishing of the coefficient a, from which we can infer that the critical interaction strength lie in the range $5.0 < U_c/t < 5.1$.

theirs may be accounted for by our simulations being carried out at a "not low enough" temperature.

In the study by Paiva *et al.*, the metallic phase appearing at low U was not studied in detail. In particular the question of the metallic or semi-metallic nature of the system was not addressed. Calculating the spectral function $A(\omega)$ for different values of U (Fig. 6.4), we find that the system is always a semi-metal when it is not in an ordered phase. The density of states drops around the Fermi level (located at $\omega = 0$) for $U/t < 5$ but without forming a gap. Instead, we observe a tiny metallic peak at the Fermi level. This peak is a finite-size effect due to

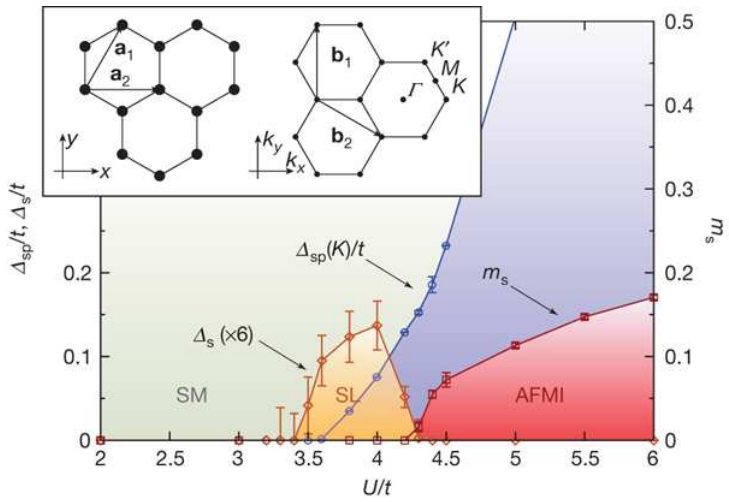

Figure 6.3: Phase diagram for the repulsive Hubbard model on the honeycomb lattice at half-filling. The semi-metal (SM) and the antiferromagnetic Mott insulator (AFMI) is separeted by a gapped spin liquid (SL) phase. $\Delta_{\mathrm{sp}}(K)$ is the single-particle gap at the Dirac point while Δ_{s} is the spin gap. The staggered magnetization is given by m_{s} and its saturation value is $\frac{1}{2}$. Reprinted by permission from Macmillan Publishers Ltd: Nature (Ref. [43], `http://www.nature.com/nature/journal/v464/n7290/full/nature08942.html`), copyright (2010).

the four states per spin located exactly at the Fermi level (in the non-interacting limit) when the system size is a multiple of three. On the contrary, for sizes that are not multiples of three, we do observe a small gap. Both this gap and the peak are finite-size effects that are reduced when we increase the size of the system. We then conclude that $A(\omega)$ is zero (or very small) only at the Fermi level but without the formation of a gap. This is the signature of a semi-metallic phase. Indeed, a metal would be signaled by a persistent peak at the Fermi level (or at least a large non-zero density). The transition to the DW-SF ordered phase (without taking into account the pseudo-spin liquid phase) is signaled by the opening of the gap in $A(\omega)$ for $U/t \geq 5$, which corresponds to the value for the transition previously obtained by the finite-size scaling analysis of S_{dw}.

In comparison, Meng *et al.* also measured the single-particle gap at the Dirac point to determine if the system has left the semi-metallic region. The single-particle gap is obtained by fitting the single-particle Green's function at the Dirac

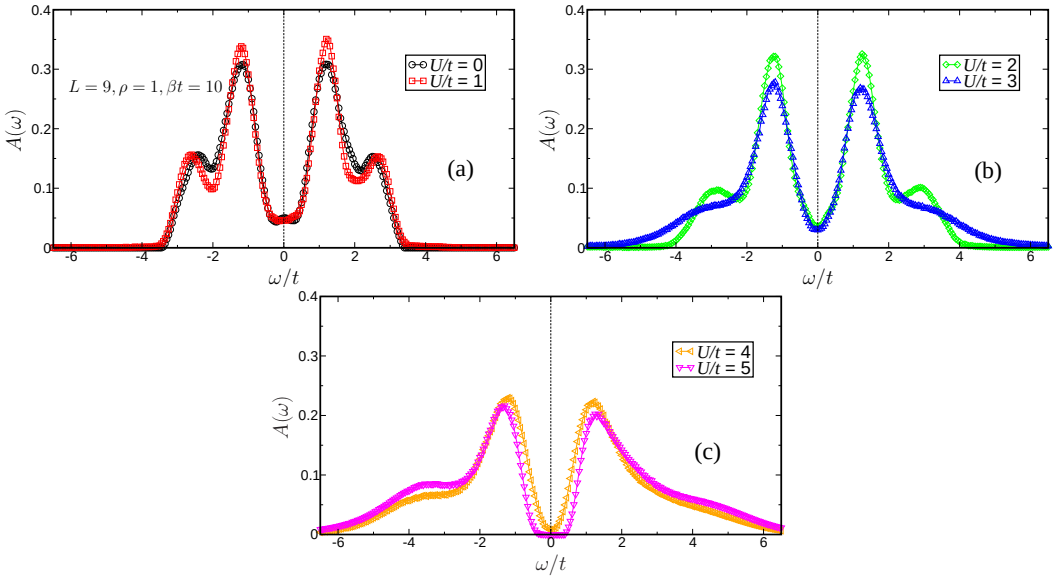

Figure 6.4: Spectral function $A(\omega)$ at half-filling ($\rho = 1$) for different values of the interaction strength U. The lattice size is $L = 9$ and $\beta t = 10$. The Fermi level is located at $\omega = 0$. For $U/t < 5$, the system is a semi-metal as witnessed by the dip around the Fermi level. The non-vanishing density of states at the Fermi level is due to finite-size effects (see Fig. 5.6). For $U/t > 5$, a gap opens as the system enters the DW-SF ordered phase. The small peaks situated at $|\omega| \approx 2.5\,t$ are also a result of finite-size effects.

point K with the formula $\mathrm{e}^{-\tau\Delta_{\mathrm{sp}}}$ and they concluded that the semi-metallic region extends up to $U \approx 3.5t$; see Fig. 6.3. They also tried to circumvent the problem of tiny metallic peak at the Fermi level that comes from finite-size effects by applying a weak vector potential through the lattice to break the degeneracy between the four states per spin at the Dirac points, hence the values of single-particle gap measured by Meng *et al.* are larger than ours[4]. They further provide evidence of a spin liquid by calculating the spin excitation gap, Δ_{s} (see Fig. 6.3) and singlet-singlet correlations (not shown). However, to obtain the spin gap (in our case, it is the pair excitation gap), we need to calculate the time-displaced pair Green's function and the calculation involved is computationally too expensive for us. Interested readers are advised to refer to Ref. [43] for their detailed findings.

[4]Lowering the temperature also has the effect of increasing the gap value, as we will see in the next section. This is because contributions to $A(\omega)$ from excited states are reduced at lower temperature.

6.4 Doping away from half-filling

6.4.1 Superfluid in doped system

At zero temperature, when the FAHM is doped away from the DW-SF ordered phase obtained at half-filling when $U > U_c$, say by increasing ρ from 1, we can crudely picture the system as applying an external magnetic field μ that couples to the z-component of the pseudo-spin in the Heisenberg model (6.27). The AF order in the z-direction is then broken and the pseudo-spins are now aligned with the z-direction with some canting angles. Assuming a classical value of $\sum_{\boldsymbol{i}} J^z_{\boldsymbol{i}}$ (determined by the density ρ), we may describe the system by an XY model of pseudo-spins, coupled antiferromagnetically in the xy-plane. We thus expect the density order to disappear and the phase coherence order to persist. However, one also expects phase coherence to be established throughout the sample when the system is sufficiently doped away from the semi-metallic phase obtained at half-filling when $U < U_c$. Indeed in this case the Fermi surface is no longer limited to isolated points and BCS pairing becomes possible. Therefore, we expect the phase coherence order to establish at zero temperature for all values of the interaction U for $\left|\delta\rho\right| = \left|\rho - 1\right|$ that are sufficiently large. With an order parameter of dimension two (a phase gradient pictured as a vector lying in the xy-plane), the system undergoes the Berezinskii-Kosterlitz-Thouless (BKT)[122–124] transition at some critical temperature T_c, leading to a quasi-long-range phase order, i.e. a superfluid phase, at $T < T_c$ before the appearance of the Bose-Einstein condensate at $T = 0$.

How about a system with its density arbitrarily close to half-filling? Due to the vanishing density of states, there might be a small region around half-filling that displays metallic behaviour when doped away from half-filling. In this case, there would be a critical doping ρ_c at small U before entering the superfluid phase (see Fig. 6.5). According to mean-field theory [125], a superconductor exists anywhere

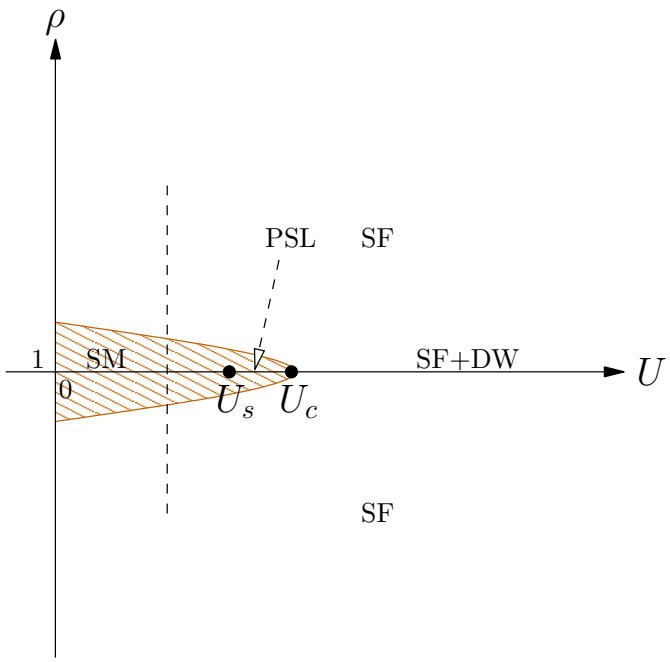

Figure 6.5: Does the FAHM supports an extended semi-metallic region? At half-filling ($\rho = 1$), there is a phase transition from a semi-metal (SM) to a pseudo-spin liquid (PSL) at an interaction strength U_s [43], then to a superfluid (SF) with density order (DW) at a critical interaction strength U_c. Away from half-filling, the system is a superfluid for $U > U_c$. However, for $U < U_c$, there might exist a small region (shaded in figure) around half-filling with metallic behaviour but is not a superfluid. The system is investigated at three different densities and at interaction strength $U = 3t < U_s < U_c$ (dashed line). DQMC results indicate that the boundary point ρ_c of this region (if it exists) at $U = 3t$ is less than 1.05. The investigation of a smaller density is computationally too expensive.

away from half-filling, albeit the superconducting gap function or, equivalently, $\langle \Delta_i^\dagger \rangle$, decays exponentially with respect to $1/(U\sqrt{\rho - 1})$ in the BCS regime, hence the shaded region in Fig. 6.5 does not exist. In their previous study [126], Su *et al.* compared DQMC results to random phase approximation (RPA) calculations and shown that there is a so-called BCS-BEC crossover extending from small to large values of the interaction when the system is off half-filling. When U is increased, the ground state of the system evolves continuously from a BCS state (where fermions with opposite spins form loose pairs of plane waves with opposite momenta) to a BEC of bosonic molecules (where fermions with opposite spin form tightly-bound pairs). We have extended their study to larger lattices (up to $L = 15$) and lower

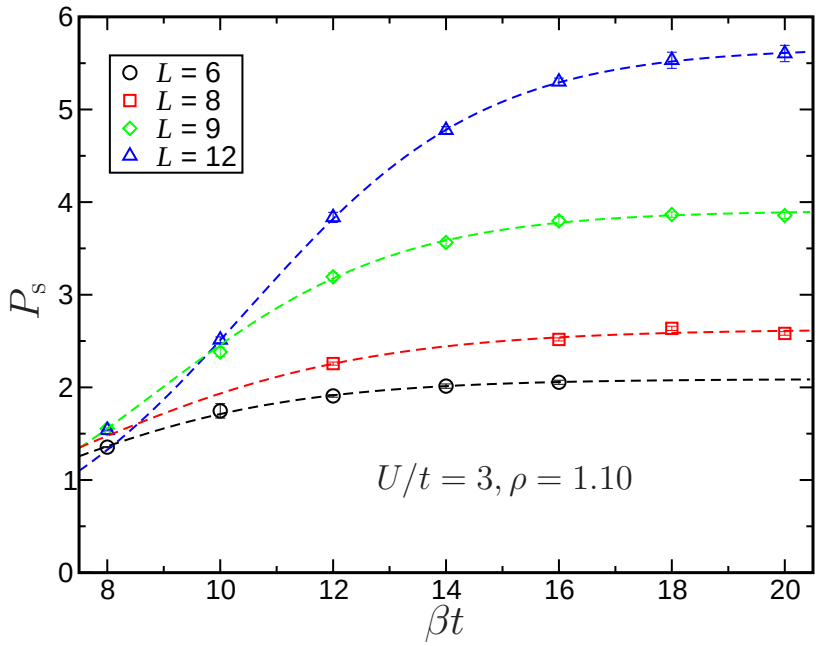

Figure 6.6: Evolution of the pair structure factor P_s as a function of the inverse temperature βt for several lattice sizes L. The interaction strength has been fixed at $U = 3t$ and the total average fermionic density at $\rho = 1.1$. The dashed lines are fits using the 3-parameter function $F(\beta t)$, Eq. (6.28). A plateau is reached when βt is much greater than the energy gap induced by finite-size effects between the ground state and the first excited state. As can be seen, the plateau is reached at larger βt when the lattice size increases. It is also reached at larger βt when $\rho \to 1$ (not shown).

temperatures (up to $\beta t = 20$) and we have also analyzed new observables. In the following, we will show that the system is a superfluid which possesses preformed pairs that develop quasi-long-range phase coherence at low temperature.

We first study the behavior of the pair and density wave structure factors, P_s and S_{dw}, away from half-filling. Since a finite lattice is used, the energy of the system is discretized with a finite energy gap ($\sim 1/L$) between the ground state and the excited states. As the temperature is decreased, these physical quantities will saturate at finite values when the ground state contributes dominantly to the thermal averages. We obtain the low-temperature limit of these quantities by decreasing the temperature until we observe a plateau signaling that we have reached the $T = 0$ limit (Fig. 6.6) and this saturation temperature decreases as

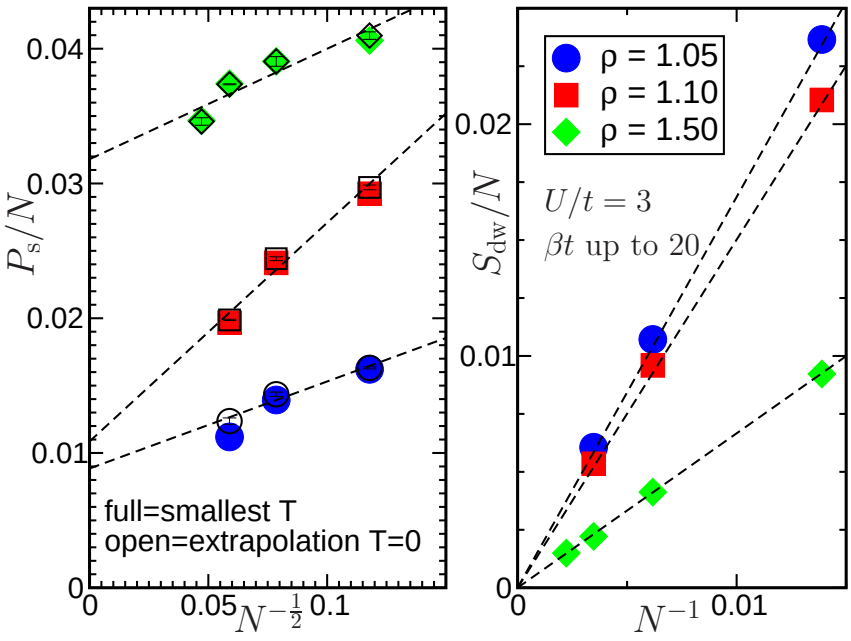

Figure 6.7: Evolution of the pair and density wave structure factors P_s and S_{dw} as a function of the number of lattice sites N for different total average fermionic densities ρ. The interaction strength has been fixed at $U = 3t$. Full symbols have been obtained for inverse temperatures up to $\beta t = 20$ (see text). Open symbols for P_s are the plateau values at $T = 0$ as extracted from the fits in Fig.6.6. The density wave structure factors S_{dw} always go to zero as the system size $L = \sqrt{N/2}$ tends to infinity whereas the phase coherence ordering signal P_s never vanishes. The dashed lines are guides to the eyes. For the same parameters at half-filling the system would be semi-metallic and S_{dw} and P_s would both vanish.

the lattice size increases. To extract the plateau value, we have used the three-parameter function

$$F(\beta t) = \frac{u}{1 + v \exp(-w\beta t)} \tag{6.28}$$

to fit our numerical data $P_s(\beta t)$. The plateau value $\lim_{\beta\to\infty} P_s$ is then approximated by u. We have also observed in our numerical simulations that this plateau is reached at lower and lower temperatures as we approach half-filling. This is because the BKT critical temperature T_c goes to zero like $1/|\ln \delta\rho|$ as $\delta\rho = |1 - \rho| \to 0$ [141] and lower temperatures are required to achieve phase coherence.

Figure 6.7 shows how P_s and S_{dw} scale with the number of lattice sites N. For each chosen lattice size L and fermionic density ρ, we have run our simulations for

the lowest temperature that could be numerically achieved. The temperature range that we have been able to explore was up to $\beta t = 20$. As expected $S_{\rm dw}$ always goes to zero and $P_{\rm s}$ always extrapolates to a non-zero value. We may then conclude, from direct measurement, that the BEC at zero temperature always appears as soon as the system is doped away from half-filling. Even with the smallest doping that we have been studying ($\rho = 1.05$, 5% doping), we have observed a clear persistence of the phase coherence ordering in the large-size limit.

6.4.2 Pair formation in the doped system

To observe the molecule formation along the BCS-BEC crossover, we have studied the density of on-site pairs

$$\rho_{\rm p} = \frac{1}{N} \sum_i \langle n_{i\uparrow} n_{i\downarrow} \rangle. \tag{6.29}$$

In the non-interacting limit ($U/t \to 0$), spin-up and spin-down particles are uncorrelated. Hence $\langle n_{i\uparrow} n_{i\downarrow} \rangle = \langle n_{i\uparrow} \rangle \langle n_{i\downarrow} \rangle = \rho_\uparrow \rho_\downarrow$. Since we consider here equal spin populations $\rho_\uparrow = \rho_\downarrow = \rho/2$, we find $\rho_{\rm p} = \rho_\uparrow^2$. In the molecular limit ($U/t \to \infty$), fermions can only exist in pair at a site. Hence $\langle n_{i\uparrow} n_{i\downarrow} \rangle = \langle n_{i\uparrow} \rangle = \rho_\uparrow$ and $\rho_{\rm p} = \rho_\uparrow$. In Fig. 6.8, we have plotted the rescaled density of on-site pairs:

$$\tilde{\rho}_{\rm p} = \frac{\rho_{\rm p} - \rho_\uparrow^2}{\rho_\uparrow - \rho_\uparrow^2}. \tag{6.30}$$

as a function of U/t. The crossover between a regime of loosely-bound pairs and a regime of more tightly-bound pairs (molecules) is nicely evidenced by the smooth evolution of this rescaled quantity between the two limits $\tilde{\rho}_p = 0$ and $\tilde{\rho}_p = 1$ as the interaction is increased. For the intermediate values of the interactions used in our simulation, we see that the pairs are not tightly-bound yet. The $\tilde{\rho}_p = 1$ limit is obtained only for extremely large values of U/t.

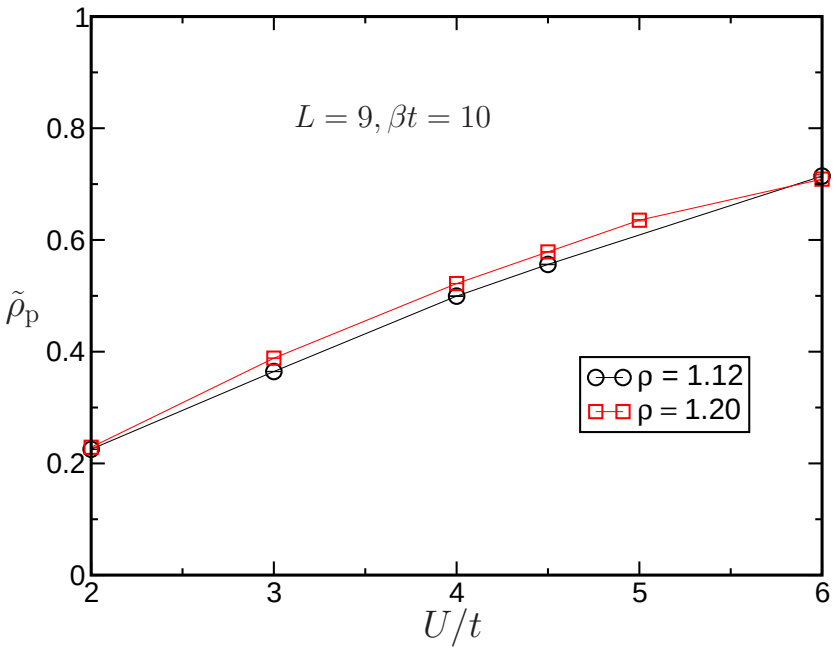

Figure 6.8: Evolution of the rescaled density $\tilde{\rho}_p$ of on-site pairs, Eq. (6.30), as a function of the interaction strength U/t for two different total average fermionic densities ρ. The system size has been fixed at $L = 9$ and the inverse temperature is $\beta t = 10$. In the non-interacting limit ($U/t \to 0$), spin-up and spin-down particles are uncorrelated, hence $\langle n_{i\uparrow} n_{i\downarrow} \rangle = \langle n_{i\uparrow} \rangle \langle n_{i\downarrow} \rangle = \rho_\uparrow \rho_\downarrow = \rho_\uparrow^2$ for equal spin populations. In this case $\tilde{\rho}_p = 0$. In the molecular limit ($U/t \to \infty$), fermions can only exist in pair at a site, hence $\langle n_{i\uparrow} n_{i\downarrow} \rangle = \langle n_{i\uparrow} \rangle = \rho_\uparrow$. In this case $\tilde{\rho}_p = 1$.

The second evidence for molecule formation along the BEC-BCS crossover comes from the evolution of the spectral function $A(\omega)$ when the interaction strength U (Fig. 6.9) and the temperature T (Fig. 6.10) are varied. At large interactions ($U \geq 4$), a clear gap is found at the Fermi level $\omega = 0$ provided the temperature is low enough, showing the formation of molecules. On the contrary, when the interaction is weaker ($U \leq 3$), the gap does not open within the same range of temperatures. However, we observe that the value of $A(\omega)$ at the Fermi level $\omega = 0$ decreases when the temperature is lowered (Fig. 6.10). We interpret this behavior as the precursor to the formation of a small BCS gap at very low temperatures. This dip in $A(\omega)$ at the Fermi level is different from the one due to the vanishing of the non-interacting density of states at the Dirac points that

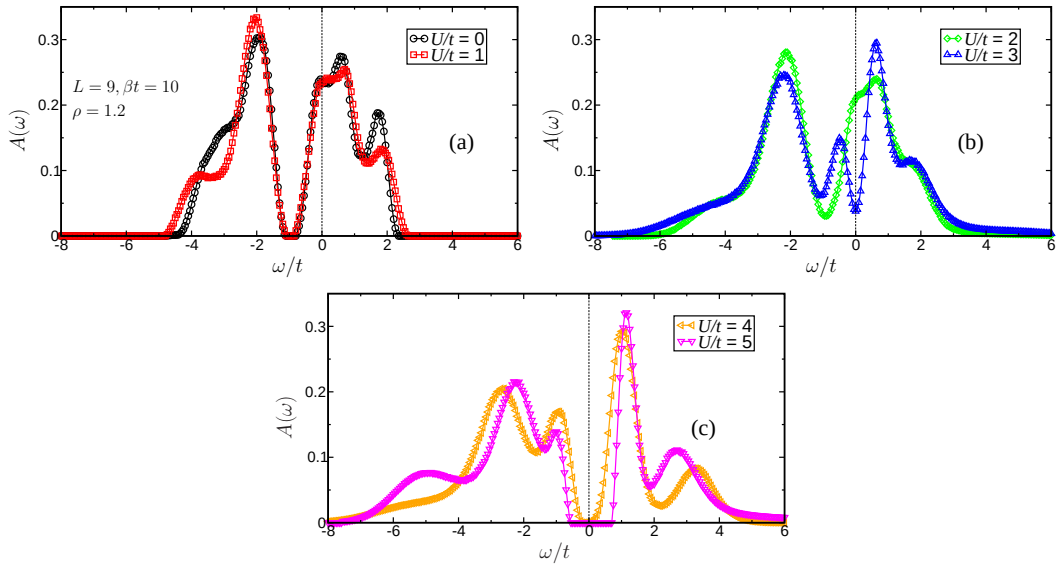

Figure 6.9: Evolution of the spectral function $A(\omega)$ as a function of the interaction strength U at density $\rho = 1.2$, inverse temperature $\beta t = 12$ and lattice size $L = 9$. When $U = 0$, the chemical potential is numerically found to be $\mu/t = 0.8768$, locating the Dirac points in the residual gap (due to finite-size effects and temperature rounding) around $\omega/t = -1$. The fact that the density of states vanishes linearly with ω around $\omega/t = -1$ also supports this identification of the location of the Dirac points. As U is increased, a dip develops in the spectral function at the Fermi level (located at $\omega = 0$) and the BCS-BEC gap eventually opens while the Dirac points are gradually destroyed.

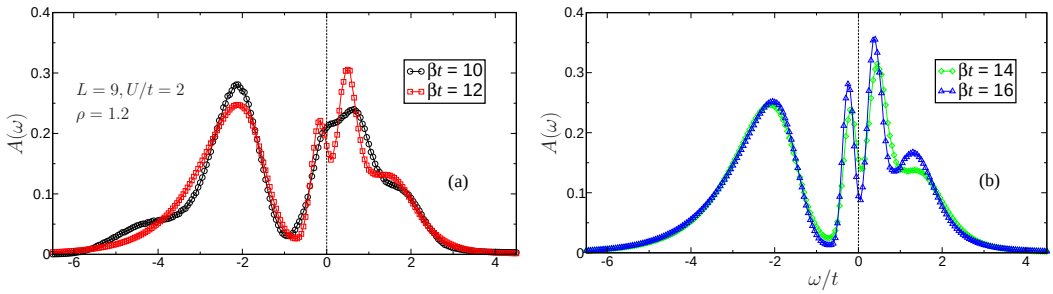

Figure 6.10: Evolution of $A(\omega)$ as a function of inverse temperature βt at $\rho = 1.2$, interaction strength $U = 2t$ and lattice size $L = 9$. As the temperature is lowered, a dip develops in the spectral function at the Fermi level located at $\omega = 0$. Eventually a gap opens when the temperature is low enough (not shown). The gap opening at the Fermi level is obtained even at weak interactions, a situation characteristic of the existence of a small BCS gap.

was observed at half-filling in the semi-metal case. The Dirac dip is still present in the $U \leq 3$ cases for $\omega < 0$ (Fig. 6.9), showing that the interaction strength is not large enough to strongly modify the structure of the Fermi sea, except very close

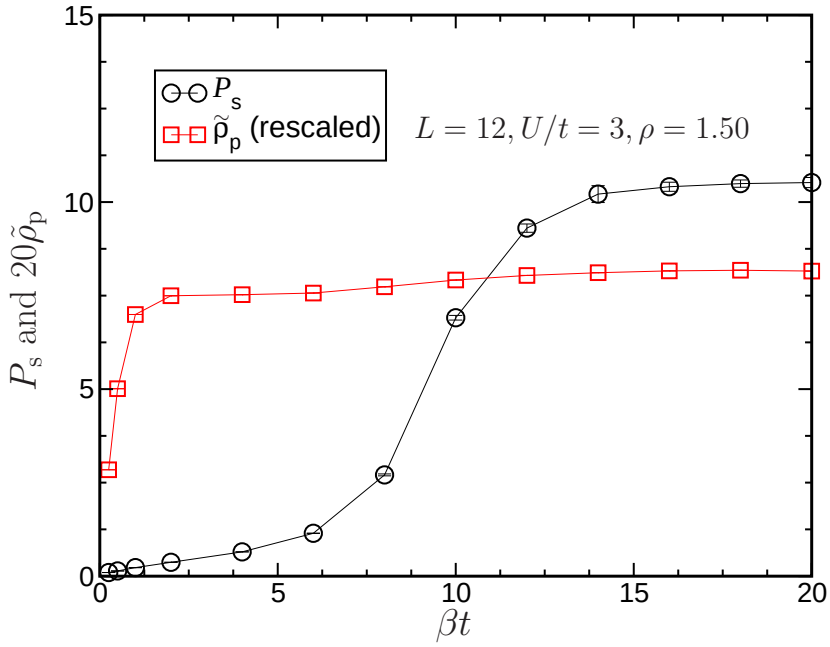

Figure 6.11: Evolution of the pair structure factor P_s (circles) and the rescaled density of on-site pairs $\tilde{\rho}_p$ (squares) as a function of the inverse temperature βt at interaction strength $U = 3t$. The total average fermionic density is set at $\rho = 1.5$ and the system size is $L = 12$. Two different energy scales are clearly identified as P_s, signaling the emergence of phase coherence, saturates at $\beta t \approx U/t$ whereas $\tilde{\rho}_p$, signaling the molecule formation, saturates at $\beta t \approx t/U$. We recover here (in dimensionless units) the two energy scales t^2/U and U, typical of the emergence of phase coherence and of the formation of tightly-bound pairs.

to the Fermi level. This is characteristic of the BCS case. On the other hand, the Dirac dip disappears at strong interactions (Fig. 6.9, bottom), showing now that the original Fermi sea structure has been completely modified by the interaction.

6.4.3 Pair phase coherence and temperature scales in doped system

A nice feature of the strongly-interacting regime is the existence of two very different energy scales. One corresponds to the formation of bound pairs (molecules) and is typically of the order of U itself. The second corresponds to the emergence of phase coherence between these pairs and is of the order of the hopping parame-

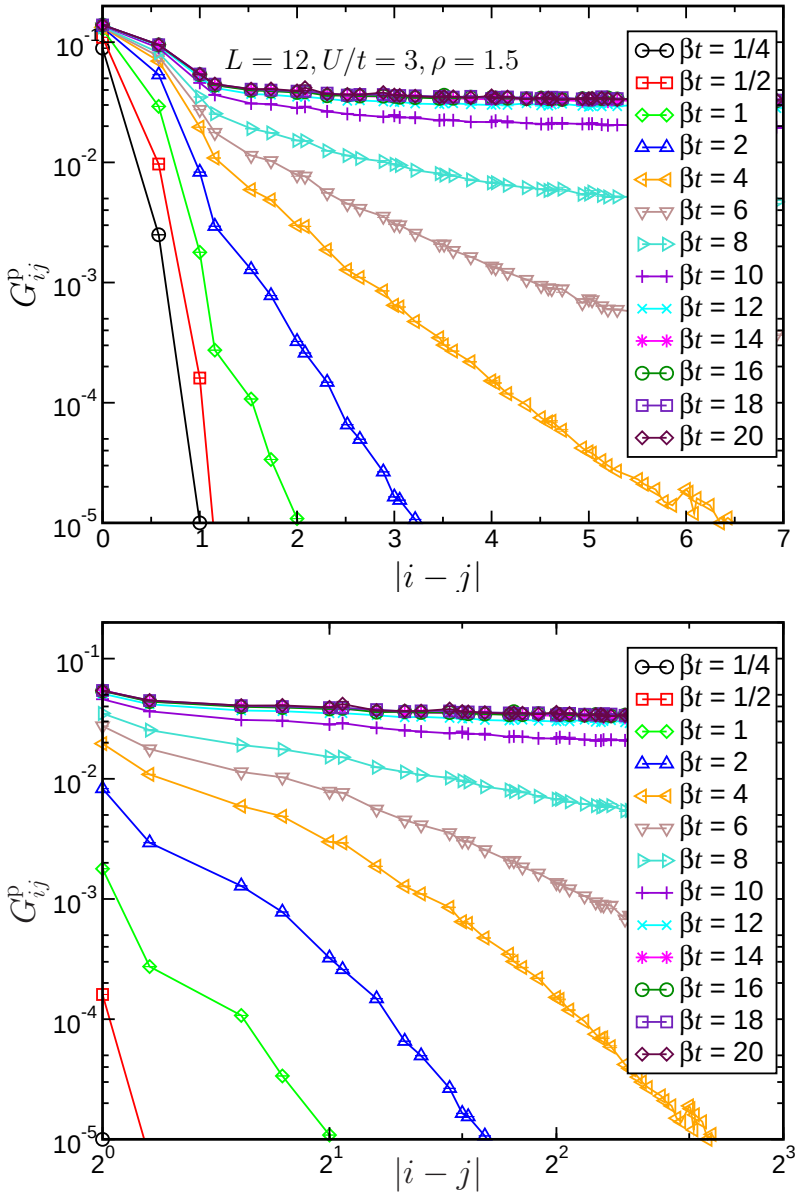

Figure 6.12: Evolution of the pair Green's function as a function of distance for different temperatures. The total average fermionic density is set at $\rho = 1.5$, the interaction strength at $U = 3t$ and the lattice size is $L = 12$. The vertical axes are plotted in logarithmic scale while the horizontal axes are plotted with linear (left) and logarithmic (right) scales. For large site separation $|i - j|$, we observe a transition from an exponential decay (linear behavior in the log-linear plot) at high temperature to a weak algebraic decay (linear behavior in the log-log plot) at low temperature. This is the signature of the BKT transition where the system leaves the disordered phase to enter a phase with quasi-long-range order as the temperature is lowered. However, due to the limited system size, the weak algebraic decay of the pair Green's function is difficult to infer unambiguously.

ter for pairs, typically t^2/U [138]. These two energy scales are clearly identified by comparing the evolution of $P_{\rm s}$ and $\rho_{\rm p}$ when the temperature is varied, see Fig. 6.11. We thus can conclude that, even if the pairs are not tightly-bound at the intermediate values of U/t we used (as it shown in Fig. 6.11), we clearly observe the formation of pairs before the emergence of phase coherence, which is expected in the BEC regime. To investigate this phenomenon further, we show in Fig. 6.12 the pair Green's function (5.16) as a function of distance for different temperatures. There is a range of temperatures ($0.1 < \beta t < 5$) where the pair Green's function is clearly decreasing exponentially with distance (up to some boundary effects). This means that no phase coherence is achieved and the system is in a disordered regime. In other words, the corresponding temperatures are above the BKT transition temperature T_c. For this same temperature range, $\rho_{\rm p}$ has already reached its zero-temperature limit (Fig. 6.11). This is clear evidence for the existence of preformed pairs which will eventually develop quasi-long-range phase coherence at a much lower temperature. For temperatures $T < T_c$, the Green's function should decay algebraically with distance with an exponent $\eta = T/(4T_c)$ [141]. For $\beta t \geq 10$, the pair Green's function behavior is consistent with a power-law decay, but it is difficult to extract the corresponding exponent due to finite-size effects.

6.5 Summary

We have shown that the coexistence of superfluid and density order at half-filling is a result of pseudo-spin symmetry and confirmed it by Monte Carlo results. We found that the system enters a phase superfluid and density wave at interaction strength $U \approx 5t$. However, Meng *et al.* found that the critical strength is lower (at $U \approx 4.3t$). We attributed the discrepancy to the high temperature at which our results were computed. Meng *et al.* also found (in a repulsive model) a spin

liquid phase before the transition into antiferromagnetic Mott insulator, but the relevant quantity (time-displaced pair Green function in the attractive model) is computationally too expensive for us. Doping away from half-filling, the system appears as superfluid without density wave at a doping as low as 5%. Spectral functions extracted with the MaxEnt method indicate the formation of a BCS gap at the Fermi level as the temperature is lowered at a given interaction strength, or as the interaction strength is increased at a given temperature. The presence of a superfluid is also confirmed by the power-law decay of pairing correlation below a certain temperature, which is a signature of the BKT transition. Above the transition temperature, we have demonstrated formation of on-site pairs without long-range coherence. Two temperature scales are thus observed, involving pair formation and pair phase coherence, respectively.

Chapter 7

Conclusions

Motivated by the current active research in graphene physics, we have explained and analyzed how to reproduce massless Dirac fermions by loading ultracold fermionic atoms into an optical lattice with honeycomb structure. We described the simplest possible laser configuration that gives rise to an optical potential where field minima are organized in a honeycomb structure and we have thoroughly detailed the corresponding crystallographic features. The band structure of a perfect honeycomb lattice displays two conical degeneracies located at the corners of the first Brillouin zone, as dictated by symmetry.

When the lattice is loaded with fermions at half-filling, the Fermi level cuts the energy band precisely at these degeneracy points known as the *Dirac points*. Around half-filling, we can cast the tight-binding Hamilton operator into a form reminiscent of the Weyl-Dirac Hamilton operator that governs the dynamics of massless Dirac fermions. We evaluate the important parameter of the tight-binding model, the tunneling amplitude t between nearest neighbors in the terms of an effective Planck's constant of the problem, $\hbar_e = \sqrt{2E_R/V_0}$ (with V_0 the optical potential strength and E_R the recoil energy). A semi-classical evaluation of t agrees well with an exact numerical calculation of the band spectrum in the tight-

binding limit. From this, we derive the required temperature to reach the Dirac fermion regime to be in the micro Kelvin range.

In view of the impossibility of controlling the experimental parameters with infinite precision, we examined the robustness of massless Dirac fermions to imperfections of the laser configurations, e.g. field strength imbalance and mis-alignment of the laser beams. The massless Dirac fermions turn out to be quite robust as the equality of the beam intensities should be controlled within the few percent range while the respective beam angles should equal $2\pi/3$ within the few degrees range. By appropriately controlling these lattice distortions, one can even move the Dirac points around in the Brillouin zone and modify the group velocity of Dirac fermions in certain directions.

A great advantage of the honeycomb optical lattice over the real graphene is our ability to tune the interactions between fermionic atoms through Feshbach resonance. We studied the Hubbard model with on-site interactions to describe the physics of these atoms trapped in the optical lattice. In particular, we investigated the attractive regime and showed that there is a quantum phase transition at $T = 0$ between a disordered phase and a DW-SF phase exhibiting crystalline as well as superfluid orders. The critical interaction strength at which this QPT takes place is bounded by $5.0 \leq U_c/t \leq 5.1$. We have also shown that, before the transition, the system is semi-metallic and that the interactions do not markedly change the nature of this phase. We compared our results with the work by Meng *et al.* that was published recently. We attributed the discrepancy in the critical interaction strength to the relatively high temperature at which our results were obtained. We also missed the pseudo-spin liquid phase found by Meng *et al.*, as we did not calculate the time-displaced pair Green's function. Such a calculation would be computationally demanding for us. Away from half-filling, within our numerical accuracy, the system seems to become superfluid even for doping as low as 5%. We

show four pieces of evidence to support this identification: (1) a finite-size analysis of the pair structure factor P_{s}, (2) the existence of two different energy scales for strong enough interactions, one for pair formations ($\sim U$ since it is the cost to break a pair) and one for establishing phase coherence of pairs ($\sim t^2/U$ since it is the cost for a pair to hop in the XY pseudo-spin model), (3) the formation of a BCS gap at the Fermi level, and (4) the exponential decay of the pair Green's function above the BKT transition temperature and a power-law decay below it.

At strong interactions, the presence of the DW-SF phase can be understood as a consequence of the effective model at half-filling being the Heisenberg pseudo-spin model with antiferromagnetic coupling. For weak interactions, both at and away from half-filling, we have observed that the spectral function $A(\omega)$ is qualitatively the same as in the non-interacting case. Only the states close to the Fermi level are affected by these weak interactions. As there are no available states in the half-filled case close to the Fermi level, the interactions hardly play a role and the system remains a semi-metal (at half-filling) up to $U = 3.5t$ (value from Meng *et al.*). For larger interaction strength, the system enter a pseudo-spin liquid phase with a resonating valence bond picture. It costs energy in making both a single-particle excitation and a pair excitation and there is no long-range pair phase coherence in such a system. When the interactions are very strong, tightly-bound pairs form and the system enters a different phase. In this case, the description in terms of individual fermions and plane-wave states is no longer relevant.

Currently, there is a lack of experimental evidence to confirm our theoretical findings on the Hubbard model. The closest material is graphene, with an estimated repulsive interaction strength of $3.6t$ based on experimental values from polyacetylene [10, 39], which amounts to a single point on the phase diagram. At room temperature, we have $\beta t \approx 100$ in graphene, an inverse temperature five times larger than the largest βt that we have simulated. So far, graphene is found

to display a semi-metallic behaviour, which agrees with our Monte Carlo results for half-filled lattice at $U < 5t$. Since many graphene phenomena can be explained using non-interacting massless Dirac fermions, and since our results on spectral functions show that the spectral function $A(\omega)$ varies linearly with ω at half-filling (a characteristic of single-particle excitations being massless Dirac fermions), it is thus possible that the properties of the half-filled honeycomb lattice before the phase transition at $U \approx 5t$ can be explained with a Fermi-liquid type theory. Even though many people have already worked on such a theory (or other related theories) [40, 142–145], we have yet to obtain conclusive evidence on the Fermi-liquid / non-Fermi-liquid / marginal Fermi-liquid properties of graphene.

Another interesting property of graphene is its DC and AC conductivity. The minimal DC conductivity was first reported as a universal value independent of sample and temperature [4, 11]. Various attempts were made to explain this minimal value as a characteristics of ideal lattice without any scattering processes, including explanation based on *Zitterbewegung* of relativistic Dirac fermions (see Ref. [9] and references therein.) and extrapolation of AC conductivity to zero frequency limit [146]. However, another experimental report has cast doubt on the universality of the minimal DC conductivity [147]. On the other hand, the dynamical or AC conductivity is comparatively well understood [15, 148, 149]. There is a universal background value of the order of e^2/h at small frequency that can be accounted for by interband transitions and this universal value has been confirmed experimentally [93]. When interactions between fermions are present, using the BCS picture, we found that there are additional intraband contributions to the dynamical conductivity when the interacting system is away from half-filling. There is again a difficulty in obtaining experimental data for comparison, since the electrons in graphene appear to be interacting repulsively, while conductivity is a quantity that has not been measured in cold atom experiments. Recently,

there was experimental realization of synthetic electric and magnetic fields acting on neutral atoms [150, 151]. This was achieved by coupling different magnetic sublevels through Raman processes to produce spatially-dependent or time-depedent effective vector potential. This experimental success indicates that we are a step closer to the experimental verification of our theoretical results and we may gain further understanding into the physics of fermions in a honeycomb lattice.

Other novel physics in a honeycomb lattice that might be produced using cold atom experiments include exotic pairing in fermionic population with spin imbalance and Anderson localization with disordered potential. Our group has started theoretical works in these directions and we hope that our findings will shed light on the physics involved.

In conclusion, trapping ultracold fermions in an optical lattice offers a better tool than graphene to explore the fundamental physics of a honeycomb lattice. There are certain technological barriers to be overcome, e.g. it is harder to reach the relevant temperature for observing the interesting physics in cold atom experiments, but we believe that this is just a matter of time. With the combined experimental results on graphene and cold atoms, we should have a better understanding of the physics of spin-1/2 fermions in a honeycomb lattice.

Appendix A

Symmetry

A.1 Labeling of energy eigenstates through symmetry

To show that we can label an energy eigenstate by eigenvalues of some symmetry operators, we note that a symmetry operator $\mathcal{G}$ that leaves H invariant implies that they commute,

$$\mathcal{G}H\mathcal{G}^{-1} = H \Rightarrow \mathcal{G}H = H\mathcal{G}. \tag{A.1}$$

Choosing the eigenfunctions of $\mathcal{G}$ as the basis, we can express the matrix representation of the above relation as

$$\sum_j \mathcal{G}_{ij}H_{jk} = \sum_j H_{ij}\mathcal{G}_{jk}. \tag{A.2}$$

Since $\mathcal{G}$ is diagonal in the given basis, we are left with the relation

$$(\mathcal{G}_{ii} - \mathcal{G}_{kk})H_{ik} = 0. \tag{A.3}$$

If $\mathcal{G}_{ii} \neq \mathcal{G}_{kk}$, the ith state and the kth state belong to different symmetries and H_{ik} must be equal to zero. Hence, there are no off-diagonal matrix elements of H that connects states of different symmetries.

A.2 Eigenvalues of translation operators

To obtain the eigenvalues of the translation operators of a triangular lattice, let us first consider the simplest case of a one-dimensional lattice along x-direction with L sites and periodic boundary conditions. The translation operators are

$$T_{\boldsymbol{R}} = \mathrm{e}^{-\frac{\mathrm{i}}{\hbar}pna} \quad \text{with } n = 0, 1, \ldots, L-1, \tag{A.4}$$

where p is the 1D momentum operator and a is the lattice spacing between two neighboring sites. Due to the periodicity of the lattice, we know that under L translations, a particle will return to its original position, hence

$$T_{\boldsymbol{R}}^{L} = 1 \tag{A.5}$$

and the eigenvalues of $T_{\boldsymbol{R}}$ are the L-th roots of unity, i.e.

$$\mathrm{e}^{-\mathrm{i}\frac{2\pi m}{L}} \quad \text{with} \quad m = 0, 1, \ldots, L-1. \tag{A.6}$$

To express this result in the conventional notation used in solid-state physics, we write it as

$$\mathrm{e}^{-\mathrm{i}\frac{2\pi m}{L}} = \mathrm{e}^{-\mathrm{i}\frac{2\pi}{a}\frac{m}{L}a} = \mathrm{e}^{-\mathrm{i}ka}, \tag{A.7}$$

where $k = 0, \frac{2\pi}{La}, \cdots, \frac{2\pi(L-1)}{La}$ and $\boldsymbol{k} = k\boldsymbol{e}_x$ is a wave vector that labels a single-particle quantum state. In the limit $L \to \infty$, $0 \leq k < \frac{2\pi}{a}$ and $\boldsymbol{b} = \frac{2\pi}{a}\boldsymbol{e}_x$ is the primitive vector of the reciprocal lattice. The eigenvalues of the trans-

lation operators remain unchanged if the wave vector is translated through $\boldsymbol{b}$, i.e. $\boldsymbol{k} \rightarrow \boldsymbol{k} + \boldsymbol{b}$, hence we can redefine the range of k to be $-\frac{\pi}{a} \leq k < \frac{\pi}{a}$. This is just the 1st BZ of the 1D lattice. The definition of the wave vectors can be generalized to a 2D lattice by finding the two linearly independent primitive vectors $\boldsymbol{b}_i$ of the reciprocal lattice that satisfy the relation

$$\boldsymbol{a}_i \cdot \boldsymbol{b}_j = 2\pi\delta_{ij}, \quad \text{for} \quad i, j = 1, 2. \tag{A.8}$$

A.3 Analytical expression of density of states

We follow closely here the derivation given in Ref. [62]. In the thermodynamic limit ($N_c \rightarrow \infty$), Eq. (2.42) can be written as

$$\rho(\mathcal{E}) = \frac{1}{4\pi^2} \sum_{s=\pm} \int_0^{2\pi} dx \int_0^{2\pi} dy \; \delta(s\sqrt{3 + 2\cos x + 2\cos y + 2\cos(x+y)} - \mathcal{E}). \tag{A.9}$$

However, it is easier to calculate the number of frequencies whose squared-values lie between $\mathcal{E}^2$ and $\mathcal{E}^2 + d(\mathcal{E}^2)$, i.e. we seek the frequency distribution $g(\mathcal{E}^2)d(\mathcal{E}^2)$ such that $\rho(\mathcal{E}) = 2|\mathcal{E}|g(\mathcal{E}^2)$. We thus have

$$\begin{aligned}
g(\mathcal{E}^2) &= \lim_{N_c \rightarrow \infty} \frac{1}{N_c} \sum_{\boldsymbol{k}} \delta\left((\epsilon_{+,\boldsymbol{k}}/t)^2 - \mathcal{E}^2\right) \\
&= \frac{1}{4\pi^2} \int_0^{2\pi} dx \int_0^{2\pi} dy \; \delta(3 + 2\cos x + 2\cos y + 2\cos(x+y) - \mathcal{E}^2) \\
&= \frac{1}{\pi^2} \int_0^{\pi} d\theta \int_0^{\pi} d\phi \; \delta(1 + 4\cos\phi\cos 2\theta + 4\cos^2 2\theta - \mathcal{E}^2) \\
&= \frac{2}{\pi^2} \int_{-1}^{1} du \int_{-1}^{1} dv \; \frac{\delta(1 + 4uv + 4u^2 - \mathcal{E}^2)}{2\sqrt{1-u^2}\sqrt{1-v^2}} \\
&= \frac{1}{\pi^2} \int_{-1}^{1} du \frac{I(u, \mathcal{E}^2)}{\sqrt{1-u^2}},
\end{aligned} \tag{A.10}$$

where

$$I(u,\mathcal{E}^2) = \int_{-1}^{1} dv \frac{\delta(1+4uv+4u^2-\mathcal{E}^2)}{\sqrt{1-v^2}} = \int_{u(u-1)}^{u(u+1)} dz \frac{\mathrm{sgn}(u)\delta(1+4z-\mathcal{E}^2)}{\sqrt{(z-u(u-1))(u(u+1)-z)}} \text{ with } z = u(u+v). \tag{A.11}$$

In the third line of Eq. (A.10), we have employed the substitutions,

$$\begin{aligned} x &= 2\theta + \phi, \\ y &= 2\theta - \phi, \end{aligned} \tag{A.12}$$

where $0 \leq \theta, \phi \leq \pi$. In the fourth line, the factor of two comes from the fact that $\cos 2\theta$ is even with respect to $\theta = \pi/2$ and we continue to make the substitutions

$$\begin{aligned} u &= \cos 2\theta, \\ v &= \cos \phi. \end{aligned} \tag{A.13}$$

The integral (A.11) is of the form

$$J = \int_a^b dz\ \delta[p(z)]f(z) \tag{A.14}$$

and it can be evaluated following Ref. [62]. This is done by defining $w = p(z)$ and the solution $z = q(w)$ such that $dz = q'(w)dw$ where $q'(w) = dq(w)/dw$. Finally, the defining property of Dirac delta function,

$$\int_\beta^\alpha dw\ \delta(w)F(w) = \begin{cases} F(0), & \alpha\beta < 0 \\ 0 & \text{otherwise} \end{cases} \tag{A.15}$$

yields

$$J = \begin{cases} f\left(q(0)\right) q'(0), & p(a)p(b) < 0 \\ 0. & \text{otherwise} \end{cases} \tag{A.16}$$

Hence, to relate to our quantities in Eq. (A.11), we have

$$\begin{aligned} a &= \begin{cases} u(u-1) \text{ for } u > 0, \\ u(u+1) \text{ for } u < 0, \end{cases} \\ b &= \begin{cases} u(u+1) \text{ for } u > 0, \\ u(u-1) \text{ for } u < 0, \end{cases} \\ q(w) &= \frac{1}{4}[w - (1-\mathcal{E}^2)], \\ p(z) &= 1 + 4z - \mathcal{E}^2 = 4[z - q(0)], \\ f(z) &= \frac{1}{\sqrt{(z-a)(b-z)}} \end{aligned} \tag{A.17}$$

and

$$I(u, \mathcal{E}^2) = \begin{cases} \frac{1}{4\sqrt{[q(0)-a][b-q(0)]}}, & [q(0)-a][b-q(0)] > 0 \\ 0. & \text{otherwise} \end{cases} \tag{A.18}$$

If we further define $\xi = u^2$, we can write $[q(0)-a][b-q(0)]$ as $(\lambda_+ - \xi)(\xi - \lambda_-)$, where

$$\lambda_\pm = \frac{1}{2}\Big(\frac{|\mathcal{E}|^2+1}{2} \pm |\mathcal{E}|\Big) = \frac{(|\mathcal{E}| \pm 1)^2}{4}. \tag{A.19}$$

To further evaluate $g(\mathcal{E}^2)$, we need the identity (see Eq. 574 from Ref. [152]),

$$\int_\gamma^\beta \frac{dx}{\sqrt{(\alpha-x)(\beta-x)(x-\gamma)x}} = \frac{2}{\sqrt{(\alpha-\gamma)\beta}} F\left(\frac{\pi}{2}, \sqrt{\frac{\beta-\gamma}{\alpha-\gamma}\frac{\alpha}{\beta}}\right) \tag{A.20}$$

where $\alpha \geq \beta \geq \gamma \geq 0$ and $F(\pi/2, k)$ is the complete elliptical integral of the first kind. For $|\mathcal{E}| \leq 1$, we have $1 \geq \lambda_+ \geq \lambda_- \geq 0$ while we have $\lambda_+ \geq 1 \geq \lambda_- \geq 0$ when $1 \leq |\mathcal{E}| \leq 3$. If we now let $Z_0 = 4\beta(\alpha-\gamma)$ and $Z_1 = 4\alpha(\beta-\gamma)$, then

Z_0 and Z_1 are given by the expression (2.44) for the defined range. Substituting Eqs. (A.18) and (A.20) into Eq. (A.10), and noting the change of integration limits, $\int_{-1}^{1} du \to \int_{0}^{1} \frac{d\xi}{\sqrt{\xi}}$, we finally arrive at

$$g(\mathcal{E}^2) = \frac{1}{\pi^2\sqrt{Z_0}} F\left(\frac{\pi}{2}, \sqrt{\frac{Z_1}{Z_0}}\right) \tag{A.21}$$

and

$$\rho(\mathcal{E}) = \frac{2}{\pi^2}\frac{|\mathcal{E}|}{\sqrt{Z_0}} F\left(\frac{\pi}{2}, \sqrt{\frac{Z_1}{Z_0}}\right). \tag{A.22}$$

Appendix B

Interactions

B.1 Strong coupling limit at half-filling

We consider a half-filled lattice with N pairs of fermions. The projectors P_l onto the subspace with exactly l doubly-occupied sites can be generated by expanding the Gutzwiller projector

$$\Pi(x) = \prod_{\boldsymbol{i}} [1 - (1-x) n_{\boldsymbol{i}\uparrow} n_{\boldsymbol{i}\downarrow}] = \sum_{l=0}^{N} x^l P_l, \tag{B.1}$$

where the variational parameter x ranges from 0 (forbidding double occupancy) to 1 (leaving state unchanged). A projector can be easily extracted by an appropriate number of differentiation of $\Pi(x)$ with respect to x followed by setting x to zero. For example, setting $x = 0$ in $\Pi(x)$ immediately gives the projector onto the subspace with zero doubly-occupied sites, $P_0 = \prod_{\boldsymbol{i}} [1 - n_{\boldsymbol{i}\uparrow} n_{\boldsymbol{i}\downarrow}]$. We consider two specific projectors: $P_{N/2}$ that projects onto the subspace with exactly $N/2$ doubly-occupied sites and $P_\eta \equiv \sum_{l \neq \frac{N}{2}} P_l$ that projects onto the subspace with at least one broken pair, such that

$$P_{N/2} + P_\eta = \mathbb{1}. \tag{B.2}$$

Using Eq. (B.2), we can rewrite the Hamilton operator as

$$H = \underbrace{P_{N/2} H P_{N/2} + P_\eta H P_\eta}_{H_0} + \underbrace{P_{N/2} H P_\eta + P_\eta H P_{N/2}}_{H_\eta}. \tag{B.3}$$

We now seek a canonical transformation to eliminate the effect of H_η to the lowest order so as to remove non-diagonal elements that connect the two subspaces. This is carried out by first defining

$$H(\lambda) = H_0 + \lambda H_\eta, \tag{B.4}$$

then looking for the canonical transformation of the form

$$\mathcal{U}(\lambda) = e^{\mathrm{i}\lambda\mathcal{S}}, \;\; \mathcal{S} = \mathcal{S}^\dagger \tag{B.5}$$

such that the transformed Hamilton operator $H_{\text{eff}}(\lambda)$ obeys

$$H_{\text{eff}}(\lambda) = e^{\mathrm{i}\lambda\mathcal{S}} H(\lambda) e^{-\mathrm{i}\lambda\mathcal{S}} = H_0 + \lambda^2 H' + \mathcal{O}(\lambda^3). \tag{B.6}$$

In the end, we set $\lambda = 1$. In this sense, λ is just a bookkeeping device, not an expansion parameter of any sort. Expanding Eq. (B.6), we have

$$H_{\text{eff}}(\lambda) = H_0 + \lambda(H_\eta + \mathrm{i}[\mathcal{S}, H_0]) + \lambda^2 \left(\mathrm{i}[\mathcal{S}, H_\eta] + \frac{1}{2}[\mathcal{S}, [H_0, \mathcal{S}]] \right) + \mathcal{O}(\lambda^3), \tag{B.7}$$

and $\mathcal{S}$ is determined by cancelling the linear term:

$$[H_0, \mathcal{S}] + \mathrm{i} H_\eta = 0. \tag{B.8}$$

Setting $\lambda = 1$, we obtain

$$H_{\text{eff}} = H_0 + \frac{\mathrm{i}}{2}[\mathcal{S}, H_\eta]. \tag{B.9}$$

H_K terms	Initial state				Final state			
	$\boldsymbol{i\bar{\sigma}}$	$\boldsymbol{i\sigma}$	$\boldsymbol{j\sigma}$	$\boldsymbol{j\bar{\sigma}}$	$\boldsymbol{i\bar{\sigma}}$	$\boldsymbol{i\sigma}$	$\boldsymbol{j\sigma}$	$\boldsymbol{j\bar{\sigma}}$
$(1-n_{i\bar{\sigma}})f^\dagger_{i\sigma}f_{j\sigma}(1-n_{j\bar{\sigma}})$	0	0	1	0	0	1	0	0
$n_{i\bar{\sigma}}f^\dagger_{i\sigma}f_{j\sigma}(1-n_{j\bar{\sigma}})$	1	0	1	0	1	1	0	0
$(1-n_{i\bar{\sigma}})f^\dagger_{i\sigma}f_{j\sigma}n_{j,\bar{\sigma}}$	0	0	1	1	0	1	0	1
$n_{i\bar{\sigma}}f^\dagger_{i\sigma}f_{j\sigma}n_{j\bar{\sigma}}$	1	0	1	1	1	1	0	1

Table B.1: The H_K terms act on the initial states and changes them to the final states. Each H_K term will give non-zero value for only one initial state and one final state. Acting on any other consifigurations besides those given in the table will give zero. The 0(1) in the table elements means that there is no(one) particle of a given spin at the given site, where the spin and position are labeled by the table headings.

To solve for $\mathcal{S}$, we apply projectors $P_{N/2}$ and P_η on Eq. (B.8) to arrive at

$$P_{N/2}\mathcal{S}P_\eta = [\mathrm{i}P_{N/2}H_\eta P_{N/2} + (P_{N/2}HP_{N/2})(P_{N/2}\mathcal{S}P_\eta)](P_\eta HP_\eta)^{-1}. \tag{B.10}$$

At this point, we make the assumption that the eigenenergies of the Hubbard Hamilton operator (5.1) are separated into disjointed regions in each of which the spectrum is either continuous of semi-continuous. This is certainly true in the strongly coupling limit where the energy separation between regions (labeled by the number of broken pairs) is of the order U. We can thus approximate $P_{N/2}H_\eta P_{N/2}$ by its average value over all states within the subspace of $N/2$ doubly-occupied sites. Since $P_{N/2}H_\eta P_{N/2}$ is now a number, we can solve Eq. (B.10) by iteration. The solution takes the form

$$P_{N/2}\mathcal{S}P_\eta = \mathrm{i}P_{N/2}H_\eta P_\eta(P_\eta HP_\eta - P_{N/2}HP_{N/2})^{-1}. \tag{B.11}$$

We may adopt a similar approach to approximate the value of $P_\eta HP_\eta$. Since we are really interested in the low-energy behaviour of the system, we only keep the lowest band in the subspace defined by P_η, i.e. states with only one broken pair and replace $P_\eta HP_\eta$ by its average over all states with one broken pair. We thus expect $\langle P_\eta HP_\eta\rangle - \langle P_{N/2}HP_{N/2}\rangle \approx U$, where U is the energy cost of having

a broken pair (two singly-occupied sites instead of two doubly-occupied or fully-empty sites). Substituting the expression into Eq. (B.9), the resulting effective Hamilton operator is

$$H_{\text{eff}} = \underbrace{P_{N/2}HP_{N/2} - \frac{1}{U}P_{N/2}HP_\eta HP_{N/2}}_{P_{N/2}H_{\text{eff}}P_{N/2}} + \underbrace{P_\eta HP_\eta + \frac{1}{U}P_\eta HP_{N/2}HP_\eta}_{P_\eta H_{\text{eff}}P_\eta}. \tag{B.12}$$

We are more interested in the low-energy sector with only doubly-occupied sites, hence we neglect the term $P_\eta H_{\text{eff}} P_\eta$ to obtain

$$H_{\text{eff}} = P_{N/2}HP_{N/2} - \frac{1}{U}P_{N/2}HP_\eta HP_{N/2}. \tag{B.13}$$

Notice that the kinetic energy term H_K does not conserve the number of doubly-occupied sites and $P_{N/2}H_V P_{N/2}$ is a constant, the effective Hamilton operator is further reduced to

$$H_{\text{eff}} = -\frac{1}{U}P_{N/2}HP_\eta HP_{N/2} = -\frac{1}{U}P_{N/2}H_K P_\eta H_K P_{N/2}, \tag{B.14}$$

since H_V conserves the number of doubly-occupied sites. Writing the identity operator as the sum of two terms,

$$1 = (1 - n_{i\bar{\sigma}}) + n_{i\bar{\sigma}}, \tag{B.15}$$

where $\bar{\sigma} = -\sigma$, each term in H_K is written as a sum of four terms,

$$\begin{aligned} f^\dagger_{i\sigma} f_{j\sigma} = {} & (1 - n_{i\bar{\sigma}}) f^\dagger_{i\sigma} f_{j\sigma} (1 - n_{j\bar{\sigma}}) \\ & + n_{i\bar{\sigma}} f^\dagger_{i\sigma} f_{j\sigma} (1 - n_{j\bar{\sigma}}) \\ & + (1 - n_{i\bar{\sigma}}) f^\dagger_{i\sigma} f_{j\sigma} n_{j\bar{\sigma}} \\ & + n_{i\bar{\sigma}} f^\dagger_{i\sigma} f_{j\sigma} n_{j\bar{\sigma}}. \end{aligned} \tag{B.16}$$

The meaning of the four terms is illustrated in Table B.1. Clearly, the first and the fourth terms preserve the number of doubly occupied sites, while the second and the third terms changes the number of doubly occupied sites by ± 1. Only the second term contributes to $P_{N/2} H_K P_\eta$ while only the third term contributes to $P_\eta H_K P_{N/2}$. Hence,

$$H_{\text{eff}} = -\frac{t^2}{U} P_{N/2} \left(\sum_{\substack{\boldsymbol{i},\boldsymbol{j} \\ \boldsymbol{k},\boldsymbol{l} \\ \sigma,\sigma'}} n_{\boldsymbol{i}\bar{\sigma}} f^\dagger_{\boldsymbol{i}\sigma} f_{\boldsymbol{j}\sigma} (1 - n_{\boldsymbol{j}\bar{\sigma}}) P_\eta (1 - n_{\boldsymbol{k},\bar{\sigma}'}) f^\dagger_{\boldsymbol{k},\sigma'} f_{\boldsymbol{l},\sigma'} n_{\boldsymbol{l},\bar{\sigma}'} \right) P_{N/2}. \quad \text{(B.17)}$$

The summation in fact consists of two sums, one represents the hopping of a pair from a site (the $\boldsymbol{l}$-th site) to a neighbouring site (the $\boldsymbol{k}$-th site), while the other represents a pair which is virtually broken and reformed (one particle of the pair hops to a neighbouring site and hops back to reform the pair). Writing explicitly,

$$\begin{aligned} H_{\text{eff}} &= -\frac{t^2}{U} \sum_{\boldsymbol{k},\boldsymbol{l},\sigma} \Big(n_{\boldsymbol{l}\bar{\sigma}} f^\dagger_{\boldsymbol{l}\sigma} f_{\boldsymbol{k}\sigma} (1 - n_{\boldsymbol{k}\bar{\sigma}})(1 - n_{\boldsymbol{k},\bar{\sigma}}) f^\dagger_{\boldsymbol{k},\sigma} f_{\boldsymbol{l},\sigma} n_{\boldsymbol{l},\bar{\sigma}} \\ &\quad + n_{\boldsymbol{k}\sigma} f^\dagger_{\boldsymbol{k}\bar{\sigma}} f_{\boldsymbol{l}\bar{\sigma}} (1 - n_{\boldsymbol{l}\sigma})(1 - n_{\boldsymbol{k}\bar{\sigma}}) f^\dagger_{\boldsymbol{k}\sigma} f_{\boldsymbol{l}\sigma} n_{\boldsymbol{l}\bar{\sigma}} \Big) \\ &= -\frac{t^2}{U} \sum_{\boldsymbol{k},\boldsymbol{l},\sigma} \Big((1 - n_{\boldsymbol{k}\bar{\sigma}})(1 - n_{\boldsymbol{k}\sigma}) n_{\boldsymbol{l}\sigma} n_{\boldsymbol{l}\bar{\sigma}} + f^\dagger_{\boldsymbol{k}\sigma} f^\dagger_{\boldsymbol{k}\bar{\sigma}} f_{\boldsymbol{l}\bar{\sigma}} f_{\boldsymbol{l}\sigma} \Big) \\ &= -\frac{2t^2}{U} \sum_{\boldsymbol{k},\boldsymbol{l}} \Big((1 - n_{\boldsymbol{k}\uparrow})(1 - n_{\boldsymbol{k}\downarrow}) n_{\boldsymbol{l}\uparrow} n_{\boldsymbol{l}\downarrow} + f^\dagger_{\boldsymbol{k}\uparrow} f^\dagger_{\boldsymbol{k}\downarrow} f_{\boldsymbol{l}\downarrow} f_{\boldsymbol{l}\uparrow} \Big). \end{aligned} \quad \text{(B.18)}$$

We have previously defined the z-component of the pseudo-spin (6.23) as

$$\Rightarrow J^z_{\boldsymbol{k}} = \frac{1}{2}(n_{\boldsymbol{k}\uparrow} + n_{\boldsymbol{k}\downarrow} - 1) = \begin{cases} \frac{1}{2}, & \text{a pair at } \boldsymbol{k}\text{th site} \\ -\frac{1}{2}, & \text{no pair at } \boldsymbol{k}\text{th site} \\ 0, & \text{single particle at } \boldsymbol{k}\text{th site} \end{cases} \quad \text{(B.19)}$$

Since we are only interested in the subspace where there is either a pair or no pair

of particles at the $\boldsymbol{k}$th site, we can rewrite $J^z_{\boldsymbol{k}}$ as

$$J^z_{\boldsymbol{k}} = n_{\boldsymbol{k}\uparrow} n_{\boldsymbol{k}\downarrow} - \frac{1}{2}. \tag{B.20}$$

Next, we combine the terms in Eq. (B.18) that involve virtual hopping from the $\boldsymbol{k}$th site to the $\boldsymbol{l}$th site and from the $\boldsymbol{l}$th site to the $\boldsymbol{k}$th site to arrive at

$$\begin{aligned}
H_{\text{eff}} &= -\frac{2t^2}{U} \sum_{\langle \boldsymbol{k},\boldsymbol{l} \rangle} \Big((1 - n_{\boldsymbol{k}\uparrow})(1 - n_{\boldsymbol{k}\downarrow}) n_{\boldsymbol{l}\uparrow} n_{\boldsymbol{l}\downarrow} + \Delta^\dagger_{\boldsymbol{k}} \Delta_{\boldsymbol{l}} \\
&\quad + (1 - n_{\boldsymbol{l}\uparrow})(1 - n_{\boldsymbol{l}\downarrow}) n_{\boldsymbol{k}\uparrow} n_{\boldsymbol{k}\downarrow} + \Delta^\dagger_{\boldsymbol{l}} \Delta_{\boldsymbol{k}} \Big) \\
&= -\frac{2t^2}{U} \sum_{\langle \boldsymbol{k},\boldsymbol{l} \rangle} \left((\frac{1}{2} - J^z_{\boldsymbol{k}})(\frac{1}{2} + J^z_{\boldsymbol{l}}) + (\frac{1}{2} + J^z_{\boldsymbol{k}})(\frac{1}{2} - J^z_{\boldsymbol{l}}) - J^+_{\boldsymbol{k}} J^-_{\boldsymbol{l}} - J^-_{\boldsymbol{k}} J^+_{\boldsymbol{l}} \right) \\
&= -\frac{2t^2}{U} \sum_{\langle \boldsymbol{k},\boldsymbol{l} \rangle} \left(\frac{1}{2} - 2 J^z_{\boldsymbol{k}} J^z_{\boldsymbol{l}} - 2 J^x_{\boldsymbol{k}} J^x_{\boldsymbol{l}} - 2 J^y_{\boldsymbol{k}} J^y_{\boldsymbol{l}} \right) \\
&= \frac{4t^2}{U} \sum_{\langle \boldsymbol{k},\boldsymbol{l} \rangle} \boldsymbol{J}_{\boldsymbol{k}} \cdot \boldsymbol{J}_{\boldsymbol{l}},
\end{aligned} \tag{B.21}$$

where $\langle \boldsymbol{k}, \boldsymbol{l} \rangle$ sums over all nearest neighbour sites. The term $\frac{1}{2}$ has been removed from the last line as it does not affect the effective Hamiltonian and the resulting effective Hamiltonian describes a Heisenberg pseudo-spin system in the given bipartite lattice. Clearly, the ground state of the system displays antiferromagnetic ordering of the pseudo-spins.

Bibliography

[1] K. S. Novoselov, A. K. Geim, S. V. Morozov, D. Jiang, Y. Zhang, S. V. Dubonos, I. V. Grigorieva, and A. A. Firsov, *Electric field effect in atomically thin carbon films*, Science **306** (2004), 666.

[2] Y.-M. Lin, C. Dimitrakopoulos, K. A. Jenkins, D. B. Farmer, H.-Y. Chiu, A. Grill, and P. Avouris, *100-GHz transistors from wafer-scale epitaxial graphene*, Science **327** (2010), 662.

[3] G. W. Semenoff, *Condensed-matter simulation of a three-dimensional anomaly*, Phys. Rev. Lett. **53** (1984), 2449–2452.

[4] K. S. Novoselov, A. K. Geim, S. V. Morozov, D. Jiang, M. I. Katsnelson, I. V. Grigorieva, S. V. Dubonos, , and A. A. Firsov, *Two-dimensional gas of massless Dirac fermions in graphene*, Nature **438** (2005), 197–200.

[5] M. Wilson, *Electrons in atomically thin carbon sheets behave like massless particles*, Phys. Today **59** (2006), 21.

[6] A. C. Neto, F. Guinea, and N. M. Peres, *Drawing conclusions from graphene*, Phys. World **19** (2006), 33.

[7] S. Y. Zhou, G.-H. Gweon, J. Graf, A. V. Fedorov, C. D. Spataru, R. D. Diehl, Y. Kopelevich, D.-H. Lee, S. G. Louie, and A. Lanzara, *First direct observation of Dirac fermions in graphite*, Nat. Phys. **2** (2006), 595.

[8] M. I. Katsnelson, K. S. Novoselov, and A. K. Geim, *Chiral tunnelling and the Klein paradox in graphene*, Nat. Phys. **2** (2006), 620.

[9] M. I. Katsnelson and K. S. Novoselov, *Graphene: New bridge between condensed matter physics and quantum electrodynamics*, Solid State Comm. **143** (2007), 3.

[10] A. H. Castro Neto, F. Guinea, N. M. R. Peres, K. S. Novoselov, and A. K. Geim, *The electronic properties of graphene*, Rev. Mod. Phys. **81** (2009), 109–162.

[11] Y. Zhang, Y. Tan, H. Stormer, and P. Kim, *Experimental observation of the quantum hall effect and Berry's phase in graphene*, Nature **438** (2005), 201.

[12] G. Li and E. Andrei, *Observation of Landau levels of Dirac fermions in graphene*, Nat. Phys. **3** (2007), 623.

[13] J. C. Meyer, A. K. Geim, M. I. Katsnelson, K. S. Novoselov, T. J. Booth, and S. Roth, *The structure of suspended graphene sheets*, Nature **446** (2007), 60–63.

[14] A. Fasolino, J. H. Los, and M. I. Katsnelson, *Intrinsic ripples in graphene*, Nat. Mat. **6** (2007), 858–861.

[15] V. P. Gusynin, S. G. Sharapov, and J. P. Carbotte, *On the universal ac optical background in graphene*, New J. Phys. **11** (2009), 095013.

[16] Y. Zhang, V. W. Brar, C. Girit, A. Zettl, and M. F. Crommie, *Origin of spatial charge inhomogeneity in graphene*, Nat. Phys. **5** (2009), 722–726.

[17] M. H. Anderson, J. R. Ensher, M. R. Matthews, C. E. Wieman, and E. A. Cornell, *Observation of Bose-Einstein Condensation in a dilute atomic vapor*, Science **269** (1995), 198–201.

[18] C. C. Bradley, C. A. Sackett, J. J. Tollett, and R. G. Hulet, *Evidence of Bose-Einstein condensation in an atomic gas with attractive interactions*, Phys. Rev. Lett. **75** (1995), 1687–1690.

[19] K. B. Davis, M. O. Mewes, M. R. Andrews, N. J. van Druten, D. S. Durfee, D. M. Kurn, and W. Ketterle, *Bose-Einstein condensation in a gas of Sodium atoms*, Phys. Rev. Lett. **75** (1995), 3969–3973.

[20] B. DeMarco, J. L. Bohn, J. P. Burke, M. Holland, and D. S. Jin, *Measurement of p-wave threshold law using evaporatively cooled fermionic atoms*, Phys. Rev. Lett. **82** (1999), 4208–4211.

[21] F. Schreck, L. Khaykovich, K. L. Corwin, G. Ferrari, T. Bourdel, J. Cubizolles, and C. Salomon, *Quasipure Bose-Einstein condensate immersed in a Fermi sea*, Phys. Rev. Lett. **87** (2001), 080403.

[22] A. G. Truscott, K. E. Strecker, W. I. McAlexander, G. B. Partridge, and R. G. Huletdagger, *Observation of Fermi pressure in a gas of trapped atoms*, Science **291** (2001), 2570–2572.

[23] J. Cubizolles, T. Bourdel, S. J. J. M. F. Kokkelmans, G. V. Shlyapnikov, and C. Salomon, *Production of long-lived ultracold Li2 molecules from a fermi gas*, Phys. Rev. Lett. **91** (2003), 240401.

[24] M. W. Zwierlein, J. R. Abo-Shaeer, A. Schirotzek, C. H. Schunck, and W. Ketterle, *Vortices and superfluidity in a strongly interacting Fermi gas*, Nature **435** (2005), 1047–1051.

[25] M. W. Zwierlein, A. Schirotzek, C. H. Schunck, and W. Ketterle, *Fermionic Superfluidity with Imbalanced Spin Populations*, Science **311** (2006), 492–496.

[26] G. B. Partridge, W. Li, R. I. Kamar, Y.-a. Liao, and R. G. Hulet, *Pairing and Phase Separation in a Polarized Fermi Gas*, Science **311** (2006), 503–505.

[27] Y. Shin, M. W. Zwierlein, C. H. Schunck, A. Schirotzek, and W. Ketterle, *Observation of phase separation in a strongly interacting imbalanced Fermi gas*, Phys. Rev. Lett. **97** (2006), 030401.

[28] G. B. Partridge, W. Li, Y. A. Liao, R. G. Hulet, M. Haque, and H. T. C. Stoof, *Deformation of a trapped fermi gas with unequal spin populations*, Phys. Rev. Lett. **97** (2006), 190407.

[29] Y. il Shin, C. H. Schunck, A. Schirotzek1, and W. Ketterle, *Phase diagram of a two-component Fermi gas with resonant interactions*, Nature **451** (2007), 689–693.

[30] J. K. Chin, D. E. Miller, Y. Liu, C. Stan, W. Setiawan, C. Sanner, K. Xu, and W. Ketterle, *Evidence for superfluidity of ultracold fermions in an optical lattice*, Nature **443** (2006), 961–964.

[31] W. Ketterle and M. W. Zwierlein, *Making, probing and understanding ultracold Fermi gases*, Riv Nuovo Cimento **31** (2008), 247–422.

[32] E. Timmermans, P. Tommasini, M. Hussein, and A. Kerman, *Feshbach resonances in atomic Bose-Einstein condensates*, Phys. Rep. **315** (1999), 199.

[33] S.-L. Zhu, B. Wang, and L.-M. Duan, *Simulation and detection of Dirac fermions with cold atoms in an optical lattice*, Phys. Rev. Lett. **98** (2007), 260402.

[34] A. Damascelli, Z. Hussain, and Z.-X. Shen, *Angle-resolved photoemission studies of the cuprate superconductors*, Rev. Mod. Phys. **75** (2003), 473–541.

[35] P. A. Lee, N. Nagaosa, and X.-G. Wen, *Doping a Mott insulator: Physics of high-temperature superconductivity*, Rev. Mod. Phys. **78** (2006), 17–85.

[36] A. Leggett, *Quantum Liquids*: *Bose Condensation and Cooper Pairing in Condensed-Matter Systems*, Oxford University Press, Oxford, 2006.

[37] J. E. Hirsch, *Two-dimensional Hubbard model: Numerical simulation study*, Phys. Rev. B **31** (1985), 4403–4419.

[38] T. Paiva, R. T. Scalettar, W. Zheng, R. R. P. Singh, and J. Oitmaa, *Ground-state and finite-temperature signatures of quantum phase transitions in the half-filled Hubbard model on a honeycomb lattice*, Phys. Rev. B **72** (2005), 085123.

[39] D. Baeriswyl, D. K. Campbell, and S. Mazumdar, *Correlations and defect energies*, Phys. Rev. Lett. **56** (1986), 1509.

[40] J. González, F. Guinea, and M. A. H. Vozmediano, *Marginal-Fermi-liquid behavior from two-dimensional Coulomb interaction*, Phys. Rev. B **59** (1999), R2474–R2477.

[41] M. Mueller, L. Fritz, S. Sachdev, and J. Schmalian, *Graphene: Relativistic transport in a nearly perfect quantum liquid*, ArXiv e-prints (2009). Proceedings for ICMP 09.

[42] K. L. Lee, K. Bouadim, G. G. Batrouni, F. Hébert, R. T. Scalettar, C. Miniatura, and B. Grémaud, *Attractive Hubbard model on a honeycomb lattice: Quantum Monte Carlo study*, Phys. Rev. B **80** (2009), 245118.

[43] Z. Y. Meng, T. C. Lang, S. Wessel, F. F. Assaad, and A. Muramatsu, *Quantum spin liquid emerging in two-dimensional correlated Dirac fermions*, Nature **464** (2010), 847–851.

[44] S.-S. Lee and P. A. Lee, *U(1) gauge theory of the Hubbard model: Spin liquid states and possible application to κ-(BEDT-TTF)$_2$Cu$_2$(CN)$_3$*, Phys. Rev. Lett. **95** (2005), 036403.

[45] M. Hermele, *SU(2) gauge theory of the Hubbard model and application to the honeycomb lattice*, Phys. Rev. B **76** (2007), 035125.

[46] E. Zhao and A. Paramekanti, *Self-consistent slave rotor mean-field theory for strongly correlated systems*, Phys. Rev. B **76** (2007), 195101.

[47] N. W. Ashcroft and N. D. Mermin, *Solid State Physics*, Thomson Learning, Inc., USA, 1976.

[48] M. Tinkham, *Group Theory and Quantum Mechanics*, Dover Publications, Inc., Mineola, New York, 1992.

[49] W. M. Lomer, *The valence bands in two-dimensional graphite*, Proc. R. Soc. Lon. Ser-A **227** (1955), 330.

[50] P. R. Wallace, *The band theory of graphite*, Phys. Rev. **71** (1947), 622–634.

[51] J. C. Slonczewski and P. R. Weiss, *Band structure of graphite*, Phys. Rev. **109** (1958), 272–279.

[52] K. L. Lee, B. Grémaud, R. Han, B.-G. Englert, and C. Miniatura, *Ultracold fermions in a graphene-type optical lattice*, Phys. Rev. A **80** (2009), 043411.

[53] R. Han, *Massless Dirac fermions in honeycomb potential*, 2007. Unpublished.

[54] G. H. Wannier, *The structure of electronic excitation levels in insulating crystals*, Phys. Rev. **52** (1937), 191–197.

[55] W. Kohn, *Analytic properties of Bloch waves and Wannier functions*, Phys. Rev. **115** (1959), 809–821.

[56] S. Kivelson, *Wannier functions in one-dimensional disordered systems: Application to fractionally charged solitons*, Phys. Rev. B **26** (1982), 4269–4277.

[57] J. D. Cloizeaux, *Orthogonal orbitals and generalized Wannier functions*, Phys. Rev. **129** (1963), 554–566.

[58] J. D. Cloizeaux, *Analytical properties of n-dimensional energy bands and Wannier functions*, Phys. Rev. **135** (1964), A698–A707.

[59] J. D. Cloizeaux, *Energy bands and projection operators in a crystal: Analytic and asymptotic properties*, Phys. Rev. **135** (1964), A685–A697.

[60] I. Affleck, J. Harveya, and E. Witten, *Instantons and (super-) symmetry breaking in (2+1) dimensions*, Nucl. Phys. B **206** (1982), 413–439.

[61] J. P. Hobson and W. A. Nierenberg, *The statistics of a two-dimensional, hexagonal net*, Phys. Rev. **89** (1953), 662.

[62] H. B. Rosenstock, *Dynamics of the graphite lattice*, J. Chem. Phys. **21** (1953), 2064–2069.

[63] J. Dalibard and C. Cohen-Tannoudji, *Dressed-atom approach to atomic motion in laser light: the dipole force revisited*, J. Opt. Soc. Am. B **2** (1985), 1707–1720.

[64] C. Cohen-Tannoudji, J. Dupont-Roc, and G. Grynberg, *Atom-Photon Interactions: Basic Processes and Applications*, Wiley-Interscience, 1998.

[65] C. Foot, *Atomic Physics*, Oxford University Press, 2005.

[66] H. Wallis, *Quantum theory of atomic motion in laser light*, Phys. Rep. **255** (1995), 203.

[67] R. Grimm, M. Weidemüller, and Y. B. Ovchinnikov, *Optical dipole traps for neutral atoms*, Adv. At. Mol. Opt. Phys. **42** (2000), 95.

[68] G. Grynberg and C. Robilliard, *Cold atoms in dissipative optical lattices*, Phys. Rep. **355** (December 2001), 335–451(117).

[69] M. Greiner, O. Mandel, T. Esslinger, T. W. Hänsch, and I. Bloch, *Quantum phase transition from a superfluid to a Mott insulator in a gas of ultracold atoms*, Nature **415** (2002), 39.

[70] D. Jaksch, C. Bruder, J. I. Cirac, C. W. Gardiner, and P. Zoller, *Cold bosonic atoms in optical lattices*, Phys. Rev. Lett. **81** (1998), 3108–3111.

[71] M. Lewenstein, A. Sanpera, V. Ahufinger, B. Damski, A. Sen(de), and U. Sen, *Ultracold atomic gases in optical lattices: mimicking condensed matter physics and beyond*, Adv. Phys. **56** (2007), 243–379.

[72] D. Jaksch, H.-J. Briegel, J. I. Cirac, C. W. Gardiner, and P. Zoller, *Entanglement of atoms via cold controlled collisions*, Phys. Rev. Lett. **82** (1999), 1975–1978.

[73] I. Bloch, *Ultracold quantum gases in optical lattices*, Nat. Phys. **1** (2005), 23–30.

[74] X. Chen, B. Zeng, Z.-C. Gu, B. Yoshida, and I. L. Chuang, *Gapped two-body Hamiltonian whose unique ground state is universal for one-way quantum computation*, Phys. Rev. Lett. **102** (2009), 220501.

[75] E. R. Dufresne and D. G. Grier, *Optical tweezer arrays and optical substrates created with diffractive optics*, Rev. Sci. Instrum. **69** (1998), 1974–1977.

[76] J. E. Curtis, B. A. Koss, and D. G. Grier, *Dynamic holographic optical tweezers*, Opt. Commun. **207** (2002), 169–175.

[77] D. G. Grier, *A revolution in optical manipulation*, Nature **424** (2003), 810–816.

[78] D. G. Grier and Y. Roichman, *Holographic optical trapping*, Appl. Opt. **45** (2006), 880–887.

[79] J. Liesener, M. Reicherter, T. Haist, and H. J. Tiziani, *Multi-functional optical tweezers using computer-generated holograms*, Opt. Commun. **185** (2000), 77–82.

[80] D. Palima, C. A. Alonzo, P. J. Rodrigo, and J. Glückstad, *Generalized phase contrast matched to gaussian illumination*, Opt. Express **15** (2007), 11971–11977.

[81] I. Bloch, J. Dalibard, and W. Zwerger, *Many-body physics with ultracold gases*, Rev. Mod. Phys. **80** (2008), 885–964.

[82] M. Gutzwiller, *Chaos in Classical and Quantum Mechanics*, Springer, New York, 1990.

[83] G. V. Mil'nikov and H. Nakamura, *Practical implementation of the instanton theory for the ground-state tunneling splitting*, J. Chem. Phys. **115** (2001), 6881–6897.

[84] L. Schulman, *Techniques and Applications of Path Integration*, Wiley, New York, 1981.

[85] W. Zwerger, *Mott–Hubbard transition of cold atoms in optical lattices*, J. Opt. B: Quantum Semiclass. Opt. **5** (2003), S9.

[86] M. E. Gehm, *Properties of* ^{6}*Li*, Jetlab, 1st edn., 2003.

[87] Y. Hasegawa, R. Konno, H. Nakano, and M. Kohmoto, *Zero modes of tight-binding electrons on the honeycomb lattice*, Phys. Rev. B **74** (2006), 033413.

[88] G. Montambaux, F. Piéchon, J.-N. Fuchs, and M. O. Goerbig, *Merging of Dirac points in a two-dimensional crystal*, Phys. Rev. B **80** (2009), 153412.

[89] C.-H. Park, L. Yang, Y.-W. Son, M. L. Cohen, and S. G. Louie, *Anisotropic behaviours of massless Dirac fermions in graphene under periodic potentials*, Nat. Phys. **4** (2008), 213–217.

[90] C. Bai and X. Zhang, *Klein paradox and resonant tunneling in a graphene superlattice*, Phys. Rev. B **76** (2007), 075430.

[91] P. Lecheminant, *One-dimensional spin liquids*, in *Frustrated Spin Systems*, H. Diep, ed., World Scientific Publishing Company, Singapore (2005) pp. 307–366.

[92] J. K. Block and N. Nygaard, *Honeycomb optical lattices with harmonic confinement*, Phys. Rev. A **81** (2010), 053421.

[93] G.-W. Li, S.-J. Huang, H.-S. Wu, S. Fang, D.-S. Hong, T. Mohamed, and D.-J. Han, *A Michelson interferometer for relative phase locking of optical beams*, J. Phys. Soc. Jpn. **77** (2008), 024301.

[94] E. Tiesinga, B. J. Verhaar, and H. T. C. Stoof, *Threshold and resonance phenomena in ultracold ground-state collisions*, Phys. Rev. A **47** (1993), 4114–4122.

[95] H. Feshbach, *Unified theory of nuclear reactions*, Ann. Phys. **5** (1958), 357 – 390.

[96] M. Theis, G. Thalhammer, K. Winkler, M. Hellwig, G. Ruff, R. Grimm, and J. H. Denschlag, *Tuning the scattering length with an optically induced Feshbach resonance*, Phys. Rev. Lett. **93** (2004), 123001.

[97] C. H. Schunck, M. W. Zwierlein, C. A. Stan, S. M. F. Raupach, W. Ketterle, A. Simoni, E. Tiesinga, C. J. Williams, and P. S. Julienne, *Feshbach resonances in fermionic ^6Li*, Phys. Rev. A **71** (2005), 045601.

[98] E. R. I. Abraham, W. I. McAlexander, J. M. Gerton, R. G. Hulet, R. Côté, and A. Dalgarno, *Triplet s-wave resonance in ^6Li collisions and scattering lengths of ^6Li and ^7Li*, Phys. Rev. A **55** (1997), R3299–R3302.

[99] J. Hubbard, *Electron Correlations in Narrow Energy Bands*, Proc. R. Soc. London, Ser. A **276** (1963), 238.

[100] J. Hubbard, *Electron correlations in narrow energy bands. v. a perturbation expansion about the atomic limit*, Proc. R. Soc. London, Ser. A **296** (1967), 82.

[101] T. Bourdel, L. Khaykovich, J. Cubizolles, J. Zhang, F. Chevy, M. Teichmann, L. Tarruell, S. J. J. M. F. Kokkelmans, and C. Salomon, *Experimental study of the BEC-BCS crossover region in Lithium 6*, Phys. Rev. Lett. **93** (2004), 050401.

[102] S. Jochim, M. Bartenstein, A. Altmeyer, G. Hendl, C. Chin, J. H. Denschlag, and R. Grimm, *Pure gas of optically trapped molecules created from Fermionic atoms*, Phys. Rev. Lett. **91** (2003), 240402.

[103] G. M. Falco and H. T. C. Stoof, *Atom-molecule theory of broad Feshbach resonances*, Phys. Rev. A **71** (2005), 063614.

[104] J. E. Hirsch, *Discrete Hubbard-Stratonovich transformation for fermion lattice models*, Phys. Rev. B **28** (1983), 4059–4061.

[105] R. Blankenbecler, D. J. Scalapino, and R. L. Sugar, *Monte Carlo calculations of coupled boson-fermion systems. I*, Phys. Rev. D **24** (1981), 2278–2286.

[106] E. Y. Loh, J. E. Gubernatis, R. T. Scalettar, S. R. White, D. J. Scalapino, and R. L. Sugar, *Sign problem in the numerical simulation of many-electron systems*, Phys. Rev. B **41** (1990), 9301–9307.

[107] Z. Bai, W. Chen, R. Scalettar, and I. Yamazaki, *Lecture Notes on Advances of Numerical Methods for Hubbard Quantum Monte Carlo simulation, Part 1*, 2007. Available at `http://www.cs.ucdavis.edu/~bai/lanzhou07/Day2B.pdf`.

[108] J. E. Hirsch, *Stable Monte Carlo algorithm for fermion lattice systems at low temperatures*, Phys. Rev. B **38** (1988), 12023–12026.

[109] R. R. dos Santos, *Introduction to quantum Monte Carlo simulations for fermionic systems*, Braz. J. Phys. **33** (2003), 36.

[110] A. L. Fetter and J. D. Walecka, *Quantum Theory of Many-Particle Systems*, Dover Publications, 2003.

[111] J. W. Negele and H. Orland, *Quantum Many-Particle Systems*, Westview Press, Boulder, Colorado, 1998.

[112] M. Jarrell and J. E. Gubernatis, *Bayesian inference and the analytic continuation of imaginary-time quantum Monte Carlo data*, Phys. Rep. **269** (1996), 133 – 195.

[113] R. N. Silver, D. S. Sivia, and J. E. Gubernatis, *Maximum-entropy method for analytic continuation of quantum Monte Carlo data*, Phys. Rev. B **41** (1990), 2380–2389.

[114] S. Gull, *Developments in maximum entropy data analysis*, in *Maximum Entropy and Bayesian Methods*, J. Skilling, ed., Kluwer Academic, Dordrecht (1989) pp. 53–71.

[115] A. J. Leggett, in *Modern Trends in the Theory of Condensed Matter: Proceedings of the XVIth Karpacz Winter School of Theoretical Physics, Karpacz, Poland*, A. Pekalski and J. Przystawa, eds., Springer-Verlag, Berlin; New York (1980) p. 13.

[116] P. Nozières and S. Schmitt-Rink, *Bose condensation in an attractive fermion gas*, J. Low. Temp. Phys. **59** (1985), 195.

[117] M. Randeria, *Crossover from BCS theory to Bose-Einstein condensation*, in *Bose-Einstein Condensation*, A. Griffin, D. Snoke, and S. Stringari, eds., Cambridge University Press, Cambridge, U.K. (1994) p. 355.

[118] N. D. Mermin and H. Wagner, *Absence of ferromagnetism or antiferromagnetism in one- or two-dimensional isotropic Heisenberg models*, Phys. Rev. Lett. **17** (1966), 1133–1136.

[119] A. Gelfert and W. Nolting, *The absence of finite-temperature phase transitions in low-dimensional many-body models: a survey and new results*, J. Phys-Condens. Mat. **13** (2001), R505.

[120] M. B. Walker and T. W. Ruijgrok, *Absence of magnetic ordering in one and two dimensions in a many-band model for interacting electrons in a metal*, Phys. Rev. **171** (1968), 513–515.

[121] D. K. Ghosh, *Nonexistence of magnetic ordering in the one- and two-dimensional Hubbard model*, Phys. Rev. Lett. **27** (1971), 1584–1587.

[122] J. M. Kosterlitz and D. J. Thouless, *Ordering , metastability and phase transition in two-dimensional system*, J. Phys. C: Solid State Phys. **6** (1973), 1181.

[123] V. L. Berezinskii, *Destruction of long-range order in one-dimensional and two-dimensional systems having a continuous symmetry group I. classical systems*, Sov. Phys. JETP **32** (1971), 493.

[124] V. L. Berezinskii, *Destruction of long-range order in one-dimensional and two-dimensional systems having a continuous symmetry group II. quantum systems*, Sov. Phys. JETP **34** (1972), 610.

[125] E. Zhao and A. Paramekanti, *BCS-BEC crossover on the two-dimensional honeycomb lattice*, Phys. Rev. Lett. **97** (2006), 230404.

[126] S.-Q. Su, K.-M. Tam, and H.-Q. Lin, *Evolution of superconductor pairing interactions from weak to strong coupling on a honeycomb lattice*, Phys. Rev. B **80** (2009), 104517.

[127] H. T. Stoof, K. B. Gubbels, and D. B. Dickerscheid, *Ultracold Quantum Fields*, Springer, Dordrecht, The Netherlands, 2009.

[128] C. A. R. Sá de Melo, M. Randeria, and J. R. Engelbrecht, *Crossover from BCS to Bose superconductivity: Transition temperature and time-dependent Ginzburg-Landau theory*, Phys. Rev. Lett. **71** (1993), 3202–3205.

[129] J. R. Engelbrecht, M. Randeria, and C. A. R. Sáde Melo, *BCS to Bose crossover: Broken-symmetry state*, Phys. Rev. B **55** (1997), 15153–15156.

[130] S. Zhang, *Pseudospin symmetry and new collective modes of the Hubbard model*, Phys. Rev. Lett. **65** (1990), 120–122.

[131] A. Auerbach, *Interacting Electrons and Quantum Magnetism*, Springer-Verlag, 1994.

[132] J. P. Wallington and J. F. Annett, *Discrete symmetries and transformations of the Hubbard model*, Phys. Rev. B **58** (1998), 1218–1221.

[133] S. Robaszkiewicz, R. Micnas, and K. A. Chao, *Thermodynamic properties of the extended Hubbard model with strong intra-atomic attraction and an arbitrary electron density*, Phys. Rev. B **23** (1981), 1447–1458.

[134] S. Robaszkiewicz, R. Micnas, and K. A. Chao, *Chemical potential and order parameter of extended Hubbard model with strong intra-atomic attraction*, Phys. Rev. B **24** (1981), 1579–1582.

[135] S. Robaszkiewicz, R. Micnas, and K. A. Chao, *Hartree theory for the negative-u extended Hubbard model: Ground state*, Phys. Rev. B **24** (1981), 4018–4024.

[136] A. Moreo and D. J. Scalapino, *Two-dimensional negative-U Hubbard model*, Phys. Rev. Lett. **66** (1991), 946–948.

[137] K. A. Chao, J. Spałek, and A. M. Oleś, *Canonical perturbation expansion of the Hubbard model*, Phys. Rev. B **18** (1978), 3453–3464.

[138] J. Spalek, *t-J model then and now: a personal perspective from the pioneering times*, Acta Phys. Pol. A **111** (2007), 409–424.

[139] P. W. Anderson, *The Resonating Valence Bond State in La2CuO4 and Superconductivity*, Science **235** (1987), 1196–1198.

[140] D. A. Huse, *Ground-state staggered magnetization of two-dimensional quantum Heisenberg antiferromagnets*, Phys. Rev. B **37** (1988), 2380–2382.

[141] T. Paiva, R. R. dos Santos, R. T. Scalettar, and P. J. H. Denteneer, *Critical temperature for the two-dimensional attractive Hubbard model*, Phys. Rev. B **69** (2004), 184501.

[142] J. González, F. Guinea, and M. A. H. Vozmediano, *Non-Fermi liquid behavior of electrons in the half-filled honeycomb lattice (a renormalization group approach)*, Nucl. Phys. B **424** (1994), 595–618.

[143] S. Das Sarma, E. H. Hwang, and W.-K. Tse, *Many-body interaction effects in doped and undoped graphene: Fermi liquid versus non-Fermi liquid*, Phys. Rev. B **75** (2007), 121406.

[144] M. Polini, R. Asgari, Y. Barlas, T. Pereg-Barnea, and A. MacDonald, *Graphene: A pseudochiral Fermi liquid*, Solid State Commun. **143** (2007), 58–62.

[145] M. I. Katsnelson, *Optical properties of graphene: The Fermi-liquid approach*, Europhys. Lett. **84** (2008), 37001.

[146] K. Ziegler, *Minimal conductivity of graphene: Nonuniversal values from the Kubo formula*, Phys. Rev. B **75** (2007), 233407.

[147] Y.-W. Tan, Y. Zhang, K. Bolotin, Y. Zhao, S. Adam, E. H. Hwang, S. Das Sarma, H. L. Stormer, and P. Kim, *Measurement of scattering rate and minimum conductivity in graphene*, Phys. Rev. Lett. **99** (2007), 246803.

[148] T. Ando, Y. Zheng, and H. Suzuura, *Dynamical conductivity and zero-mode anomaly in honeycomb lattices*, J. Phys. Soc. Jpn **71** (2002), 1318–1324.

[149] L. Hao and L. Sheng, *Optical conductivity of multilayer graphene*, Solid State Commun. **149** (2009), 1962 – 1966.

[150] I. B. Spielman, *Raman processes and effective gauge potentials*, Phys. Rev. A **79** (2009), 063613.

[151] Y.-J. Lin, R. L. Compton, K. Jiménez-García, J. V. Porto, and I. B. Spielman, *Synthetic magnetic fields for ultracold neutral atoms*, Nature **462** (2009), 628–632.

[152] B. Pierce, *A Short Table of Integrals*, Ginn and Company, 4th edn., 1956.